Two Degree of Freedom Control for Disk Drive Servo Systems

by

Li Yi

B.E. (Chengdu University of Science and Technology, China) 1993

A dissertation submitted in partial satisfaction of the
requirements for the degree of
Doctor of Philosophy

in

Mechanical Engineering

in the

GRADUATE DIVISION
of the
UNIVERSITY of CALIFORNIA at BERKELEY

Committee in charge:

Professor Masayoshi Tomizuka, Chair
Professor Roberto Horowitz
Professor Ronald Fearing

Fall 2000

The dissertation of Li Yi is approved:

_____

Chair   Date

_____

Date

_____

Date

University of California at Berkeley

Fall 2000

Two Degree of Freedom Control for Disk Drive Servo Systems

Abstract

Two Degree of Freedom Control for Disk Drive Servo Systems

by

Li Yi

Doctor of Philosophy in Mechanical Engineering

University of California at Berkeley

Professor Masayoshi Tomizuka, Chair

This dissertation investigates two degree of freedom (2DOF) control and its application to the hard disk drive (HDD) servo system. In the HDD application, the 2DOF controller operates for both track seeking and track following modes, therefore eliminating the mode changes that may exacerbate the settling of the read/write (R/W) head.

Practical considerations for the HDD servo system are addressed in its design and optimization. A simple method is also developed to model the track mis-registration (TMR) sources from the position error signals (PES).

The 2DOF controller contains three major components. The first component is a feedforward controller, for which zero phase error tracking (ZPET) control or model following control can be used. A proposed feedforward control using embedded position in servo sectors shows 30% PES improvement by simulations. The second component is a reference generator providing aggressive but safe position profiles for track seeking. The

third component of the controller is a robust feedback controller, for which a disturbance observer (DOB) or an adaptive robust controller (ARC) can be used. Simulations and experiments on its use for track seeking control show that both seek time and tracking errors can be reduced.

HDD track density is determined by the TMR performance of the track following controller. Various tradeoffs have to be made for the required performance. This dissertation addresses the optimization of the servo controller with a fixed structure. The optimization problem is formulated to minimize the PES variance with constraints. The cost functions use weighting sequences from the TMR source models. The noise environment of the servo system is then accurately represented. Using the proposed method, a 2DOF controller with DOB and a conventional PID controller are optimized. Simulations show that the 2DOF controller achieves better stability margins, as well as better TMR performance.

_____

Professor Masayoshi Tomizuka
Dissertation Committee Chair

To My Parents

Shunian Yi and Zhiping Feng

Contents

List of Figures

List of Tables

Acknowledgements

First and foremost, I would like to thank my research advisor, Professor Masayoshi Tomizuka, for his consistent support and guidance. His exceptional professional standards have been an inspiration to me. His genuine respect for all of his students has been deeply appreciated by us. He always gave me full freedom to pursue my own path, but was also always available for guidance when I needed it.

I also wish to thank Professor Roberto Horowitz and Professor Ronald Fearing for serving on my thesis committee and giving me valuable feedback.

Ever since I joined Professor Tomizuka's Mechanical System Control lab, I have learned a great deal from my fellow students. I would like to thank Dr. Lin Guo, Professor Bin Yao, Dr. Weiguang Niu, Dr. Victor Chu, Dr. Matt White, Dr. Carlos Osorio, Dr. Chieh Chen and Dr. Rob Bickel for their warm friendship during my early years at Berkeley.

I would also like to thank the current members of Professor Tomizuka's research group for their support and the wonderful moments we shared together. Special thanks go to Shashikanth Suryanarayanan, Erwin Satrya Budiman, Soichi Ibaraki, and Jengyu Wang for maintaining the lab facilities and web site.

From 1996 to 1998, I had the fortune to work with Dr. Jun Ishikawa from NEC, Takeyori Hara from Fujitsu, and Dr. Susumu Hara from Keio University. The experiments in this dissertation would not have been possible without their friendly help and support.

For my research on disk drive servo systems, I would like to thank Dr. Jun Ishikawa, Takeyori Hara, Dr. Susumu Hara, Professor Craig Smith, Jiagen Ding, Bo Zhu, and Masanao Fukunaga for their valuable help and insights.

I would also like to thank Dr. Lin Guo, Dr. Ho Lee, Mr. Yu Sun, Ms. Xiaoping Hu at Maxtor Corporation, as well as Mr. Edgar Sheh and Mr. Duc Phan at Western Digital Corporation (WDC), for their warm friendship and help during my employment with them. The work experience with them greatly enhanced my practical understanding of the servo systems in the disk drive industry.

Special thanks go to Mr. Duc Phan, a director at WDC with more than 20 years' experience in the disk drive industry. He proofread the dissertation line by line, provided valuable technical feedbacks and suggestions. He also helped improve the English of this dissertation. Besides the servo system in the industry, I also learned a great deal from him about life.

I deeply appreciate my girlfriend Ching Shang for her love and support. Among many other favors she has done for me, she helped proofread this dissertation.

Finally, my deepest gratitude goes to my parents, who devoted themselves to raising their children despite all the adverse conditions of the past decades. I could not have come so far without their love, support, and understanding.

Chapter 1

Introduction

This dissertation is concerned with the control algorithms for high-density hard disk drives (HDDs). The introduction chapter is organized as follows: the system overview is given in Section 1.1, in which Subsection 1.1.1 introduces the hard disk drive, and Subsection 1.1.2 introduces its servo system, performance factors, and related terminology. The problems to be addressed in the dissertation are described in Section 1.2. An overview of the previous research is given in Section 1.3. The contributions of the dissertation are described in Section 1.4. Section 1.5 outlines the contents of the dissertation.

1.1 System Overview

1.1.1 Hard Disk Drive

HDDs are the most important permanent storage used in computers nowadays. Components of a typical HDD are shown in Figs. 1.1 and 1.2. Other storage devices include floppy disks, CD-ROMs, tape drives, and removable mass storage such as Iomega
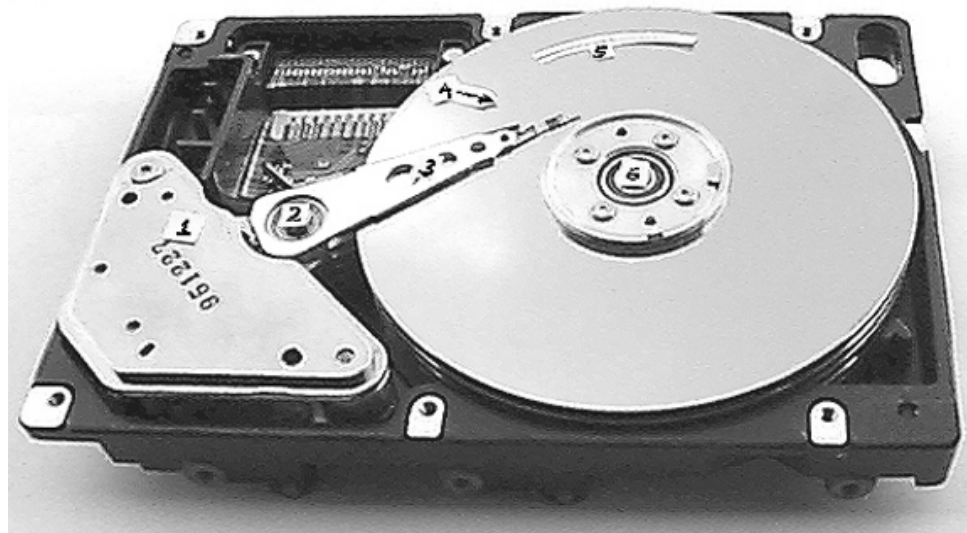
Figure 1.1: Inside a 3.5 inch hard disk drive: 1) VCM; 2) pivot bearing; 3) E-block; 4) suspension; 5) a track; and 6) spindle

ZIP and JAZ drives, and magneto-optical (MO) drives. HDD differs from others primarily in three aspects: capacity, cost per megabytes (MB), and performance. During the past 15 years, HDDs have made dramatic progress in terms of capacity, speed, and price. The first hard disks had a capacity of 10 MB, costing over $100 per MB. Nowadays, popular hard disks with tens of gigabytes (GB) cost less than a cent per MB. Meanwhile, their performance, reliability, and the data transfer-rate have been improved dramatically .

As shown in Figures 1.1, 1.2, and 1.3, HDD contains round, flat disks called *platters*, or *disks*. Information is stored on the magnetic coating of the disk surface. The disks have a hole in their center, and are stacked along a spindle. The stacked disks are rotated by an electric motor inside the spindle, called the *spindle motor*. Electromagnetic read/write (R/W) *heads* are used to either record information onto the disks or read information from them. The heads are mounted on *suspensions* through *gimbals*. Suspensions are mounted

Voice
coil motor

Spindle

Disk

Carriage

Flexible
printed
circuit

Suspension Recording head Tracks
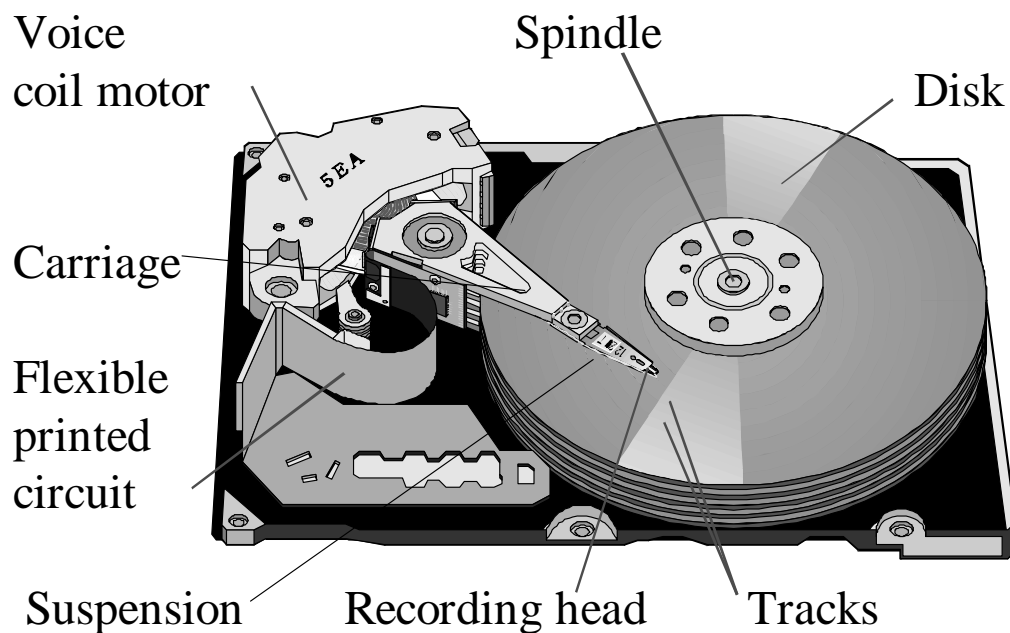
Figure 1.2: Hard disk components

on a *carriage*, or *E-block*, whose side view has an "E" shape. The heads, the suspensions, and the E-block together form the *Head Stack Assembly* (HSA). The flexible structure of the gimbals and the suspensions help the heads maintain constant flying height on an air bearing over the rotating disks. During the operation, the heads should never touch the rotating disks. Otherwise, the heads and the disk surface will be severely damaged. The R/W heads over the disk surface are positioned by an *actuator*, which controls the movement of HSA. *Voice coil motor* (VCM) is widely used as the actuator in hard disk drives. VCM controls HSA and a selected head to follow a track or to switch from one track to another.

In HDD, data are stored in tightly-packed concentric rings called *tracks*, and organized for fast access. Each track is further divided into smaller *sectors*. The stored data
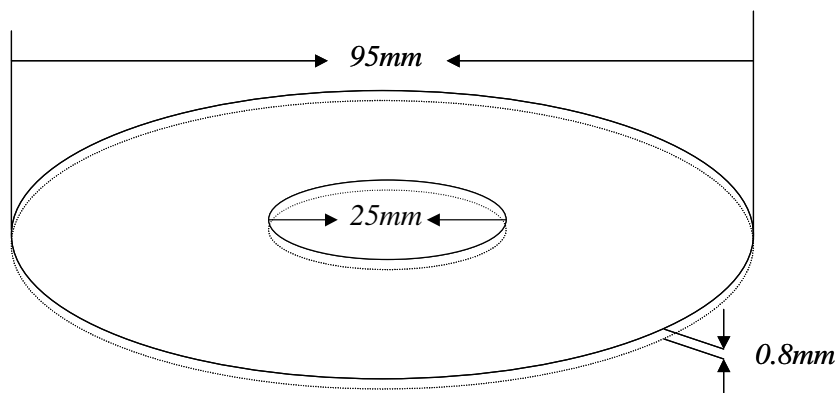
Figure 1.3: An industry standard 3.5 inch disk platter

are located by the cylinder, head, and sector numbers, which are provided to the servo subsystem by the interface controller when the host computer requests to access the data. With the cylinder and head number, the servo system controls the HSA to position the selected head to the target track center. The head then waits for the correct sector to begin access to the requested data.

Increase of HDD capacity is achieved by storing more information in the same physical disks, or increase of the *areal density* of the disks. Both bit density of tracks and track density of disks must be increased for higher areal density. The former is measured by bits per inch (BPI), and the latter by tracks per inch (TPI). Areal density, in bits per square inch ($BPSI$), is the multiplication of BPI and TPI.

Areal density is one of the most important factor for HDD performance. Increasing TPI is a relatively easier approach to increase the areal density [15], but still a challenging task itself. Historically, it involves cross-discipline technological advances in the magnetic media, actuators design, disk platter material and thickness, servo algorithms, and micro-

processors or DSP. This dissertation emphasizes the improvement of the HDD servo system.

1.1.2   HDD Servo System

The HDD servo system consists of two parts: the spindle motor servo system, and the actuator servo system. Both are real-time embedded systems. The disks rotate at a constant speed and the actuator moves over the disk surface. The task of the spindle servo is to keep the constant rotation speed. Historically, the spindle servo system has been well designed. This dissertation is mainly concerned with the actuator servo system. The term "servo system" in this dissertation refers to the actuator servo system unless otherwise stated.

The servo system calculates voltage command based on *position error signals* (PES) demodulated from *servo sectors*. The voltage command is then fed through an analog power amplifier (PA) via a DAC. The DAC acts as a zero-order hold (ZOH). The output current of PA passes the coils of the VCM, and the resulted torque drives the actuator for track following and seeking.

Figure 1.3 illustrates the widely used *embedded servo* scheme for HDDs. In the scheme, position signals are embedded in the servo sectors along the data tracks at equally spaced angles, with data sectors in between. R/W head reads sector number, track ID, and PES from the servo sectors. The number and the width of the servo sectors should be minimized for data format efficiency of HDDs. Servo sectors are pre-written on the disk before the disk can be used. *Servo writing* is performed by precision *servo writers*. Because the servo system uses the heads and servo sectors as the position sensor, the servo writers must achieve much higher positioning accuracy than the HDD servo system can do.
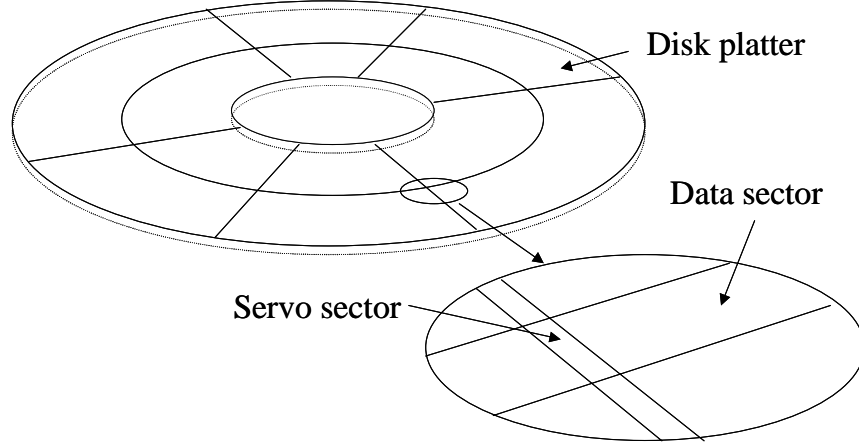
Figure 1.4: Servo sector and data sector in embedded servo system. Servo sectors provide R/W heads position information; data sectors store user data. The number of servo sectors per revolution and spindle speed determine the sampling rate.

Note that in Fig. 1.4, only 6 servo and data sectors are shown for illustration purpose. Commercial HDDs typically have more than a hundred sectors.

Figure 1.5 shows a simplified scheme of a servo sector. Assuming the head is moving from the left to the right, written in the servo sector are the *sector address mark* (SAM), gray code, ABCD bursts and optional RRO fields. SAM signals a coming servo sector and also indicates the sector number. The *gray code* provides the track number. *Bursts* are a group of magnetic written-in patterns with certain radial offsets. Each burst group has the width of a track. The position of the R/W head can be determined by the difference of the signal strength read back from these burst groups (A and B bursts shown). The relationship between the burst amplitude read back by the head and position of the head from the track center is given as

$$\Delta y_{pes} = W_r \frac{v_a - v_b}{2v_m} \qquad (1.1)$$
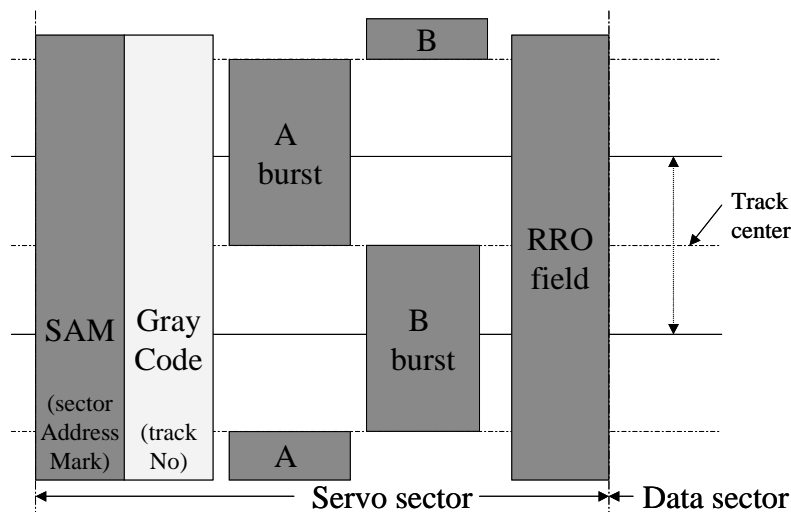
Figure 1.5: Schematic view of a servo sector, assuming R/W heads move from the left to the right in the schematic.

where W_r is the width of the read head; v_a and v_b are the amplitude of the A and B bursts read back by the head; v_m is the maximum amplitude for the bursts. Ideally, $v_a + v_b$ should be a constant. Note that in this two-bursts scheme, the maximum detectable position error is 25% of the track width. Usually, two or more bursts are used to increase the dynamic range and linearity of the PES. Optional *repeatable runout* (RRO) fields at the end of the servo sector can be used to store relevant information to correct the eccentricity of the servo sector center. Because the bursts are written by the servo writer, their radial positions also reflect the tracking errors. In general, the center of the bursts do not form a perfect circle. However, being the only position information sources in HDD, they are the reference trajectory for the R/W head to follow. The offsets of the bursts from a perfect circle are called *servo written-in errors*, which are deterministic and different for each track.

Figure 1.6 shows a common scheme to convert the analog signals read from the bursts to PES. The analog signals are conditioned by an adaptive filter, and then sent to an

analog-to-digital converter (ADC). The adaptive filter is used to attenuate the undesired media and electronic noises, and also anti-alias high-frequency noise. The servo digital signal processor (DSP) processes the results in digital format, and computes PES.
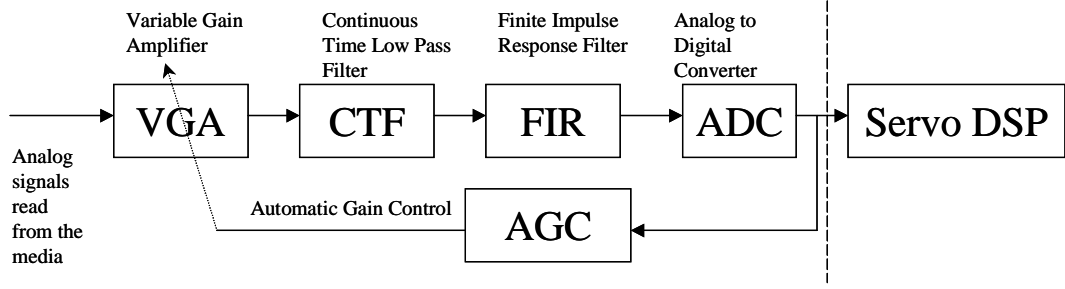
Figure 1.6: A typical hard disk drive read channel scheme. Continuous signals read from the media are conditioned before sent to servo DSP.

In an embedded servo system, PES can only be obtained in discrete-time format. Thus, its servo system is discrete in nature. The product of the spindle speed and the number of sectors determines its sampling rate, i.e.

$$F_s = N_{Sector} \frac{RPM}{60} \tag{1.2}$$

where F_s is the sampling rate in Hz, N_{Sector} is the number of the servo sectors along one track, and RPM is the spindle speed in revolution per minute.

The servo system of the disk drive plays a vital role to increase the internal performance of HDDs. Some key internal performance factors are explained as follow.

Seek time is the amount of time required for the read/write heads to move between tracks, normally in a order of milliseconds (ms). Average seek time is the average seek time from one random track (cylinder) to any other. *Track-to-track seek time*, or *track switch*

time is the amount of time that is required to seek between adjacent tracks. This can be less than 1 *ms*. *Full stroke seek time* is the amount of time to seek the entire width of the disk, from the innermost disk (ID) to the outermost disk (OD). Track seeking is a mechanical process that involves using the actuator to physically move the read/write heads. Track switch time is important because switches to adjacent tracks occur much more frequently than random seeks. With a fixed mechanical design, servo system is responsible for reducing seek time and track switch time, without increasing acoustics noises.

Latency is the amount of time that the R/W heads must wait to reach the target sector. The average latency is half the time of a full disk rotation. The worst case happens when the R/W head has to wait a full revolution to reach the target track. E.g., the average latency is 5.6*ms* for 5400 *RPM* drive, 4.2*ms* for 7200 *RPM*, and 2.8*ms* for 10*K RPM* drive. Increasing the spindle speed will reduce latency. Faster *spindle speed* also increases data transfer rate in a given BPI.

Areal density of a platter measures how many bits can be packed into each square inch. As mentioned before, areal density consists of two components: track density in TPI and bit density in BPI. The actuator servo system is responsible for maintaining the heads on-track near the center of increasingly narrowed tracks. [9][15]

Higher *RPM* and more sectors per track provide higher sampling rate. In general, higher sampling rate results in higher HDD internal performance. However, high *RPM* HDDs consume more power, generate more heat, and introduce more self-induced noises. High sampling rate servo system also demands faster DSP speed, and reduces the formatting efficiency. Trade-offs have to be made.

1.2   Problems Description

The areal density of HDD is growing at an astonishing rate at about 100% annually. Head/media technology is the most important enabling factor. Next, fast and accurate servo system is required to follow the TPI increase trend. The servo system must maintain the position of the read/write head on-track near the center of the target track in the following mode, and achieve fast and quiet head seek from one track center to another in the seeking mode.

Because of the different objectives in the seeking and the following modes, the control algorithms are often different in the two modes. The overall servo system then involves switches between algorithms. The scheme is referred to as mode switching control (MSC) [24].

There are usually two major issues in the MSC seek controller design: 1) mode switching conditions, and 2) velocity profiles.

Track seeking is required to be as fast as possible. Meanwhile, the transition from the seeking to the following mode is also required to be smooth to minimize the residual vibrations[65]. The vibrations may exacerbate the head settling, make the effective seek time longer, and cause acoustics problems. A settling mode is often used in between to smooth the transition.

The velocity reference profiles should utilize the full power, including the back e.m.f. effects, for the velocity control of the head. The ideal case is that at the end of the seek, the head velocity reaches zero, the head position is right above the target track center, and the VCM current is also zero.

The aforementioned two design requirements are very difficult to meet in MSC. Proximate time optimal servo (PTOS) [24] is usually used to design the velocity profiles. PTOS is based on a linear plant model of a rigid body. However, the plant is far more complicated. There are pivot friction, flexible cable bias, resonance modes, back e.m.f. effects, PA dynamics and saturation, electronic noises and power supply voltage variations. Those make the pure inertia plant model over-simplified. As a result, the velocity profiles and the mode switching conditions designed using rigid body model do not yield optimal head settling.

In MSC, the velocity profiles and the switching conditions are usually designed based on engineering experience, with a trial-and-error approach. Very often, conservative deceleration profiles are used for a slow transition at the mode switches, at the expense of the seek time.

The objective of the track following servo is to maintain the head along the track center precisely. If there were no noise in the servo system, and no servo written-in errors, the perfect tracking would happen and the PES would be consistently zero. Unfortunately, there are many imperfections in reality. Self-induced noises such as air turbulences, disk modes, and sensor noise are random signals by nature; servo written-in errors are deterministic noises. These are the sources contributing to PES consisting of both random and deterministic signals. The positioning accuracy or *track mis-registration* (TMR) is measured statistically in terms of the standard deviation σ of the PES. A typical specification is that 3σ be less than 10% of the track width, and less than 15% when the drive is subject to vibrations.

Without the detailed models of the self-induced off-track sources, or TMR sources, track following servo is traditionally designed heuristically in the frequency-domain. Some key criteria include phase margin, gain margin and open-loop cross over frequency. The design process usually begins before the real drives are built. Therefore, the time-domain performance can not be evaluated until prototype drives are built and the servo firmware is implemented. With the rapid increase in TPI and decrease in the time to market of HDD products, performance prediction and optimization of the track following servo for future products are desired and often crucial. However, these objectives have been difficult to achieve, mainly due to the lack of the accurate TMR source models, and systematic approaches to optimize the servo controller with various practical constraints.

1.3   Previous Research

IBM has been leading the research and development of the hard disk storage technologies for a few decades. In 1973, the IBM 3340 disk storage unit, known by its internal project name "Winchester", becomes the industry standard for the next decade. The disk drive features a smaller, lighter read/write head and a ski-like design that enables the head to fly closer to the disk surface on an air of film 18 millionths of an inch thick. The areal density was about 1.7 MB per square inch, compared with today's value at about tens of GB per square inch. A summary of the magnetic recording technology, including the servo technology, can be found in [45] and [46].

Franklin *et. al.* introduced the discrete-time track seeking servo for the hard disk in [24]. Pao and Franklin also presented and refined the time optimal control (TOS) and

Figure 1.7: IBM 3340 disk drive of 1973, known as the "Winchester" drive.

the proximate time optimal control (PTOS) for the track seeking in [48], [49], [50] and [51],

.

2DOF control belongs to the category of model-based control. In [19] and [56], Tomizuka presented an overview of the model based prediction, preview, and robust controls for motion control systems. The importance of accurate mathematical models of the controlled object and the disturbances was emphasized. He summarized that the overall tracking performance of the system can be significantly improved by feedforward controls, and the model-based adaptive and/or robust controls make it possible to realize high-performance, robust motion control systems. [54] and [55] described his work on the design of the digital tracking controllers, and introduced the zero phase error tracking controller (ZPETC) to solve the unstable zero problems [6]. Umeno and Hori implemented 2DOF control with disturbance observer (DOB) for the robust speed control of DC servomotors [29] [58]. Lee and Tomizuka implemented 2DOF control with friction compensation in [40] and [42]. Yi and Tomizuka investigated 2DOF control for mechanical system with flexible structures in [70] and [71].

Ishikawa *et. al.* investigated the use of 2DOF control for the head positioning for

low sampling rate sector servo HDDs [18]. A VCM model is used to derive the reference model, and the seek times are shortened. Yi, Hara, Hara and Tomizuka implemented a new reference generation method and a discrete DOB, as presented in [25], [72], and [73]. At the same time, White, Smith and Tomizuka studied the implementation of DOB for the track following controller in [62] and [63]; Ueda *et. al.* studied its implementation for flexible disk drives in [57]. Discrete DOB and its implementation for other industry applications were also discussed in [37] and [39].

Ishikawa used an accelerometer attached to the actuator to sense the pivot friction torque to compensate for the nonlinear friction effects [36]. White and Tomizuka attached an accelerometer on the disk drive base cover and implemented an adaptive feedforward control to reject external vibrations [61] [60]. In addition, several other model based adaptive friction compensation methods can be found in [5], [8], [13], and [17].

In 1995, Astrom and Wittenmark surveyed applications of adaptive control [7]. The only reference related to disk drive is [30] by Horowitz and Li. Their work on the adaptive control for disk drive track following servo are detailed in [31], [32], and [33]. Adaptive robust control (ARC) and its implementation on machine tools were presented by Yao, Al-majed, and Tomizuka in [66], [68], [69] and [67]. ARC differs from the conventional adaptive control in that it integrates the model-based robust control with the adaptation, and improves the adaptation speed.

The challenges to achieve high TPI were discussed in [9], [10], [16], [15], and [34]. White also examined the limitation of the TMR performance and the servo bandwidth due to sampling frequency and computational delays in [64].

The effects of disk modes on PES can be found in [44] and [35]. Abramovitch, Hust and Henze published a series of paper ([1], [2], [3] and [4]) studying the TMR models. The components level breakdown methods for TMR sources were presented. In [28], Ho Hai locked the actuator to estimate sensor noise and disk modes. All these methods are based on intrusive experiments where the drive cover must be at least partially opened. Lee and Guo modeled the TMR source using only PES and inversion of the sensitivity function, and lumped all the TMR disturbances at one location [41].

The repetitive controller used to attenuating repetitive disturbances was studied in [43], [38] and [11] for the track following mode. The transient behavior of the repetitive controller was investigated in [53].

TMR, seek and settle are the main criteria to evaluate the performance of a HDD servo system. For MSC, initial value compensation (IVC) at the mode switches to improve the settling was presented in [22] and [65]. Modified versions of PTOS have been used in the disk drive industry [51]. Studies to improve HDD seek performance can also be found in [52], [12], [23], [21], [20], [47], [27], [73], [72], and [25].

1.4 Contributions of this Dissertation

The contributions of this dissertation are as follows:

- Conventional MSC for the HDD servo system is often designed heuristically. The abrupt control input changes associated with the mode changes may exacerbate the settling of the R/W head. This dissertation proposes and implements 2DOF control for the HDD servo system. The unified 2DOF controller is applicable to both track

seeking and following modes, therefore making the mode changes in MSC unnecessary. In the 2DOF control, feedforward control is combined with DOB or ARC to enhance the servo performance.

- TMR source models have been difficult to characterize. This dissertation investigates the key characteristics of each major TMR source and shows how to characterize them. A simple method is derived to using only the raw PES data and servo system models. The characterized TMR source models are then available for servo algorithms development for HDDs with the same mechanical platform, i.e., same noise environment. They are also used later to optimize fixed-structure servo controllers for TMR performance.

- The proposed 2DOF control structure contains three major components: the reference generator, the feedforward controller, and the inner loop feedback controller. DOB and ARC are used as the inner loop controller. Although some of these components have been used in other industries, this is the first time for them to be integrated and implemented in HDD servo systems.

- A new reference generation method is proposed for the 2DOF control structure. The new reference profile is designed in two stages: off-line simulations to establish a base reference table, and on-line adjustments using the SMART (Structural vibration Minimized AcceleRation Trajectory) technique[47]. Simulations and experiments demonstrated that the 2DOF controller with this new reference generation method performs better than the PTOS. The improvement is achieved mainly in the deceleration period due to the use of back $e.m.f.$ effects.

- The effectiveness of DOB on track seeking is also validated by experiments using a Fujitsu disk drive. The implemented DOB achieved smaller tracking errors and faster seeks than the conventional PID controller. The effectiveness of ARC used for the 2DOF is also demonstrated by simulations.

- Conventional repetitive control and its constraints in HDD servo systems are discussed. A new position feedforward control using the servo sector RRO fields is proposed. The simulations show that TPI can be increased by 30%.

- Traditionally, design of fixed-structure servo controllers is based on engineering experience and trial and error. A systematic TMR optimization for fixed-structure controllers is proposed. The optimization is formulated to minimize the PES variance in the frequency-domain. The DFT magnitude sequences of the TMR sources are used as weighting sequences in the cost function. The noise environment is accurately represented in the optimization, and the order of the servo controller is not increased.

- The proposed TMR optimization method is applied to a PID controller and a DOB-based 2DOF controller. Physical intuitions of the tuning parameters are specially emphasized. One of the optimization parameters is the open-loop crossover frequency, also called open-loop bandwidth in HDD industry. The results show that an optimized DOB-based 2DOF controller achieved better TMR performance than that of an optimized PID controller. This is another advantage of the proposed 2DOF controller for HDD servo systems.

1.5   Outline of the Dissertation

The chapter has described the HDD servo system and related terminologies. The issues in the servo design have also been discussed. Chapter 2 first presents the modeling of the HDD servo system. TMR sources are discussed and their modeling based on raw PES data is presented. Chapter 3 introduces and describes 2DOF control. The 2DOF controller with a DOB is implemented for HDD in Chapter 4. Chapter 5 covers the conclusion and the proposed research projects.

Chapter 2

System Modeling

This chapter describes the modeling of HDD system. The design specifications for HDD servo system are given in Section 2.1. Plant modeling is discussed in detail in Section 2.2. TMR sources and the noise environment in which the servo system operates are described in Section 2.3. The TMR sources include repeatable components, such as servo written-in errors, and non-repeatable components, such as sensor noise, torque disturbances, and disk modes. Techniques to identify servo written-in errors are described in Section 2.3.1. Characterization of the non-repeatable components in frequency-domain is presented in Section 2.3.2, 2.3.3, and 2.3.4. This chapter is summarized in Section 2.4.

2.1   Servo Design Specifications

Commonly used deign specifications for HDD servo systems are listed as follows:

1. Minimal $5dB$ gain margin and $30°$ phase margin;

2. Asymptotic tracking of step position commands;

3. Minimal transition time for track seeking;

4. Minimal TMR for track following.

Stability margins are covered in Criterion 1. Due to the mass production of disk drive components, variation and uncertainties from the plant model are expected and must be accounted for in the servo system design. The gain margin indicates how much loop gain variation can be tolerated before the system falls into instability. The phase margin determines the stability impact from phase loss caused by computation delay and high-frequency actuator resonances. The margin values given in the specifications are typical design objectives[64]. Criterion 2 concerns the ability to reject constant torque disturbances, such as the bias torque from the flexible printed circuit (FPC). The seek and tracking performance is reflected in Criterion 3 and 4, respectively.

2.2 Hard Disk Servo Plant Modeling

For a single stage actuator HDD, the plant consists of power amplifier (PA), voice coil motor (VCM) and head stack assembly (HSA). The servo system is usually implemented by a digital signal processor (DSP). The DSP processes PES, computes and generates voltage command via a DAC. With the command, the PA controls the coil current and torque to move the HSA.

The PA and the VCM models are shown in Fig. 2.1, in which HSA is modeled as a pure inertia with resonance modes, and VCM is modeled by $\frac{1}{Ls+R}$. L is the coil inductance. $R = R_s + R_m$. R_m is the coil resistance, and R_s is the current sensor resistance providing the current information. Voltage u_2 across VCM generates the coil current i. Torque $T = K_t i$,
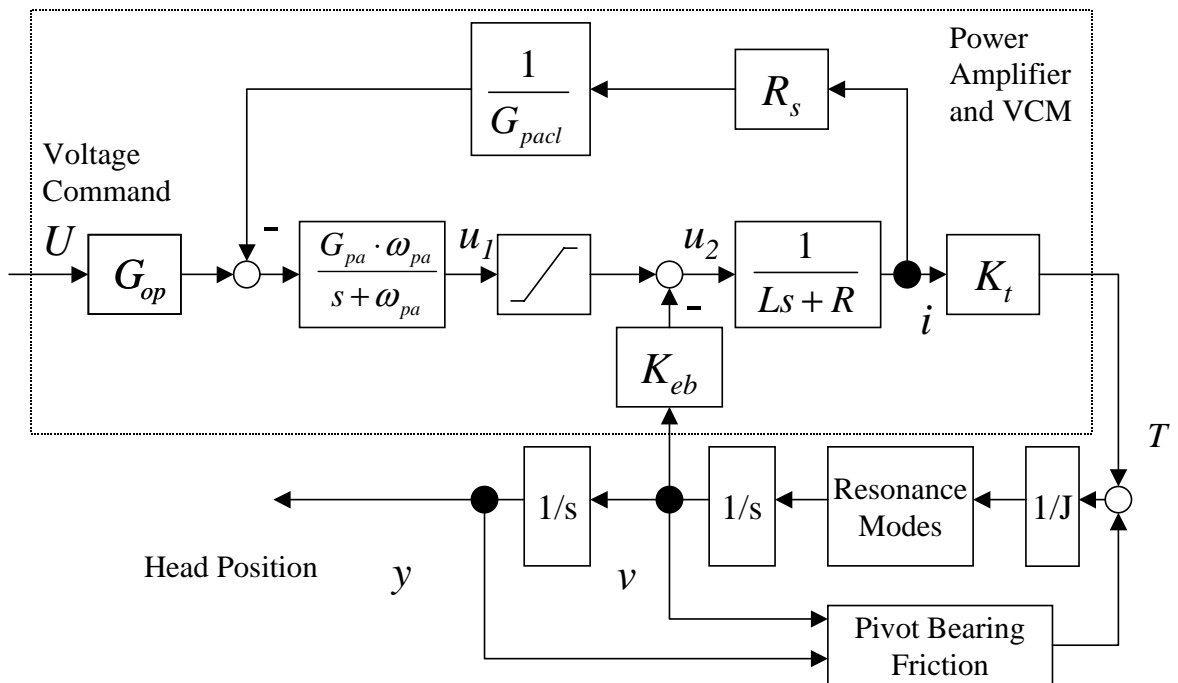
Figure 2.1: An actuator plant model consists of voice coil motor (VCM), power amplifier (PA), and head stack assembly(HSA). The PA itself is a closed-loop servo. PA saturation is also modeled. Resonance modes include actuator lateral mode and suspension torsional mode.

where K_t is the torque constant. VCM voltage is also affected by the back $e.m.f.$ voltage, which is proportional to the coil velocity v. $K_{eb} = K_t$. In the PA, an analog feedback loop controls the VCM current i to follow the voltage command U. The PA op-amp is modeled as a first-order system with a cutoff frequency ω_{pa} with a very large gain G_{pa}. In practice, the dynamics of PA is often ignored and substituted with a constant gain, given as follows:

$$i = \frac{G_{pacl}G_{op}}{R_s}U \tag{2.1}$$

G_{pacl} and R_s are the determining parameters inside the feedback loop. G_{op} is the tuning parameter outside the loop.

The dynamics of the PA is described as:

$$\dot{u}_1 = -\omega_{pa}u_1 + \omega_{pa}G_{pa}\left(G_{op}U - \frac{R_s}{G_{pacl}}i\right) \tag{2.2}$$

$$\dot{i} = \frac{1}{L}\left(sat\left(u_1\right) - K_{eb}v - Ri\right) \tag{2.3}$$

Ignoring the PA saturation and back $e.m.f.$ effect, the transfer functions from $U(s)$ to $i(s)$ and $v(s)$ to $i(s)$ are given as follows:

$$\frac{i(s)}{U(s)} = \frac{G_{pa}\omega_{pa}G_{pacl}G_{op}}{(s+\omega_{pa})(Ls+R)G_{pacl} + G_{pa}\omega_{pa}R_s} \tag{2.4}$$

$$\frac{i(s)}{v(s)} = \frac{-G_{pacl}(s+\omega_{pa})K_{eb}}{(s+\omega_{pa})(Ls+R)G_{pacl} + G_{pa}\omega_{pa}R_s} \tag{2.5}$$

Using the final value theorem, it is easy to show that the DC gains of Eqs. 2.4 and 2.5 are:

$$K_{pau} \;\;=\;\; \frac{G_{pacl}G_{op}}{\frac{RG_{pacl}}{G_{pa}} + R_s} \tag{2.6}$$

$$K_{pav} \;\;=\;\; \frac{-K_{eb}G_{pacl}}{RG_{pacl} + G_{pa}R_s} \tag{2.7}$$

where K_{pau} is the DC gain from U to i, and K_{pav} is the DC gain from the HSA velocity v to i. Usually G_{pa} is much larger than RG_{pacl}, and R_s is small. In the ideal situation with infinite G_{pa} and no op-amp saturation,

$$K_{pau} \;\;=\;\; \frac{G_{pacl}G_{op}}{R_s} \tag{2.8}$$

$$K_{pav} \;\;=\;\; 0 \tag{2.9}$$

In this case, the PA is modeled as a constant gain, and the back $e.m.f.$ has no effect on the current.

The parameters to model a HDD plant are shown Table 2.1, by example of a Fujitsu SCSI HDD model M2954. The same drive is also used in [25] and [73]. The resonance models listed in the table are simplified examples but typical for general HDD actuators.

Major HSA resonances include suspension torsional modes and actuator lateral modes, which can be modeled as second-order systems. The first suspension torsional mode, also referred to as butterfly mode at 2500 Hz, is shown in Fig. 2.2. The actuator lateral mode at $3.4KHz$ is shown in Fig. 2.3. The phase loss caused by the lateral mode imposes great challenges to increasing the servo bandwidth.

The pivot friction is a complicated nonlinear phenomenon. It is often simply modeled as a linear resonance by a second-order system. Figure 2.4 shows HSA Bode plots

Modeling Parameters	Symbol	Value
Track density	TPI	$6438.5\,track/inch$
Spindle speed	RPM	$7200\,rev/Minute$
Sampling time	T_s	$67.2\,\mu s$
Sampling rate	Fs	$14880\,Hz$
Length from pivot center to head	L_{arm}	$0.052\,m$
VCM coil resistance	R_m	$8.02825\,\Omega$
Current sensor resistance	R_s	$0.4875\,\Omega$
VCM coil inductance	L	$1.24 \times 10^{-3}\,H$
Back e.m.f.	K_{eb}	$8.976 \times 10^{-2}\,Vs/rad$
Torque constant	K_t	$8.976 \times 10^{-2}\,Nm/A$
Moment of inertia	J	$5.957 \times 10^{-6}\,Kgm^2$
Closed loop PA gain	G_{pacl}	0.8
PA op-amp gain	G_{pa}	250
PA closed-loop gain adjustment	G_{op}	0.56
Op-amp maximum voltage output	$U_{\max}$	$9\,V$
Actuator lateral mode frequency	f_{LM}	$3400\,Hz$
Suspension torsional mode frequency	f_{TM}	$2500\,Hz$
Pivot friction resonance frequency	f_{pf}	$50\,Hz$
Pivot friction damping coefficient	ζ_{pf}	0.2

Table 2.1: M2954 plant parameters
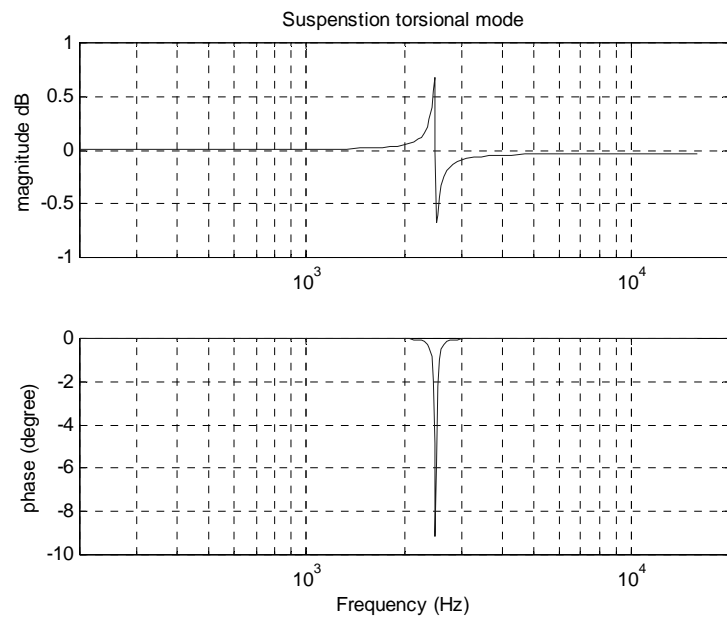
Figure 2.2: Suspension torsional mode at $2.5KHz$ with normalized DC gain.
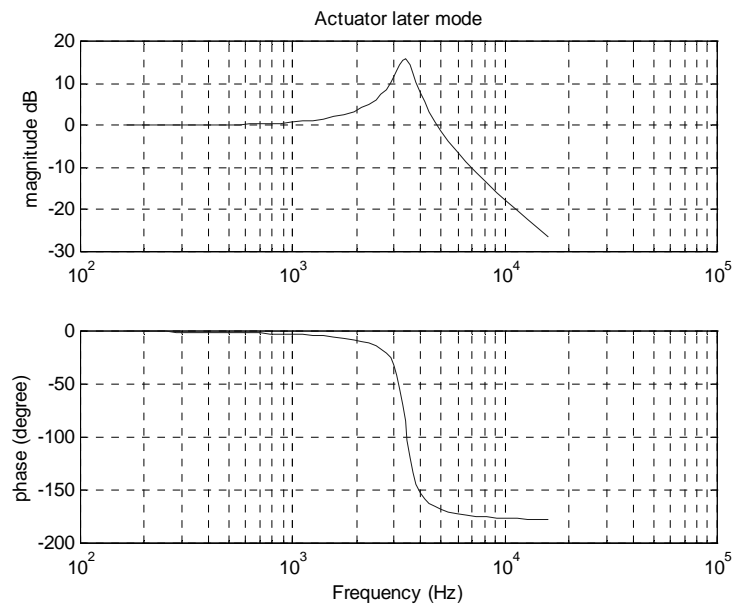
Figure 2.3: Actuator lateral mode at $3.4KHz$ with a normalized DC gain.

with and without the linear model for the pivot friction. The pivot friction limits the open-loop gain at low frequencies, and makes the system more susceptible to disturbances.
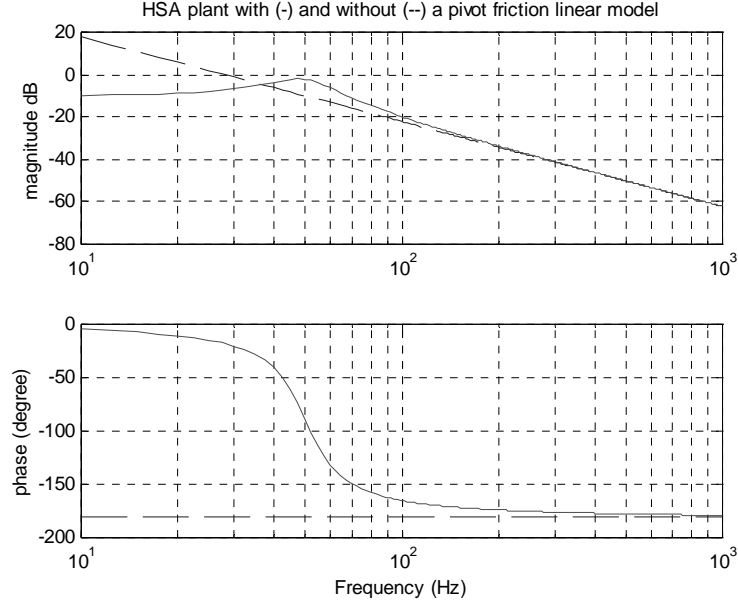
Figure 2.4: Modeling pivot friction for HSA. Without the friction, the plant shows a double integrator characteristics. A resonance mode at $50Hz$ is used here to model the pivot friction.

Ignoring the resonance modes, the state-space equations describing the plant are:

$$\dot{y} = v \tag{2.10}$$

$$\dot{v} = -(2\pi f_{pf})^2 y - 4\zeta_{pf}\pi f_{pf} v + \frac{K_t}{J} i$$

$$\dot{i} = \frac{1}{L}\left(sat\left(u_1\right) - K_{eb} v - R i\right)$$

$$\dot{u}_1 = -\omega_{pa} u_1 + \omega_{pa} G_{pa}\left(G_{op} U - \frac{R_s}{G_{pacl}} i\right)$$

In general, not all high-frequency resonances can be ignored in the HDD servo design. Plant models with and without the lateral and the torsional resonances are illustrated

in Fig. 2.5. The introduced phase loss by these resonances limit the potential to increase the open-loop bandwidth.

The plant model (2.10) is already a fourth-order system without any resonance model. Its order can be reduced by using the simplified PA model (2.1). The bandwidth of PA is much higher than that of HSA. This holds true when the PA operates in its linear mode during track following and non-saturated seeking. For the $M2954$ drive, $\frac{i(s)}{U(s)}$ and $\frac{i(s)}{v(s)}$ are lowpass filters with cutoff frequencies higher than $10\ KHz$, and can be substituted with constant gains given by (2.4) and (2.5). Ignoring the resonances and the PA dynamics, the plant model is described as:

$$
\begin{aligned}
\dot{y} &= v & (2.11)\\
\dot{v} &= -\left(2\pi f_{pf}\right)^2 y - \left(4\zeta_{pf}\pi f_{pf} - K_{pav}K_t\right)v + \frac{K_t}{J}K_{pau}U
\end{aligned}
$$

The lateral and torsional modes can then be cascaded with the system of (2.11). Figure 2.6 shows Bode diagram comparison between plant models with and without the PA dynamics. They begin to differ from about $4KHz$. Because typical HDD servo bandwidth is less than $1KHz$, PA dynamics has little effects on the stability margins. Thus, the dynamics is reasonably safe to be ignored during the initial stage of the servo design.

As mentioned before, the DSP generates analog voltage commands via a DAC, which is modeled as a ZOH. Because the servo system is inherently discrete, the continuous-time plant is discretized using the ZOH method for servo design and performance evaluation. The transfer function of the ZOH is
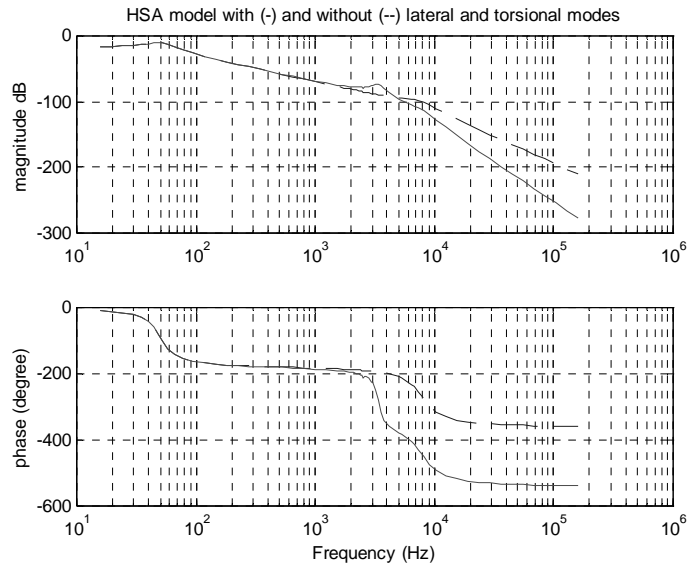
Figure 2.5: Plant model with and without lateral and torsional modes. Power amplifier dynamics are included in both models. The resonance modes caused phase loss at high frequency, in addition to that resulted from the power amplifier dynamics in both models.
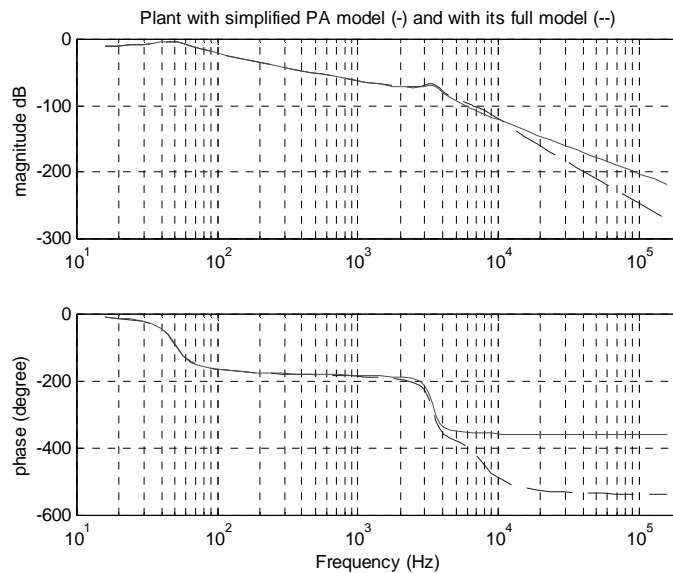
Figure 2.6: Modeling comparison between using power amplifier full model and its simplified constant gain model. Difference beginning from $4KHz$ includes additional phase loss and faster gain roll-off with power amplifier dynamics.

Bode Diagrams of Plant models (continuous "-" and discrete "--")
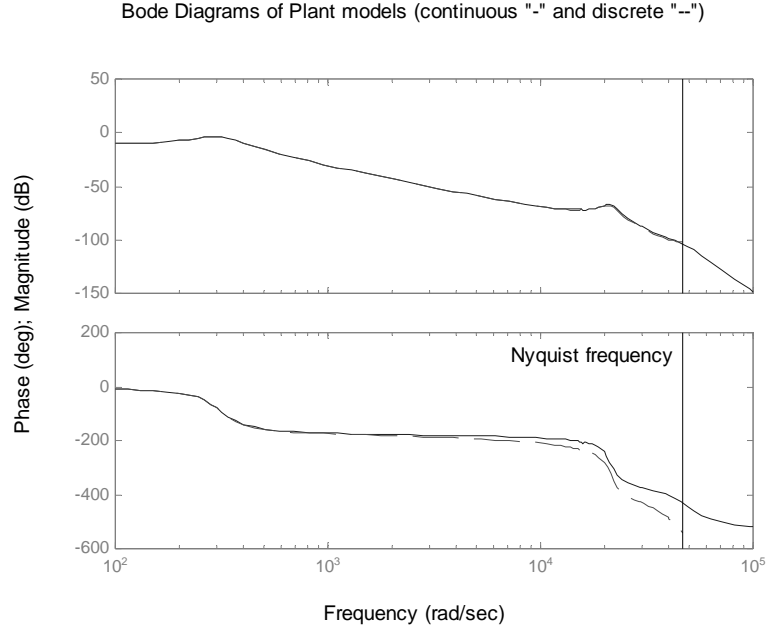
Figure 2.7: Frequency response of plant models, continuous, and discrete using zero order hold method. At the Nyquist frequency, the phase loss caused by the discretization is 90°.

$$G_{zoh}(s) = \frac{1 - e^{-T_s s}}{s} \qquad (2.12)$$

where $T_s = \frac{1}{F_s}$ is the servo sampling time. The sampling rate F_s is determined by the spindle speed and the number of sectors per revolution, as shown in Eq. 1.2. The continuous- and discrete-time plant models for $M2954$ are shown in Fig. 2.7.

The magnitude and phase change introduced by ZOH are $\frac{\sqrt{2-2\cos\omega T_s}}{\omega}$ and $-\frac{\omega T_s}{2}$, respectively[24], where ω is the frequency in rad/s. The gain of the ZOH decreases as it nears the Nyquist frequency, and the phase loss is proportional to the frequency. The maximum phase loss is $\frac{\pi}{2}$ or 90 degrees at the Nyquist frequency. As it can be seen from Fig. 2.7, the magnitude impact is small enough that the ZOH is often modeled as a simple

delay of $T_s/2$ [24]. Besides the resonances, the sampling frequency and the computation

delay also limit servo bandwidth. [64]
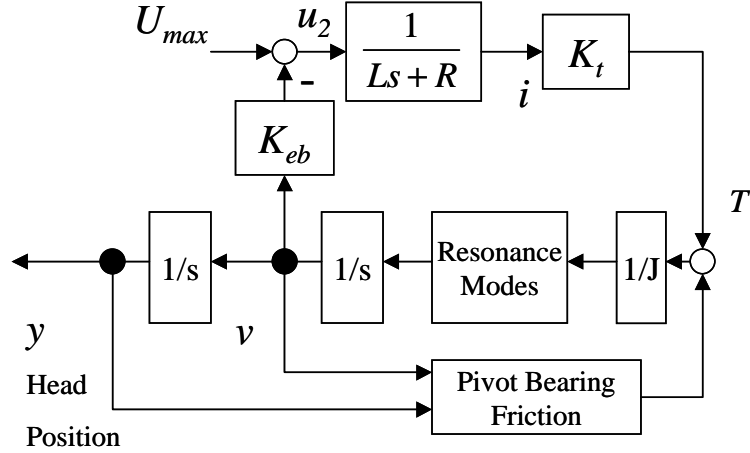
Figure 2.8: Plant model during PA saturation. VCM current feedback loop has no effect on the voltage applied across the its coil

Plant model during the power amplifier saturation is shown in Fig. 2.8. The

saturation commonly occurs during the acceleration phase of a long seek. In this case, the

maximum voltage is applied to the PA. $U_{\max}$ is the maximum op-amp voltage output. The

plant is completely different from that with the op-amp operating in its linear range. In

saturation mode, the PA current feedback loop has no effects on $U_{\max}$.

For track following control, the PA operates in its linear range without saturation.

The PA bandwidth is usually ten times higher than servo bandwidth. As a result, for servo

design and TMR analysis, the PA dynamics is often simplified as a constant gain. However,

the it need to be included in the plant model for servo system performance evaluation.

The discrete-time system model is shown in Fig. 2.9. The plant model $P\left(z^{-1}\right)$

is a ZOH equivalence of the continuous-time plant model given in Eq. 2.10 or 2.11 with
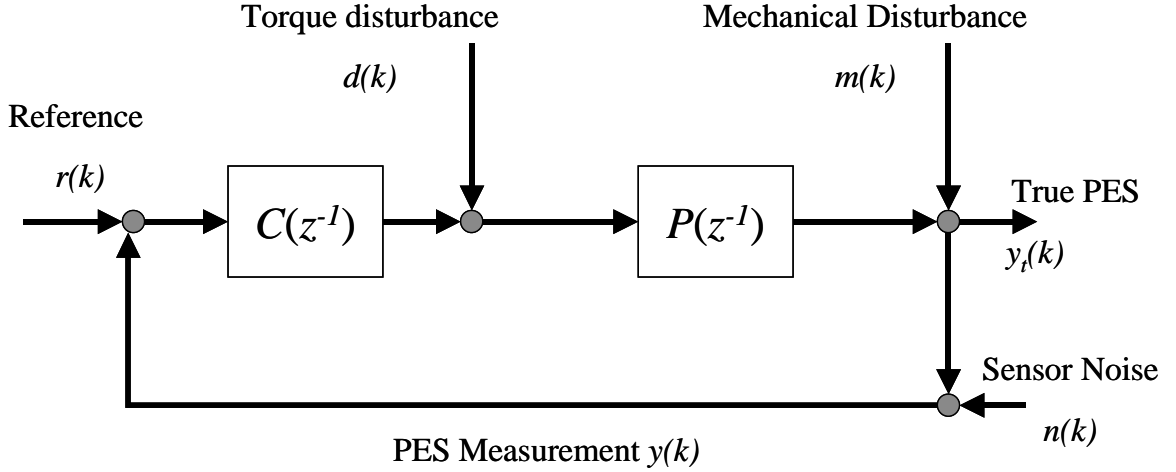
Figure 2.9: Servo system model for track following.

resonance modes augmented. Discrete servo controller $C\left(z^{-1}\right)$ is typically a PID or a state-space controller. Sensitivity function $S\left(z^{-1}\right)$, closed-loop or complementary sensitivity function $T\left(z^{-1}\right)$ and disturbance transfer function $D\left(z^{-1}\right)$ of the system are defined as follows:

$$S\left(z^{-1}\right) = \frac{1}{1 + P\left(z^{-1}\right)C\left(z^{-1}\right)} \tag{2.13}$$

$$T\left(z^{-1}\right) = \frac{P\left(z^{-1}\right)C\left(z^{-1}\right)}{1 + P\left(z^{-1}\right)C\left(z^{-1}\right)} = 1 - S\left(z^{-1}\right) \tag{2.14}$$

$$D\left(z^{-1}\right) = \frac{P\left(z^{-1}\right)}{1 + P\left(z^{-1}\right)C\left(z^{-1}\right)} \tag{2.15}$$

The sensitivity function $S\left(z^{-1}\right)$ is often referred to as the error rejection function; $T\left(z^{-1}\right)$ is the closed-loop transfer function; and $D\left(z^{-1}\right)$ is the disturbance transfer function.

The Bode's integral theorem for discrete-time systems was derived in [14]. It states that for all closed-loop stable discrete-time feedback systems, the sensitivity function has

Controller Gain	Value
K_p	0.04
K_d	0.3
K_i	0.001

Table 2.2: M2954 controller parameters

to satisfy the following integral constraint:

$$\sum_{i=1}^{m} \ln |\beta_i| = \frac{1}{\pi} \int_0^{\pi} \ln \left| S\left(e^{j\phi}\right) \right| d\phi \tag{2.16}$$

where β_i are the open-loop unstable poles of the system, m is the total number of these poles, and ϕ is the normalized frequency to make the Nyquist frequency π.

The HDD open-loop systems are always designed to be stable, i.e. $m = 0$,

$$\int_0^{\pi} \ln \left| S\left(e^{j\phi}\right) \right| d\phi = 0 \tag{2.17}$$

In the frequency region where $\left| S\left(e^{j\phi}\right) \right| > 1$, the noise is amplified, while in the region where $\left| S\left(e^{j\phi}\right) \right| < 1$, it is attenuated. (2.17) implies that the total area under the sensitivity function magnitude (in log scale) is zero. This is referred to as the waterbed effect, because pushing down the sensitivity function in certain regions results in rising it up in some other regions.

For illustration purpose, a typical PID controller with a cascaded notch filter is used for track following with the M2954 plant model. The controller is given by:

$$C_{PID}(z^{-1}) = K_p + K_d \left(1 - z^{-1}\right) + \frac{K_i}{1 - z^{-1}} \tag{2.18}$$

and its gains are given in Table 2.2.

The Bode diagrams of $C(z^{-1})$ and $P(z^{-1})$ are shown in Fig 2.10. The derivative action at high frequencies adds phase lead to compensate the plant phase loss, and the integral action increases the open-loop gain for low frequencies disturbance rejection. A notch filter

$$C_{NF}(z^{-1}) = \frac{0.6145 - 0.1603z^{-1} + 0.5038z^{-2}}{1 - 0.2275z^{-1} + 0.1855z^{-2}} \tag{2.19}$$

is cascaded with the controller $C_{PID}(z^{-1})$. The overall servo controller is

$$C(z^{-1}) = C_{PID}(z^{-1})C_{NF}(z^{-1}) \tag{2.20}$$

Figure 2.10 shows the controller and the plant with resonance modes . The notch filter is used to lower the gain caused by them. Bode diagrams and Nyquist plots of the open-loop servo without the notch filter are shown in Figs. 2.11 and 2.12, respectively. Those with the notch filter are shown in Figs. 2.14 and 2.13, respectively. Without the notch filter, the open-loop gain exceeds 0 dB at the resonance frequency at $3.4KHz$. Although the system is still stable under the situation, the stability margin is reduced significantly. Comparing Fig. 2.13 with Fig. 2.12, it can be seen that the Nyquist plots without the notch filter are much closer to the critical point $(-1, 0)$.

Also shown in Fig. 2.14 are the phase and gain margins. They are $5.6dB$ and $30.6°$, respectively. This meets the requirement on the servo stability margins stated in Section 2.1.

The asymptotic tracking of a step position command requires a unit closed-loop DC gain, or

$$T\left(z^{-1}\right)|_{z=1} = 1 \tag{2.21}$$
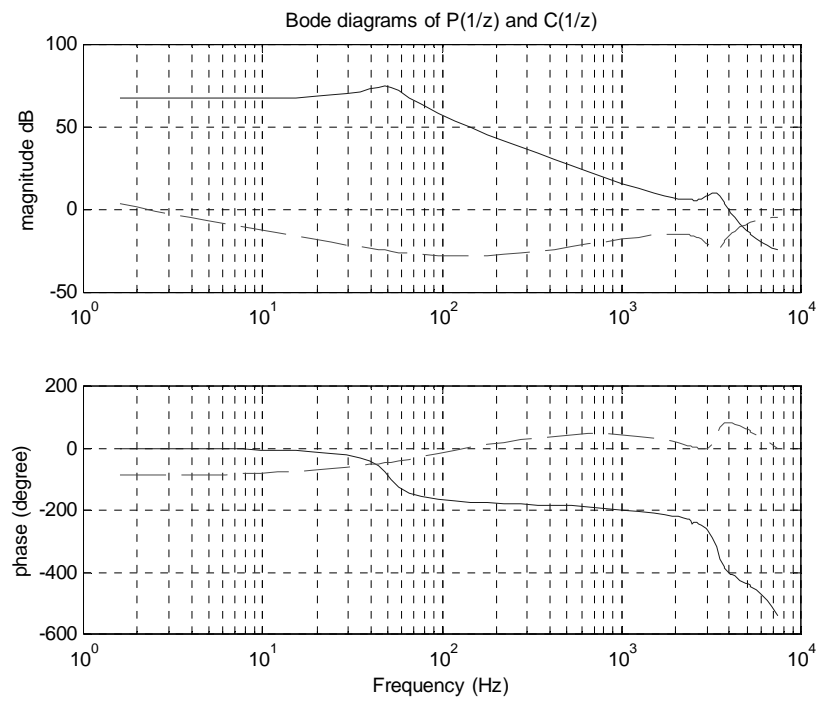
Figure 2.10: Bode diagrams of the controller and the plant for the Fujitus M2954 disk drive
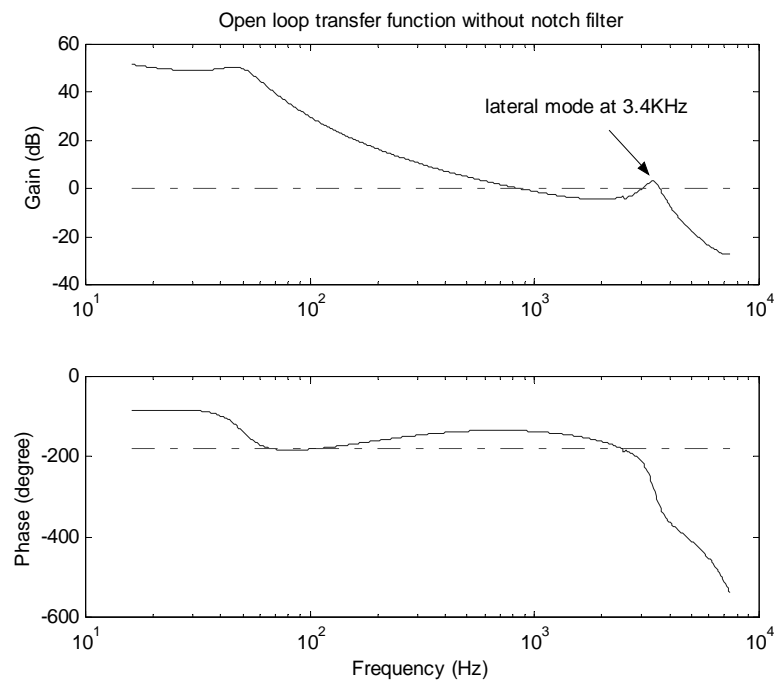
Figure 2.11: M2954 open loop bode diagram without a notch filter in the controller
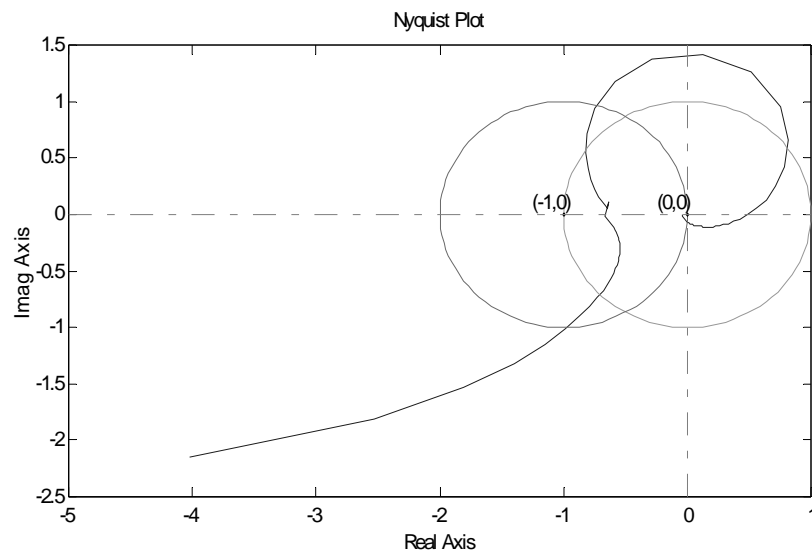
Figure 2.12: M2954 Nyquist plot without a notch filter in the controller
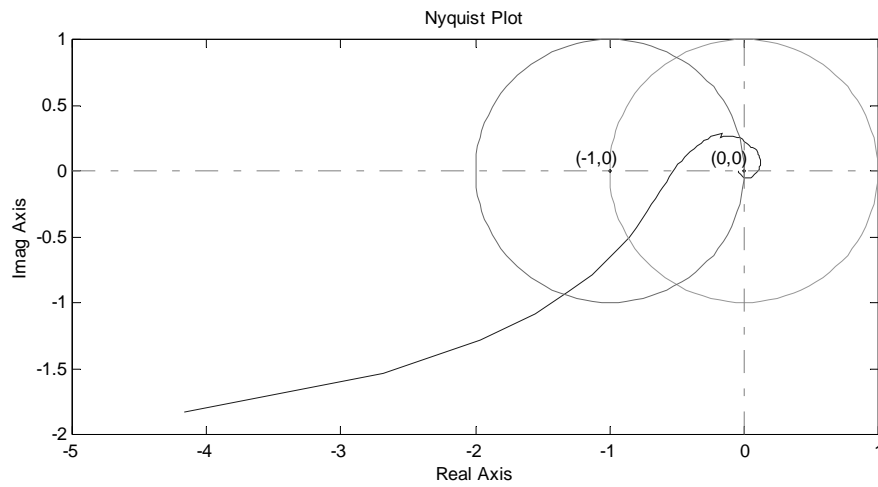
Figure 2.13: M2954 Nyquist plot with a notch filter in the controller
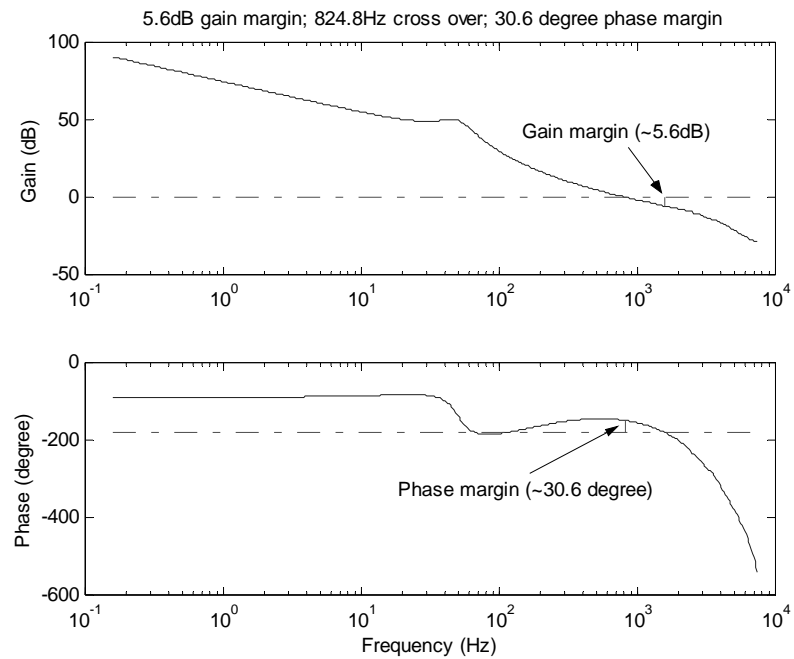
Figure 2.14: M2954 open loop Bode diagram with a notch filter in the controller. Its gain margin and phase margin meet the $5dB$ and $30°$ stability margin servo design requirement.

It also implies that the constant torque disturbances be rejected. This requires:

$$D\left(z^{-1}\right)|_{z=1} = 0 \tag{2.22}$$

Both (2.21) and (2.22) require infinite gain of the compensator at low frequencies. Typically, an integrator is added to the servo loop to achieve it. The effect of the integral control is demonstrated by comparing two servo designs for $M2954$: one uses a PID controller with the parameters in Table 2.2, the other one uses a PD controller with the same parameters, except $K_i = 0$. Both controllers use the same notch filter described in Eq. 2.19. The resulted closed-loop transfer functions are shown in Fig. 2.15. Although it is hard to tell the difference visually, numerical calculations show that the DC gain of $T\left(z^{-1}\right)$ with the PID controller has a unit gain, while that of the PD controller is 0.9892. Bode diagrams of the sensitivity functions and the disturbance transfer functions are shown in Figs. 2.16 and 2.17, respectively. The comparison studies show that only the PID controller meets the required design specification on the ability to reject constant disturbances.

HDD seek performance will be discussed in Chapter 4. TMR performance analysis and evaluation require accurate TMR source models, which will be discussed in the next section.

2.3   TMR Source Models

As explained before, the nominal model of a HDD plant can be analytically obtained given its mechanical platform. However, the servo system consists of not only the plant, but also the noise environment in which it operates. Without noise, perfect track following would have been achieved. The noise environment is examined and characterized
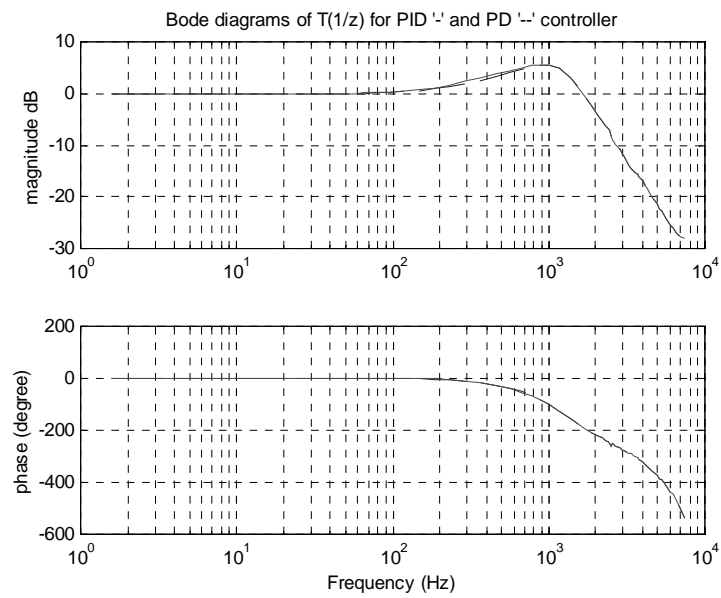
Figure 2.15: M2954 closed loop transfer function using PID and PD controllers
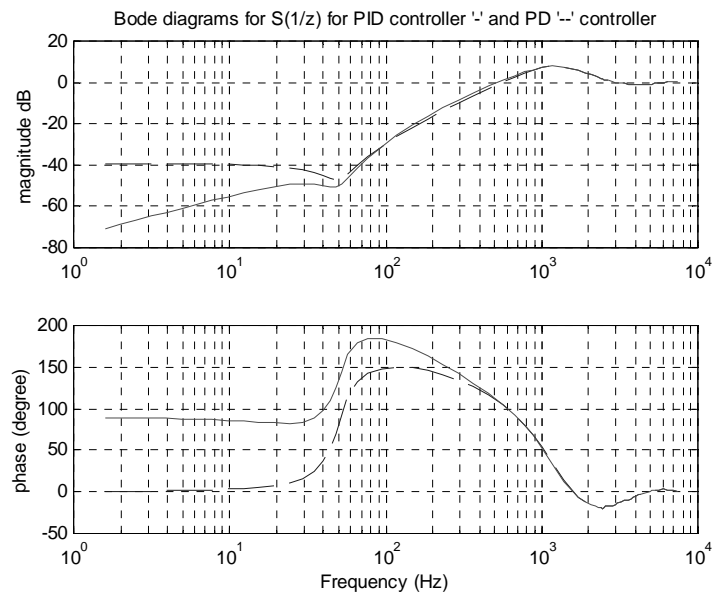
Figure 2.16: M2954 sensitivity function for PID and PD controllers
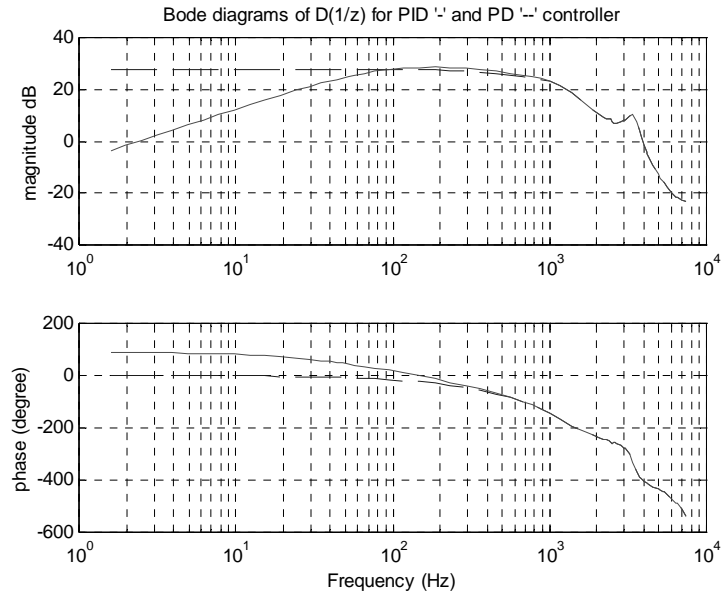
Figure 2.17: M2954 disturbance transfer function for PID and PD controllers

in two steps in this section. The first is to conduct open-drive experiments to examine and verify TMR source models, and the second step is to characterize the models from only raw PES.

Off-track PES are typically measured in terms of their standard deviation σ. It is usually required that 3σ be less than 12% of the track width under normal operating condition, and less than 15% under vibrations. The requirement is called TMR budget. There are two approaches to achieve the TMR budget, either by reducing the TMR at their sources, or attenuating PES via the servo system. Reducing TMR at their sources often require costly and time-consuming re-designs of mechanical platforms or electronics. The servo design, usually involving only firmware changes, is always given a high priority for meeting the TMR budget.
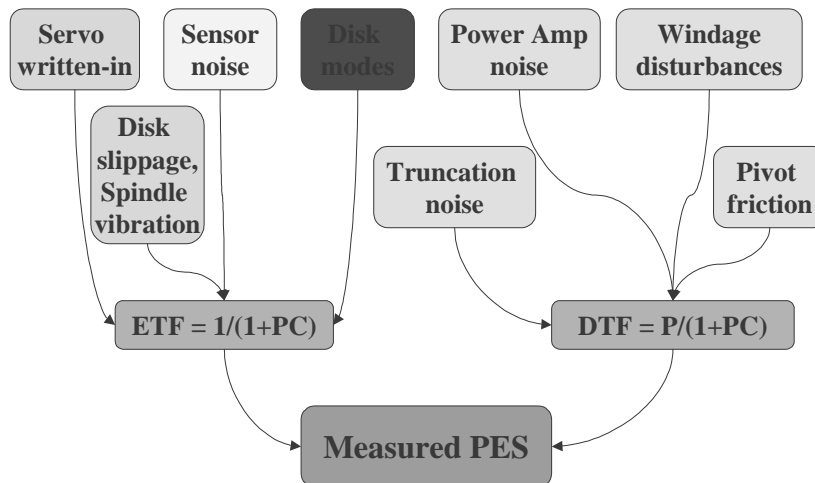
Figure 2.18: Major TMR sources contributing to the on-track PES.

TMR components can be categorized according to three different criteria [16]: 1) repeatable PES (RPES) with a fundamental spindle frequency content and its harmonics, and non-repeatable PES (NRPES) with a broad band frequency contents; 2) Seek-TMR, caused by residual mechanical vibrations after a seek, and on-track TMR, caused by noise sources in the track following mode; and 3) externally-induced TMR, caused by external shocks and vibrations, and self-induced TMR, caused by internal noise sources such as air turbulences, sensor noise, and mechanical vibrations of the disks.

Accurate TMR source models are desired for new product TPI prediction and servo performance evaluation. Without the models, the prediction and evaluation have to wait for the new HDD prototypes and firmware. TMR sources can be experimentally identified by direct measurement and/or analysis on their effects on PES ([1], [2], [3], [4], and [28]). However, the required open-drive experiments are intrusive, costly, and time-consuming. This makes it difficult to collect statistical information for accurate TMR source models.

As shown in Figs. 2.18 and 2.9, major TMR sources are categorized into four major components: servo written-in errors, disk modes, sensor noise, and torque disturbances. The first three affect PES through the sensitivity function, and the last one through the disturbance transfer function.

It has been noticed that the power spectrum of various TMR sources varies little from drive to drive with same mechanical platforms. This motivates a method to characterize the TMR sources based on only raw PES and *a priori* knowledge of the servo system. TMR sources are first investigated through open-drive experiments. The results are used to validate the proposed TMR source modeling method. The components breakdown procedures are presented along with the methodology development.

2.3.1 Process PES in Time-Domain and Frequency-Domain

This section discusses the methods to process PES in both time-domain and frequency-domain. RPES is a deterministic value at each servo sector, and can be estimated by the mean of the PES read from the specific sector. NRPES can then be obtained by removing the RPES from the PES. It will show later in Fig. 2.21 that the NRPES can be modeled as a zero mean Gaussian random process.

PES from a commercially available HDD are collected and processed to illustrate the procedures. The drive has 120 sectors per track, and $20K$ TPI. The PES collection is from one head at three locations at ID, MD, and OD. At each location, 8192 points PES are collected 10 times. One collection (8192 points) of PES at OD are shown in Fig. 2.19,

Modeling Parameters	Symbol	Value
Track density	TPI	$20000\,track/inch$
Spindle speed	RPM	$5400\,rev/Minute$
Sectors per rev	$Sector$	120
Arm distance	L_{arm}	$0.052\,m$
Back e.m.f. coefficient	K_{eb}	$7.57 \times 10^{-2}\,Vs/rad$
Torque constant	K_t	$7.57 \times 10^{-2}\,Nm/A$
Moment of inertia	J	$5.7 \times 10^{-6}\,Kgm^2$

Table 2.3: Drive model used for TMR analysis

in units of percentage of a track width.

Time-Domain Analysis

As introduced in Section 1.1.1, the PES contains deterministic RRO components: RPES, and random NRRO components: NRPES. The first step to process PES is to determine RPES. As a part of the mechanical disturbances $m(k)$ as shown in Fig. 2.9, the servo written-in errors affect PES through the sensitivity function $S\left(z^{-1}\right)$.

In the first plot in Fig. 2.19, 68 revs of PES are overlaid on the 120 servo sectors. RPES $y_{r1}(n)$ for one revolution are given by:

$$y_{r1}(n) = \frac{\sum_{k=1}^{N_r} y\left((k-1)N_s + n\right)}{N_r}, \; n = 1, 2, ..., N_s \tag{2.23}$$

where $y(i)$ is the ith point in the PES collection, N_s is the number of sectors per rev, and N_r is the complete revs in the collection. $y_{r1}(n)$ is shown in the second plot in Fig. 2.19. Standard deviation of the estimation is also provided. RPES $y_r(k)$ can be obtained by duplicating one rev RPES $y_{r1}(n)$ to all other revs within the collection length N by:

$$y_r(k) = y_{r1}\left(\mathrm{mod}\left(\frac{k}{N_s}\right)\right), \; k = 1, 2, ..., N \tag{2.24}$$
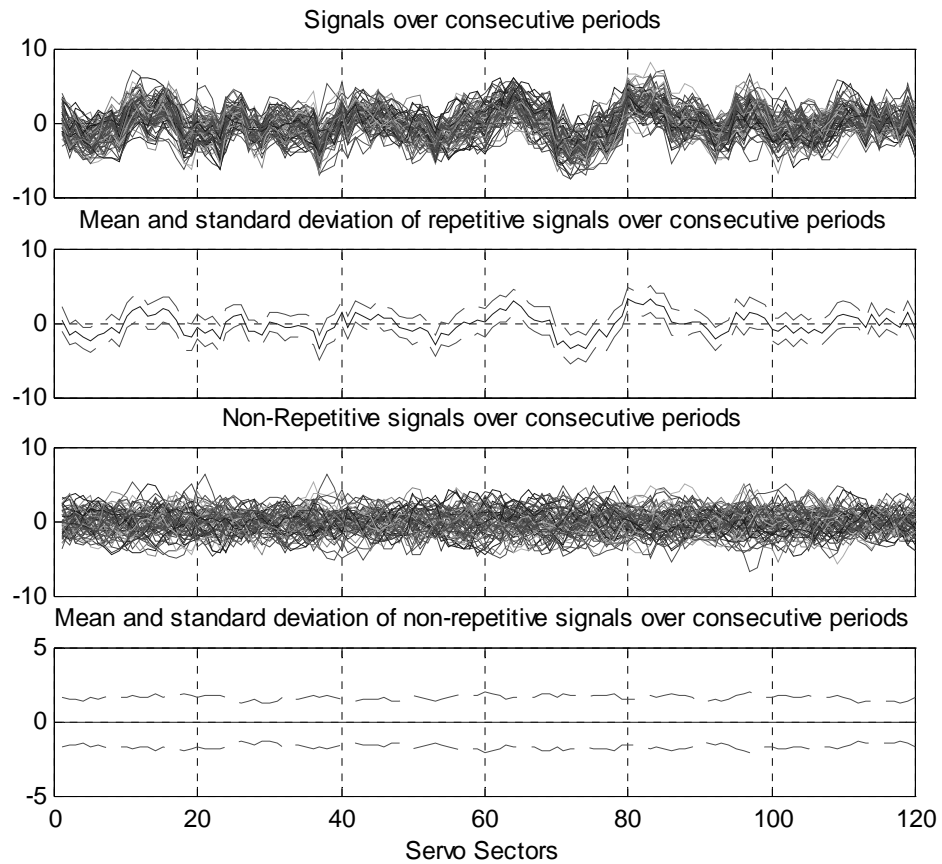
Figure 2.19: Decouple PES into RPES and NRPES components. In the top plot, PES are superposed in the track following mode. PES over consecutive disk revolutions are shown and exhibit a strong repetitive patten. This patten, or RPES, can be extracted by taking the mean value of PES over sector numbers, shown in the second plot. NRPES are extracted and shown in the third plot.
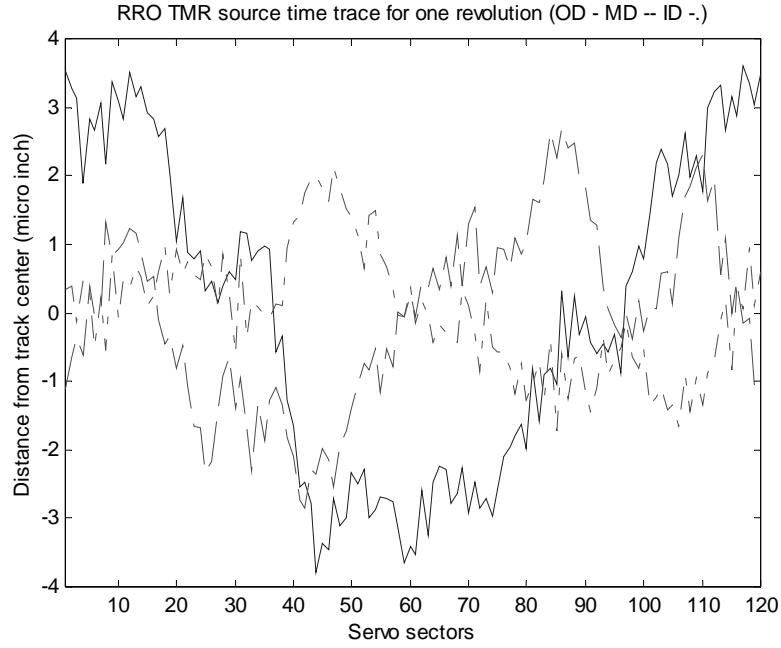
Figure 2.20: Typical servo writren-in time trace at three locations (OD MD ID)

The servo written-in errors can then be obtained by filtering RPES through the inverse of the sensitivity function, described as:

$$r_r(k) = S^{-1}\left(z^{-1}\right) y_r(k), \, k = 1, 2, .., N \tag{2.25}$$

where $r_r(k)$ is the RRO TMR source at each sector k as shown in Fig. 2.20. If $S\left(z^{-1}\right)$ contains unstable zeros outside the unit circle and direct inverse causes unstable system, Zero Phase Error inverse discussed in Chapter 3 can be used.

NRPES $y_{nr}(k)$ is obtained by removing $y_r(k)$ from PES $y(k)$, as follows:

$$y_{nr}(k) = y(k) - y_r(k), \, k = 1, 2, ..., N \tag{2.26}$$

$y_{nr}(k)$ is shown in the third plot in Fig. 2.19. Also shown in its last plot are the mean of
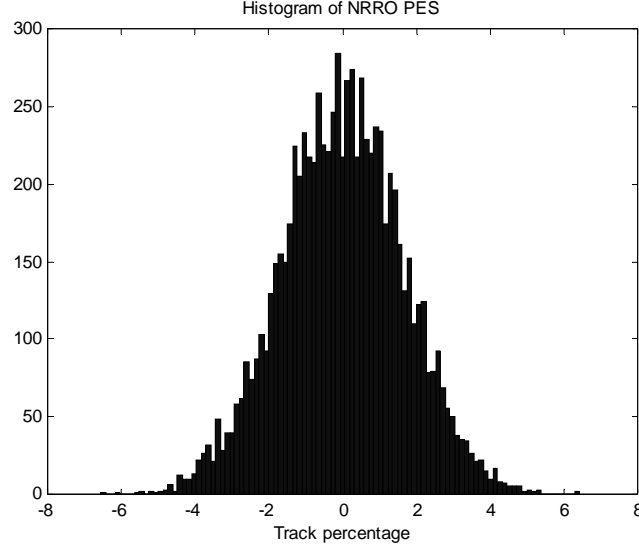
Figure 2.21: NRPES Histogram.

$y_{nr}(k)$ at each sector and its standard deviations. The histogram of $y_{nr}(k)$ is shown in Fig. 2.21.

NRPES $y_{nr}(k)$ is modeled as a zero-mean and Gaussian-distributed random process. Its variance R_y can be obtained by

$$R_{y_{nr}} = \frac{\sum_{k=1}^{N} [y_{nr}(k) - y_{mean}]^2}{N} \tag{2.27}$$

where $y_{mean} = E[y_{nr}(k)]$. Usually, y_{mean} should be small enough to avoid off-track bias in the track following mode. Standard deviation of $y_{nr}(k)$ is defined as $\sigma_{y_{nr}} = \sqrt{R_{y_{nr}}}$. Three sigma value of the PES $y(k)$, $3\sigma_y$, is a standard to evaluate TMR performance. The variance relationship between PES, RPES, and NRPES is given by:

$$R_y = R_{y_{nr}} + R_{y_r} \tag{2.28}$$

where

$$R_y = \sigma_y^2$$

$$R_{y_r} = \sigma_{y_r}^2$$

$$R_{y_{nr}} = \sigma_{y_{nr}}^2$$

In terms of standard deviation:

$$\sigma_y = \sqrt{\sigma_{y_r}^2 + \sigma_{y_{nr}}^2} \tag{2.29}$$

Frequency-Domain Analysis

Power spectrum of NRPES $y_{nr}(k)$ shows that it is a colored random process. Figure 2.9 shows the how torque disturbances $d(k)$, mechanical disturbances $m(k)$, and sensor noise $n(k)$ affect NRPES in the track following mode. To characterize these TMR sources, the frequency-domain contents of $y_{nr}(k)$ are first examined.

This dissertation uses discrete-time Fourier transform (DFT) to analyze signals in frequency-domain. In DFT, the signals are represented as a superposition of complex sinusoids. The representation is intuitive for analyzing signals filtered through linear systems. A linear system shapes amplitude and phase of signals passing it through, by its frequency responses.

Collected PES $y(k)$ is always a discrete sequence with a finite duration. Since it is absolutely summable, it can be represented by a Fourier integral of the form

$$y(k) = \frac{1}{2\pi} \int_{-\pi}^{\pi} \bar{Y}(e^{j\omega}) e^{j\omega k} d\omega \tag{2.30}$$

where $\bar{Y}(e^{j\omega})$ is the Fourier transform of $y(k)$

$$\bar{Y}(e^{j\omega}) = \sum_{k=-\infty}^{\infty} y(k) e^{-j\omega k} \tag{2.31}$$

Equations 2.30 and 2.31 form a Fourier representation for $y(k)$. The PES is represented by a superposition of infinitesimally small complex sinusoids of the form:

$$\frac{1}{2\pi} \bar{Y}(e^{j\omega}) e^{j\omega k} d\omega \tag{2.32}$$

Equation 2.31 determines the frequency components of $y(k)$ from $-\pi$ to π, as shown in Eq. 2.30.

Since $y(k)$ is a finite-duration sequence, discrete Fourier transform (DFT) can be used to analyze its frequency components. DFT of a sequence can be regarded as a sampled Fourier transform of the sequence. The DFT $\bar{F}_y(k)$ of a causal sequence $y(n)$ is given as

$$\bar{F}_y(k) = \sum_{n=1}^{N} y(n) e^{\frac{-j2\pi(k-1)(n-1)}{N}}, \ \ k = 1, 2, ..., N \tag{2.33}$$

where N is the length of $y(n)$. $\bar{F}_y(k)$ is a complex number sequence of length N, and represents sinusoids with magnitude $\left| \bar{F}_y(k) \right|$ at frequency $\frac{k-1}{N} F_s$, where F_s is the sampling frequency. Note that $\bar{F}_y(k)$ has a periodicity N, $y(n)$ can be represented by the inverse DFT as

$$y(n) = \frac{1}{N} \sum_{k=1}^{N} \bar{F}_y(k) e^{\frac{j2\pi(k-1)(n-1)}{N}} \tag{2.34}$$

For real signals $y(n)$, $\bar{F}_y(k)$ has a real and symmetric magnitude $F_y(k)$ and anti-symmetric phase. Thus, only the first half of $\bar{F}_y(k)$ needs to be kept. The normalized DFT $\bar{F}_{yn}(k)$ is given by

$$\bar{F}_{yn}(k) = \frac{2\bar{F}_y(k)}{N} \tag{2.35}$$

where $k = 1, 2, ..., M$. When N is even, $M = \frac{N}{2} + 1$, otherwise, $M = \frac{N+1}{2}$. From Eqs. 2.33 and 2.35, it can be derived that

$$\bar{F}_{yn}(1) = \frac{1}{N} \sum_{k=1}^{N} y(n)$$

which is just the mean of $y(n)$. Further investigations show that the magnitude of $\bar{F}_{yn}(k)$, denoted as $F_{yn}(k)$, reflects the real magnitude of complex sinusoids at frequency $\frac{k-1}{N} F_s$. To simplify the description in the rest of the dissertation, DFT refers to the normalized DFT if not otherwise stated.

By definition, assuming $y(n)$ has a zero mean, its variance is given as

$$R_y = \frac{\sum_{n=1}^{N} y^2(n)}{N} \tag{2.36}$$

According to the Parseval's relation,

$$\frac{\sum_{n=1}^{N} y^2(n)}{N} = \frac{\sum_{k=1}^{N} S(k)}{N} \tag{2.37}$$

where $S(k)$ is the power spectrum density (PSD) of $y(n)$. PSD can be estimated using Welch's method[59]. The method uses the magnitude of the DFT, given by:

$$S(k) = \frac{F_y(k)^2}{N}, \ k = 1, 2, ..., N$$

In general, N is a very large number, and M can be approximated by $\frac{N}{2}$. Thus,

$$\begin{aligned}
\sum_{k=1}^{N} F_y(k)^2 &= 2 \sum_{k=1}^{M} \left(\frac{F_{yn}(k) N}{2} \right)^2 \\
&= \frac{N^2}{2} \sum_{k=1}^{M} F_{yn}^2(k) \tag{2.38}
\end{aligned}$$

From Eq. 2.37, the variance of $y\left(n\right)$ can be expressed as

$$
\begin{aligned}
R_y &= \frac{\sum_{k=1}^{N} \frac{F_y^2(k)}{N}}{N} \\
&= \frac{\sum_{k=1}^{N} F_y^2\left(k\right)}{N^2} \\
&= \frac{1}{2}\sum_{k=1}^{M} F_{yn}^2\left(k\right)
\end{aligned}
\tag{2.39}
$$

Standard deviation σ_y of $y\left(k\right)$ can then be obtained from the normalized DFT $F_{yn}\left(k\right)$:

$$
\sigma_y = \sqrt{\frac{\sum_{k=1}^{M} F_{yn}^2\left(k\right)}{2}}
\tag{2.40}
$$

Figures 2.22 and 2.23 show the normalized DFT magnitude of RPES and NRPES, and their average by root-mean-square (RMS). The average is used to reduce the estimation errors.
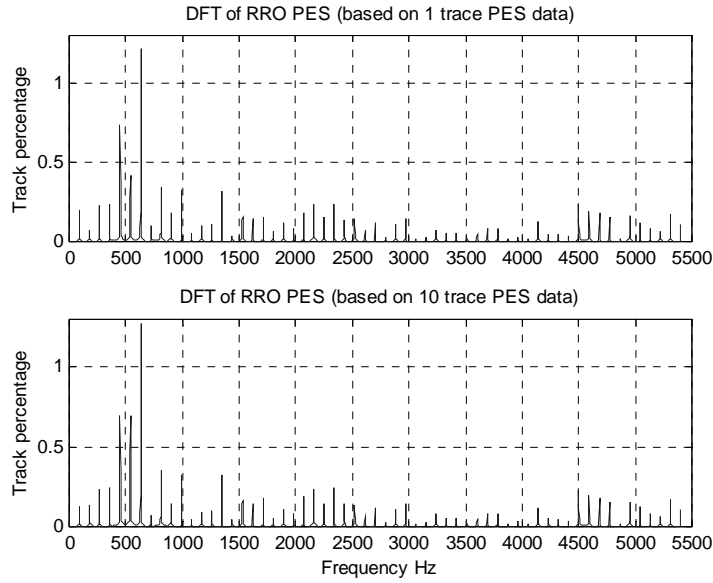
Figure 2.22: DFT magnitude of RPES
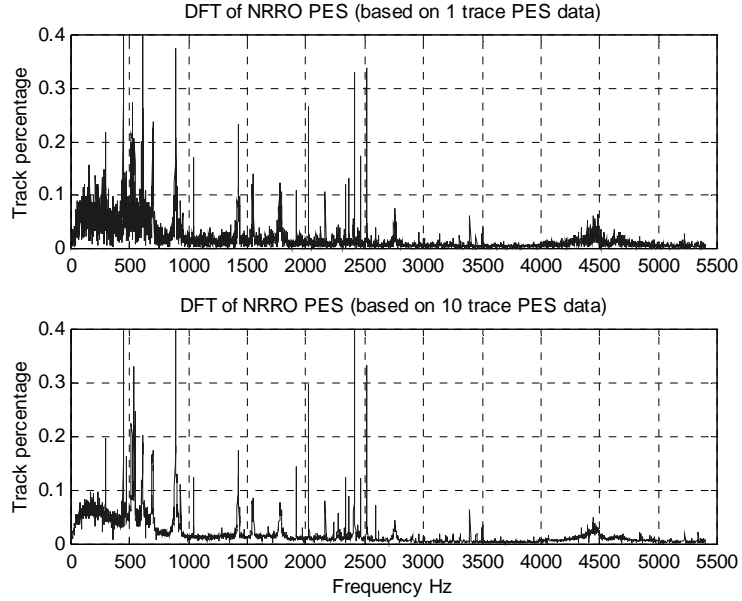
Figure 2.23: DFT magnitude of NRPES. The RMS average results in smaller estimation variances, and smoother mangnitude plots.

It can be approximated that the M-point DFT magnitude of a white noise sequence is a constant when M is large, i.e., $F_{yn}(k) = c, \forall\ k$. c relates to the standard deviation σ of the white noise:

$$\sigma\ =\ \sqrt{\frac{\sum_{k=1}^{M} F_{yn}(k)^2}{2}} = \sqrt{\frac{Mc^2}{2}} = \sqrt{\frac{M}{2}}c \qquad (2.41)$$

$$c\ =\ \sqrt{\frac{2}{M}}\sigma \qquad (2.42)$$

For a discrete-time linear system with frequency response $H\left(e^{-j\omega}\right)$,

$$\bar{F}_{y_o}(k) = H\left(e^{-j\frac{(k-1)}{M}\frac{\omega_s}{2}}\right)\bar{F}_{y_i}(k),\ k = 1, 2, 3, ..., M \qquad (2.43)$$

where $\frac{\omega_s}{2}$ is its Nyquist frequency. $\bar{F}_{y_i}(k)$ and $\bar{F}_{y_o}(k)$ are the M-point DFT of the input

and the output signals, repetitively, with their magnitude related by

$$F_{y_o}(k) = \left| H\left(e^{-j\frac{(k-1)}{M}\frac{\omega_s}{2}}\right)\right| F_{y_i}(k), \ k = 1, 2, 3, ..., M \tag{2.44}$$

Given the DFT of the output signals, the DFT magnitude of the input can be obtained by

$$F_{y_i}(k) = \left| H\left(e^{-j\frac{(k-1)}{M}\frac{\omega_s}{2}}\right)\right|^{-1} F_{y_o}(k), \ k = 1, 2, 3, ..., M \tag{2.45}$$

2.3.2 Sensor Noise

This section discusses the frequency characteristics of the sensor noise and methods to characterize it from the PES.

Sensor noise $n(k)$ affects PES through the sensitivity function $S\left(z^{-1}\right)$, as shown in Fig. 2.9. It is speculated that the high-frequency contents of the PES are mainly contributed by sensor noise and disk modes. The transfer function from them to the measured PES $y(k)$, $S\left(z^{-1}\right)$, as shown in Fig. 2.16, exhibits a unit gain near the Nyquist frequency of the servo system. The torque disturbances $w(k)$ affect PES through the disturbance transfer function $T\left(z^{-1}\right)$. As shown in Fig. 2.15, $T\left(z^{-1}\right)$ rolls off at high frequencies. The effects of the torque disturbances on the PES are therefore negligible near the Nyquist frequency.

Two experiments have been carried out to investigate the high-frequency spectrum of the PES. The first experiment is a vacuum chamber test to verify that the sensor noise is the major contributor to the high-frequency contents of the PES. The second one analyzes burst readings and proves that the sensor noise come from the burst demodulation, and is indeed white noise.

In the first experiment, a drive is placed inside a vacuum chamber, and the PES are

collected under different air pressures at OD, MD, and ID. Their DFT magnitude near the Nyquist frequency represents the signal power at the high frequency, and is shown in Fig. 2.24. The signal power comes from two possible sources: sensor noise and disk modes. The sensor noise from media and electronics is not affected by the air pressures. The disk modes excited by air turbulence, however, should decrease with the air pressures. In addition, if the disk modes were major contributors, the high-frequency PES signal power should have noticeable difference at ID, MD and OD.

Figure 2.24 shows that the high-frequency signal power has neither an obvious decreasing trend with the air pressures, nor significant difference at ID, MD, and OD. The results demonstrate that the disk modes have little effects on the high-frequency PES, which is dominated by the sensor noise.

The second experiment is carried out to identify the source of the sensor noise, and to examine their frequency characteristics. In the experiment, A- and B-burst readings are first collected simultaneously during track following. After that, the repeatable components caused by the burst defects and servo written-in offsets are removed from the readings. The remained non-repeatable components of A- and B-burst are then summed with and subtracted from each other, with the DFT magnitude of the results shown in Fig. 2.25.

Recall that in Eq. 1.1, PES is obtained from the burst readings at each servo sector by

$$y = K_{burst} \left(v_a - v_b \right) \tag{2.46}$$

where K_{burst} is a constant gain. Sensor noise contaminate the burst readings v_a and v_b as
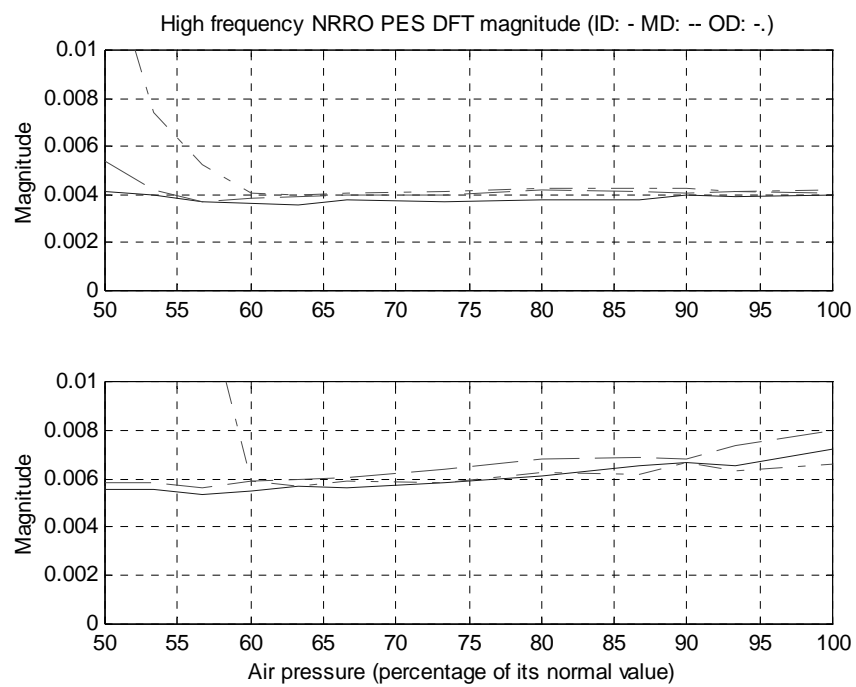
Figure 2.24: High-frequency floor of NRPES DFT magnitude v.s. air pressure in the disk drive at ID, MD, and OD for one head. Difference among them are small, implying that the disk modes have negligible effects on the floor.

follows:

$$v_a = v_{an} + n_a \tag{2.47}$$

$$v_b = v_{bn} + n_b \tag{2.48}$$

where v_{an} and v_{bn} are the true burst readings, and n_a and n_b are modeled as zero mean, independent, Gaussian distributed white noise. As a result,

$$
\begin{aligned}
y &= K_{burst}\left(v_a - v_b\right) \\
&= K_{burst}\left(v_{an} - v_{bn}\right) + K_{burst}\left(n_a - n_b\right)
\end{aligned}
\tag{2.49}
$$

Note that $v_{an} + v_{bn}$ is a constant C,

$$K_{burst}\left(v_a + v_b\right) = K_{burst}C + K_{burst}\left(n_a + n_b\right) \tag{2.50}$$

(2.49) and (2.50) are key to the conclusions of the burst test experiment. $K_{burst}v_a$ and $K_{burst}v_b$ can be obtained simultaneously at each servo sector. $K_{burst}\left(v_a - v_b\right)$ is used to construct PES, while $K_{burst}\left(n_a + n_b\right)$ is a constant plus the PES noise. Because the variance of $\left(n_a - n_b\right)$ and $\left(n_a + n_b\right)$ are the same. The DFT of $K_{burst}\left(n_a + n_b\right)$ and that of $K_{burst}\left(n_a - n_b\right)$ should also have the same magnitude.

Both $K_{burst}\left(v_a - v_b\right)$ and $K_{burst}\left(v_a + v_b\right)$ contain the burst noise $K_{burst}n_a$ and $K_{burst}n_b$. The former is the PES itself, and the latter contains only the burst noise plus a constant. The previous experiment has shown that the high-frequency contents of the PES come from the sensor noise. Comparison of the DFT magnitude the PES and the burst noise is shown in Fig. 2.25. It can be seen that the two indeed have the same magnitude near the Nyquist frequency of the servo system. The burst noise dominates the high-frequency
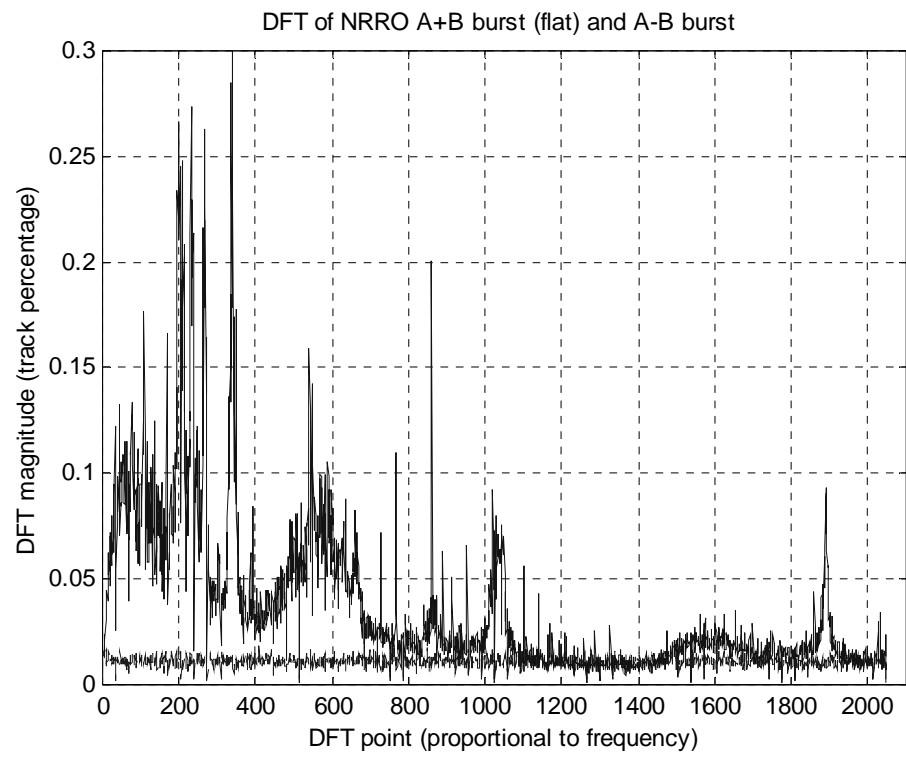
Figure 2.25: The DFT magnitude of $K_{burst}\left(v_a - v_b\right)$ and $K_{burst}\left(v_a + v_b\right)$
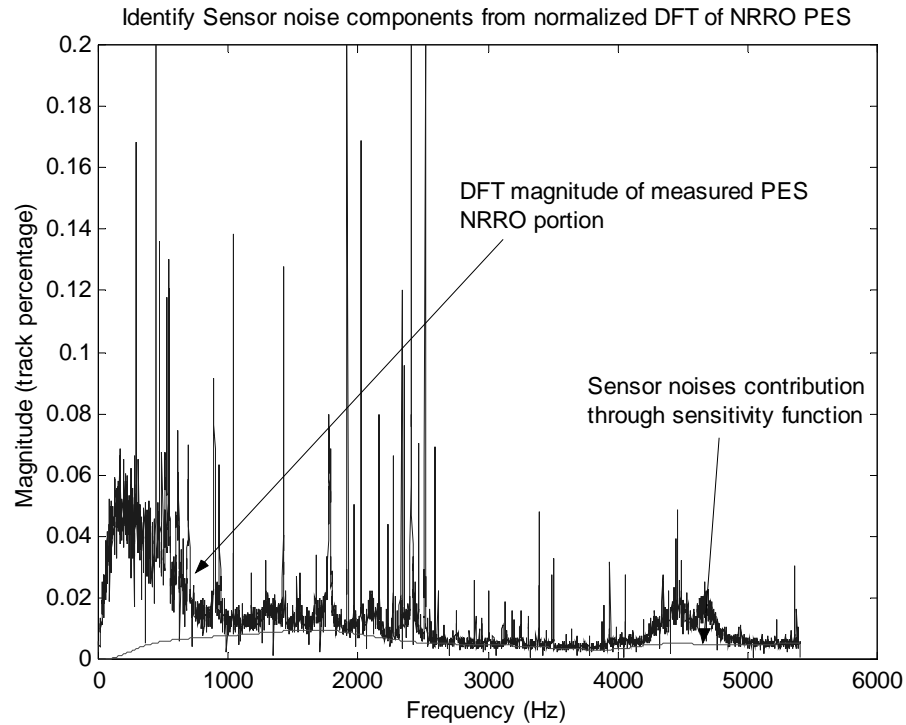
Figure 2.26: Identification of the sensor noise from PES and the sensitivity function.

contents of the PES, and therefore is the primary source of the sensor noise. The burst noise also exhibits a flat frequency magnitude in all frequency, proving that the sensor noise is indeed white.

Both the vacuum chamber and the burst test experiments support the following conclusions:

1. The high-frequency contents of PES are dominated by sensor noise;

2. The sensor noise is mainly caused by the burst demodulation noise;

3. Sensor noise is white.

Based on the conclusions, the sensor noise can be obtained by examining the high-frequency contents of PES. Because the PES are easy to collect, simple but practical procedures to identify the sensor noise can be established as follows:

1. Collect raw PES;

2. Identify RPES using Eq. 2.23, and obtain NRPES using Eq. 2.26;

3. Repeat procedure 1 and 2 several times and calculate the fixed-point DFT of each NRPES trace;

4. Smooth the DFT magnitude plot by the RMS average;

5. Determine the high-frequency DFT magnitude c;

6. Use c and Eq. 2.41 to calculate the standard deviation σ of the sensor noise.

The procedures to identify the contributions of the sensor noise to the PES are illustrated in Fig. 2.26. The DFT magnitude c of the sensor noise is first determined as described before. Based on (2.43) and (2.44), the DFT of its contribution to the PES is

$$\bar{F}_{y_{sn}}(k) = S\left(e^{-j\frac{(k-1)}{M}\frac{\omega_s}{2}}\right) c, \, k = 1, 2, 3, ..., M \tag{2.51}$$

where M is the DFT point, and $S\left(e^{j\omega}\right)$ is the sensitivity function with a Nyquist frequency $\frac{\omega_s}{2}$. The standard deviation of the sensor noise contributions to the PES can be calculated using (2.40), and is given as follows:

$$
\begin{aligned}
F_{y_{sn}}(k) &= \left|\bar{F}_{y_{sn}}(k)\right|, \, \forall k \tag{2.52} \\
\sigma_{y_{sn}} &= \sqrt{\frac{\sum_{k=1}^{M} F_{y_{sn}}^2(k)}{2}} \tag{2.53}
\end{aligned}
$$

2.3.3   Torque Disturbance

This section uses an experiment to investigate the frequency characteristics of the torque disturbance in the track following mode, shown as $d(k)$ in Fig. 2.9. Using the PES, the procedures to identify the torque disturbances are also presented.

To isolate the effect of torque disturbances from other noise sources, the servo controller loop is opened and the position of the floating arm is measured using a laser Doppler velorometer (LDV). Because there is no control input, the torque applied to the floating arm comes only from the air turbulence and the pivot friction.

The experiment is carried out as follows:

1. Spin the drive at its nominal RPM, then unlatch the actuator arm;

2. Use the LDV to measure the position of the floating arm at the R/W head. This measures the effect of the torque disturbances via the torque transfer function.

3. Latch the actuator arm to the magnetic stopper at ID;

4. Use the LDV to measure the head position again. This records the measurement noise.

The DFT magnitude of the two position measurement are shown in Fig. 2.27. The DFT of the position of the floating arm shows a characteristics of a rigid body with a pivot friction resonance at $50Hz$. The LDV measurement noise contaminated the position measurement above $500\ Hz$. Also shown in Fig. 2.27 is the DFT magnitude of the response to white noise of the nominal plant. It is adjusted to match that of the measured position. The matching is very good below $500\ Hz$. At higher frequencies, the LDV measurement

noise and the position measurement are not distinguishable. From this experiment, it can

be concluded that the torque disturbances can be modeled as white noise at least up to

500 Hz, aside from the deterministic constant torque bias caused by the air turbulence and

flexible print circuit. Although the behavior of the torque disturbances at high frequencies

can not be drawn from the experiment, it is assumed white at all frequencies.
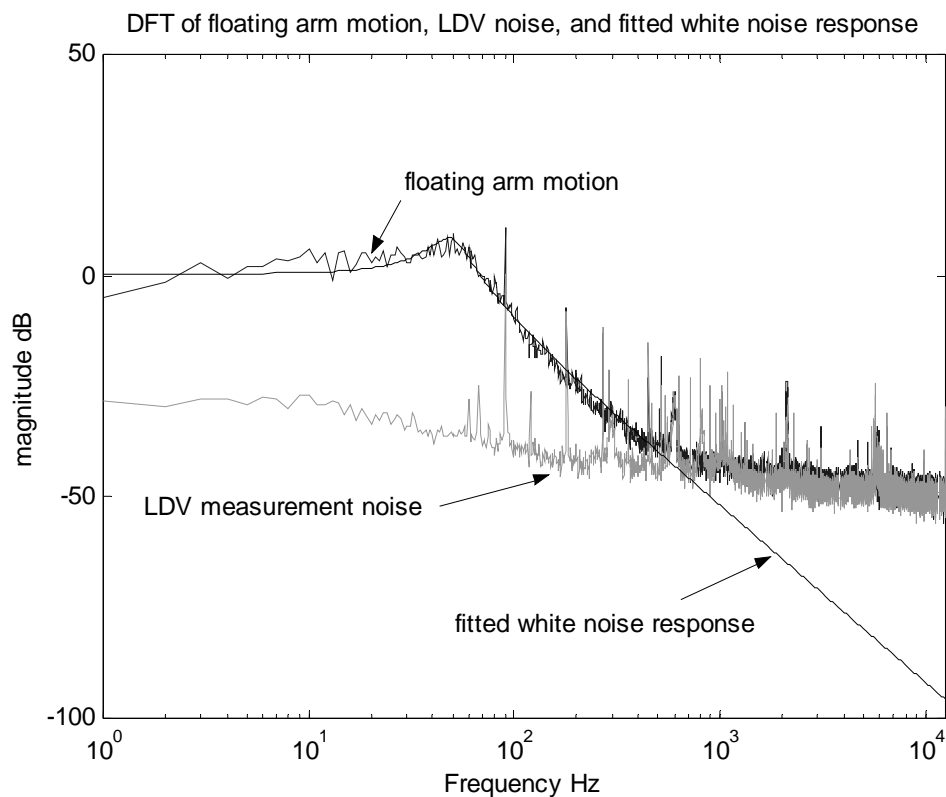
Figure 2.27: DFT of the position signal from a floating arm. Also shown are the system measurement noise, and curve-fitted response using simple plant model with pivot friction. This justified modeling torque disturbance as white.

NRPES has three major sources: sensor noise, torque disturbance, and disk mods. In order to identify the torque disturbances through NRPES, the effects of the other two sources on NRPES need to be removed. This is carried out in frequency-domain by two
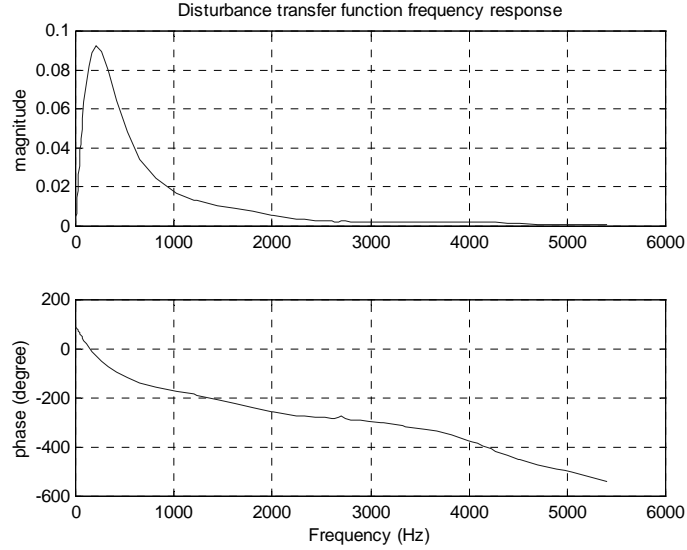
Figure 2.28: Disturbance transfer function frequency response with frequency and magnitude in linear scale.

steps. The first step is to obtain the DFT magnitude of the NRPES without sensor noise contribution by

$$F_{y_{md}}(k) = \sqrt{F_{y_{nr}}^2(k) - F_{y_{sn}}^2(k)}, \ \forall k \qquad (2.54)$$

where $F_{y_{nr}}(k)$ is the DFT magnitude of NRPES, $F_{y_{sn}}(k)$ is the sensor noise floor given in (2.52), and k is the DFT point.

The second step is to remove the effect of disk modes on the NRPES. It will be shown in the next section that disk modes are periodic in time-domain and therefore spikes in the DFT magnitude plot. With the spikes removed, Figure 2.29 shows that the base-line of $F_{y_{md}}(k)$ has the same shape of the disturbance transfer function, as illustrated in 2.28. In Figure 2.29, the torque transfer function magnitude is adjusted to match $F_{y_{md}}(k)$. The matching of the shapes validates the white noise model of the torque disturbances.
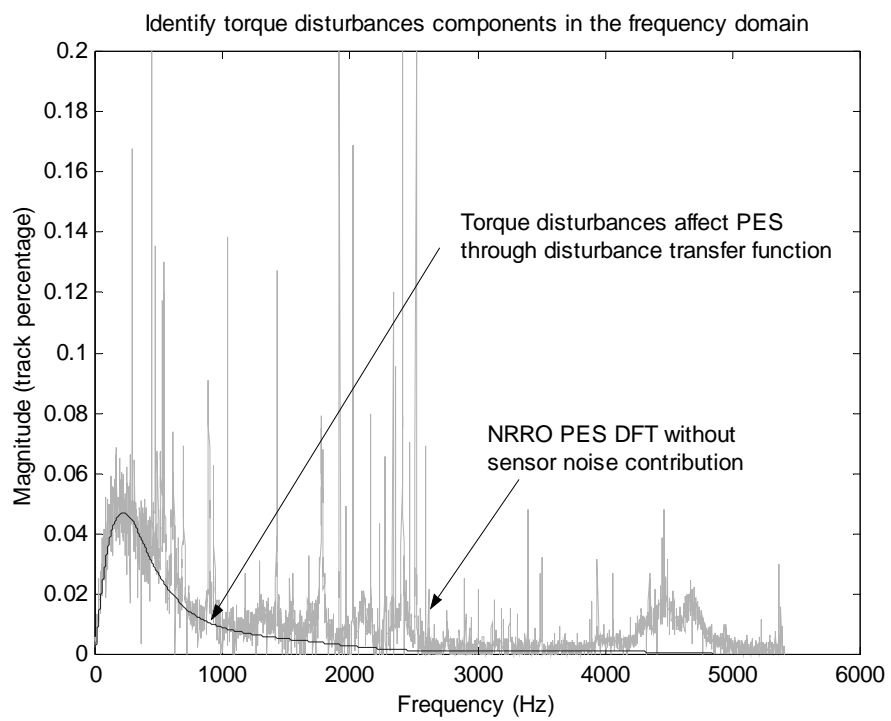
Figure 2.29: Identification of torque disturbance from PES and the disturbance transfer function.

The procedure to determine the standard deviation of the torque disturbance is as follows:

1. Use the procedure described in Section 2.3.2 to determine $F_{y_{sn}}(k)$, the sensor noise contributions to NRPES;

2. Remove the sensor noise contribution from $F_{y_{nr}}(k)$ using Eq. 2.54;

3. Smooth $F_{y_{md}}(k)$ and obtain its base-line;

4. Adjust the magnitude of the disturbance transfer function to match the base-line of $F_{y_{md}}(k)$. The resulted curve, $F_{y_d}(k)$, is the approximation of the DFT magnitude of the NRPES solely contributed by the white torque disturbance. Its standard deviation can be calculated using Eq. 2.40.

5. The gain used to adjust the disturbance transfer function is the constant DFT magnitude of the white torque disturbance. Its standard deviation can also be obtained using Eq. 2.40.

2.3.4   Disk Modes and other TMR Sources

Disk resonance modes are excited primarily by the air turbulence within HDDs. The behavior is dominated by the disk's material and geometry. 3.5 *inch* diameter disks with 0.8 *mm* thickness, as shown in Fig. 1.3, are current industry standard for desktop HDDs. The disk modes degrade the PES significantly, and are increasingly serious with higher rotation speed and the TPI. [44]

Each disk vibration mode has m nodal circles and n nodal diameters [35], and

is denoted as the (m, n) mode. $(0, 0)$, $(0, 1)$, $(0, 2)$ and $(0, 3)$ modes and their natural frequencies are illustrated in Figs. 2.30, 2.31, 2.32, and 2.33, respectively.
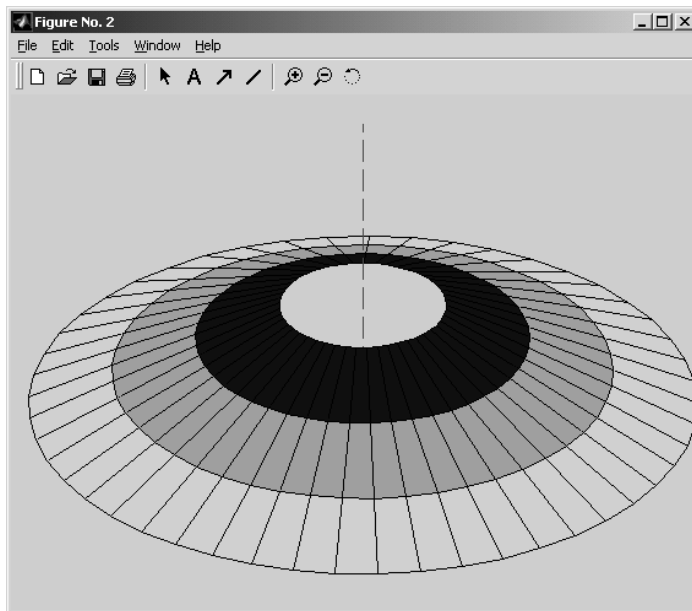
Figure 2.30: $(0, 0)$ disk mode at 608 Hz

Disk modes consists of all possible (m, n) modes. However, the above four modes are the most significant TMR contributors. Superposition of these modes is shown in Fig. 2.34 to illustrate the disk vibrations. As the disk rotates, the vibrations generate periodic traveling waves. The R/W head on the disk then encounters periodic displacement shift of the fixed tracks on the disk. The effect is reflected in the DFT of the PES as the spikes shown in Fig. 2.35.

The procedure to determine disk modes and other unaccounted-for TMR sources is as follows:

1. Follow the procedures in Sections 2.3.2 and 2.3.3 to obtain $F_{y_{nr}}(k)$, $F_{y_{sn}}(k)$ and
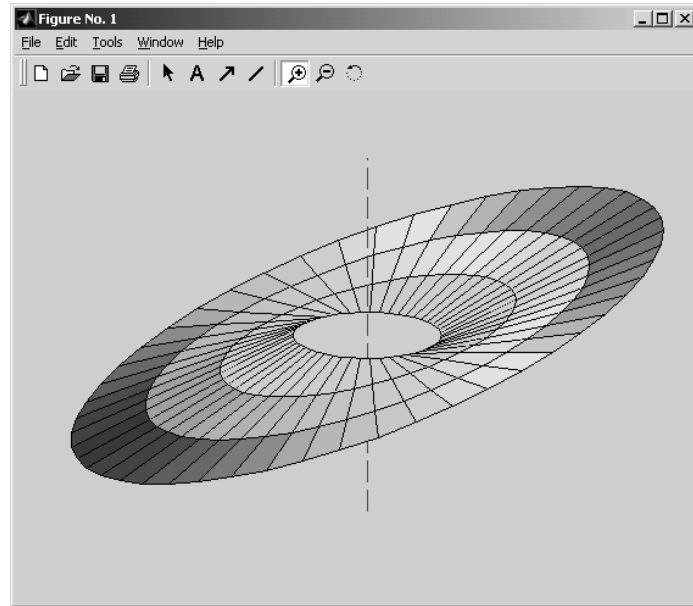
Figure 2.31: $(0,1)$ disk mode at 619 Hz.
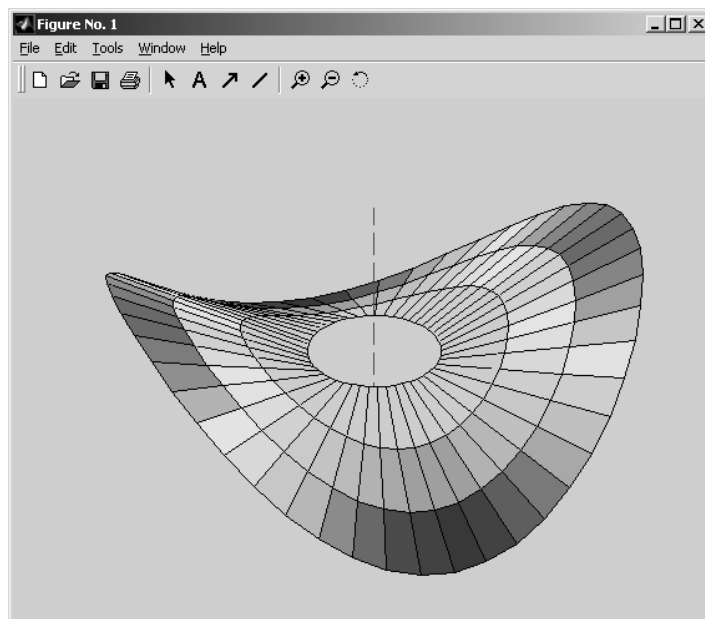
Figure 2.32: $(0,2)$ disk mode at 729 Hz
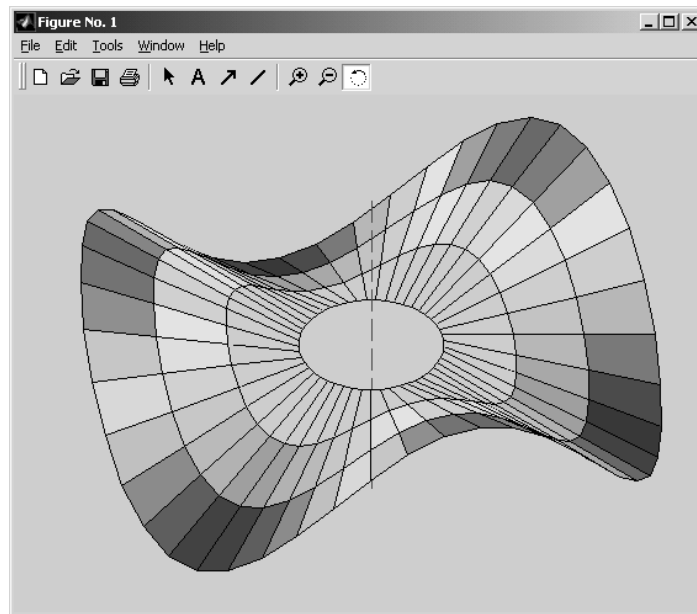
Figure 2.33: $(0,3)$ disk mode at 1168 Hz
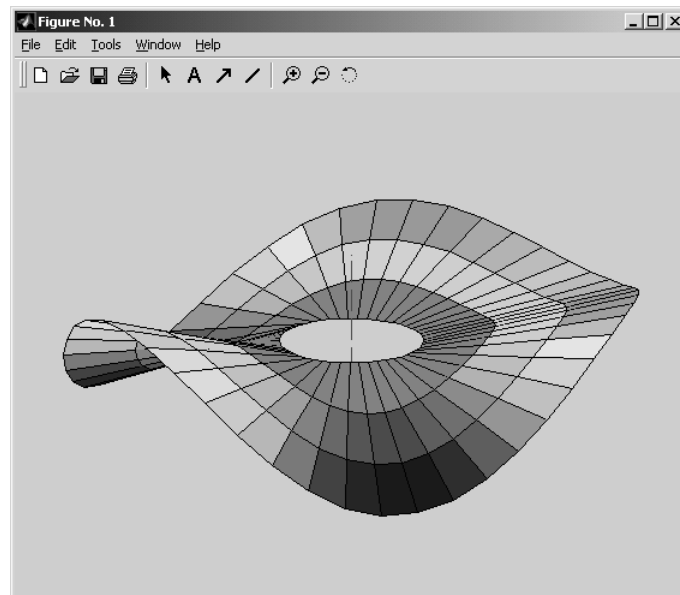
Figure 2.34: Superposition of PES from four contributing disk modes. This is an exaggerated illustration for disk vibration.

$F_{y_d}(k)$;

2. The effects of the disk modes and all other unaccounted-for TMR sources are obtained by removing the sensor noise and torque disturbance floor from the NRPES DFT magnitude, described as:

$$F_{y_m}(k) = \sqrt{F_{y_{nr}}^2(k) - F_{y_{sn}}^2(k) - F_{y_d}^2(k)}, \ \forall k \tag{2.55}$$

Following the procedure, $F_{y_m}(k)$ of the example PES is shown in Fig. 2.35.
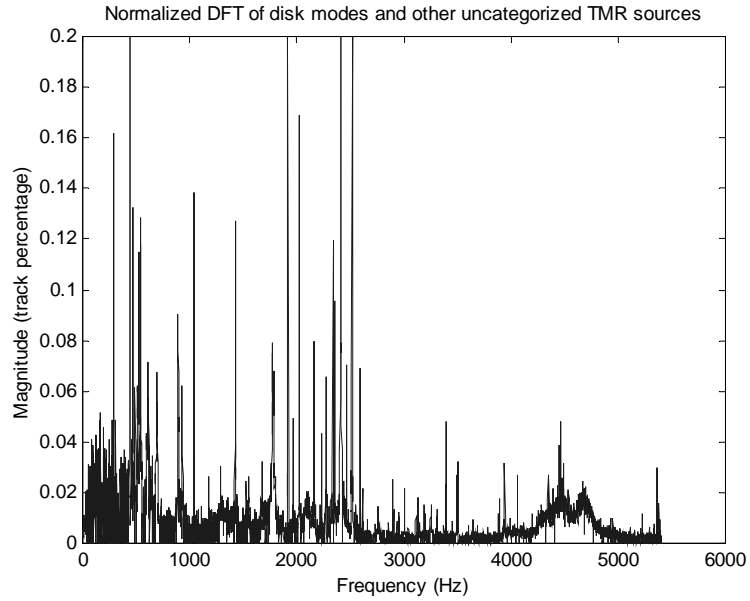
Figure 2.35: DFT of disk modes. Sensor noise and torque disturbance are removed.

The DFT magnitude of the disk modes can be generated by

$$F_m(k) = S^{-1}(k) F_{y_m}(k) \tag{2.56}$$

$F_m(k)$ for OD, MD, and ID are shown in Fig. 2.36. It can be seen that the energy of the disk modes is concentrated below 500 Hz. This is why the error rejection function

must have strong attenuations of low-frequency disturbances. Time-domain trace of the disk modes can be obtained by the inverse DFT, and the results are plotted in Fig. 2.37.
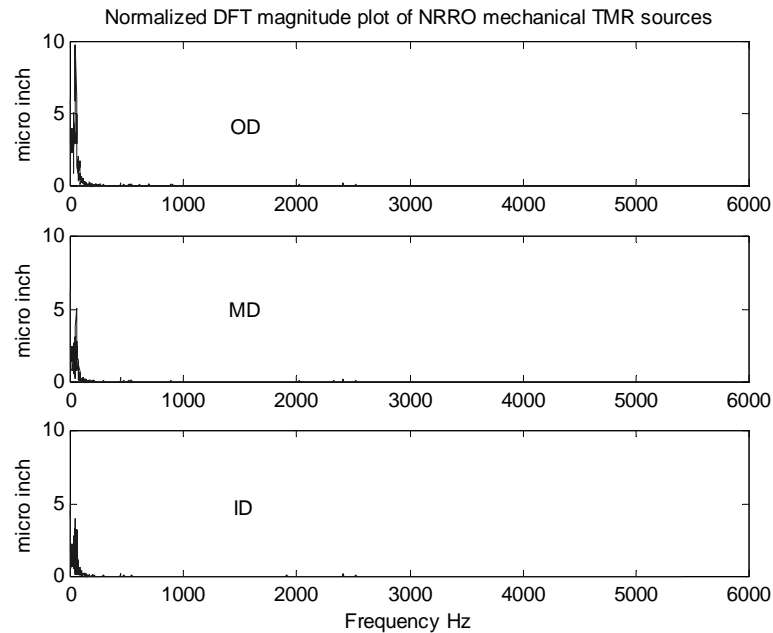
Figure 2.36: DFT of the disk modes and other unaccounted-for TMR sources. They are concentrated below 500 Hz.

2.4   Summary

Servo design specifications were defined at the beginning of this chapter. HDD servo system and TMR modeling were introduced. The TMR sources are categorized into repeatable servo written-in errors, and non-repeatable sensor noise, torque disturbance, and disk modes. Each of the four components was analyzed and characterized theoretically and experimentally. Based on the results, practical procedures were developed to identify them using only the raw PES.
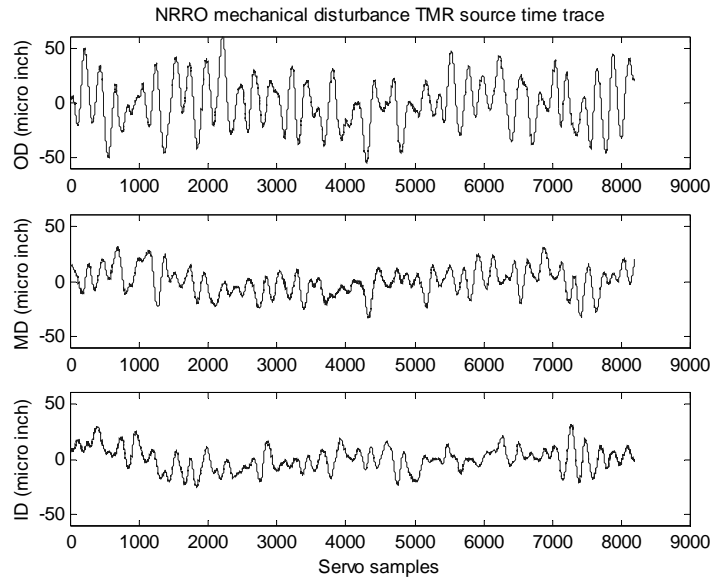
Figure 2.37: Time domain trace of the disk modes. OD has the largest variance while ID has the smallest one.

The techniques to process PES in time- and frequency-domains were explained. In the frequency-domain, the normalized DFT is used because its magnitude has the same unit as the PES. The PES variance can also be calculated from it by Parseval's relation.

The three components of NRPES were investigated by experiments. A simple method was developed to model the TMR sources using the raw PES. The method is validated by comparing the measured PES and the simulated PES, shown in Figs. 2.38 and 2.39, respectively. The latter is the PES output of the servo system with the modeled TMR sources as inputs. There is only 1% difference in their variance caused by the estimation errors of the noise base-line and the phase for the inverse DFT.

Noise contributions (variance) in the measured PES

RRO PES: 43%

NRRO PES: 57%

RRO PES
NRRO PES
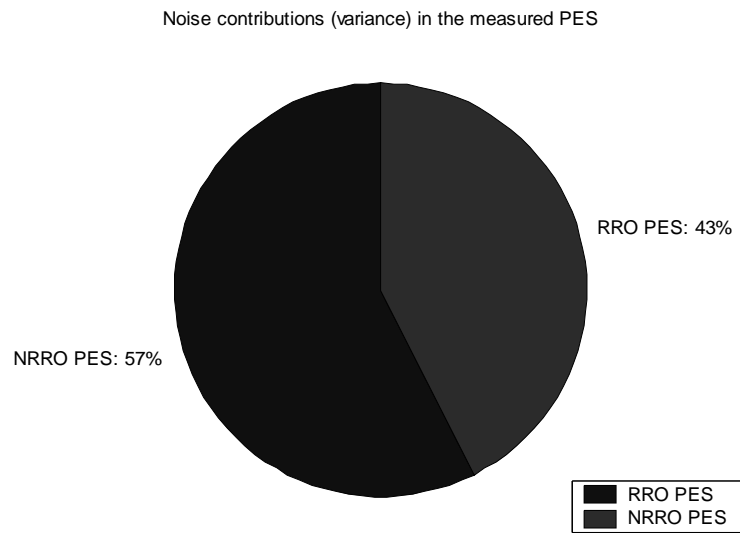
Figure 2.38: Pie chart showing NRPES and RPES components in the measured PES.

Noise contributions (variance) in re-constructed PES using indentified TMR sources

Sensor noise: 1%

Torque disturbance 11%

RRO: 44%

Disk modes and other TMR sources: 44%

sensor noise
torque disturbance
disk modes and others
servo written-in errors
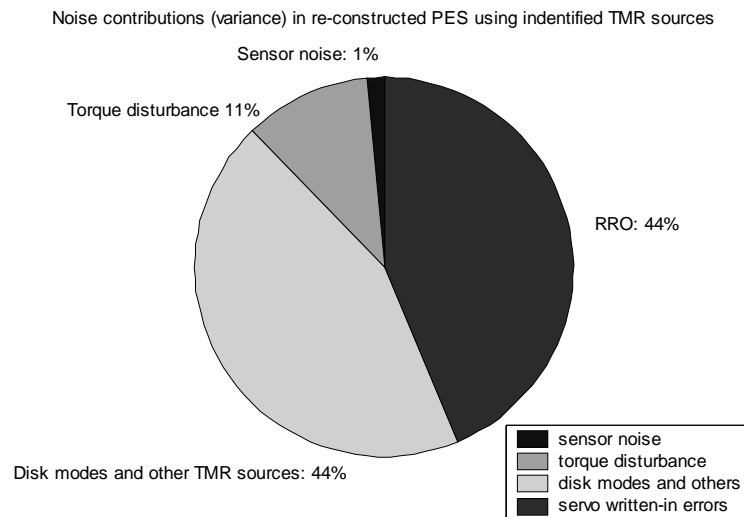
Figure 2.39: Pie chart showing contributions of TMR sources in the simulated PES using the TMR models.

Chapter 3

Two Degree of Freedom Control System

This Chapter introduces the two degree of freedom (2DOF) control for HDD. In Section 3.1, the conventional mode switching control is first introduced, followed by the description of the 2DOF control. As shown in Fig. 3.4, the 2DOF control structure consists of three major components: a robust feedback controller, a feedforward controller, and a reference generator. These components are described in Sections 3.2, 3.3, and 3.4, respectively. Summary of this chapter is given in Section 3.5.

3.1 Introduction

3.1.1 Conventional Mode Switching Control

The primary objective of the track following servo is to minimize the on-track PES. For track seeking, the objective is fast seek from one track center to another. It is a

common practice to design two different controllers for these two modes, and to optimize them based on the distinctive requirements. This approach is referred to as Mode Switching Control (MSC), a popular scheme used in the current HDD servo systems. It is illustrated in Fig. 3.1.
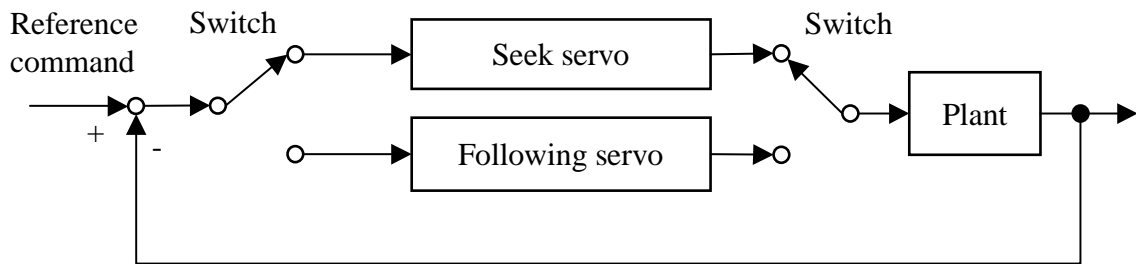
Figure 3.1: Mode switching control servo structure.

For crash protection of the R/W head in case of a power failure, there is a maximum coast velocity limit for the head. When the servo starts a long seek, the PA is first saturated and the maximum voltage is applied to the VCM. When the head velocity reaches the coast velocity with the maximum acceleration, the servo changes to the coast velocity control mode. After the velocity reaches a predefined threshold, velocity control is used to follow a predefined deceleration profile. Usually a PD controller is used for this purpose. When the head moves close to the target track center, the track following controller is used. As mentioned before, the following controller is typically a PID controller with notch filters. An extra settling mode is often added to between the seeking and the following modes. In this dissertation, the settling mode is ignored to simplify the MSC structure.

The deceleration velocity profile mentioned above is usually provided by a function

or a lookup table. The velocity changes with the remaining distance to the target track center. Time optimal servo (TOS) can be used to design the profile based on the bang-bang control theory [24]. However, the severe control input chatting associated with TOS makes its implementation for HDD impractical. In practice, proximate time optimal servo (PTOS) is used instead.

Proximate Time Optimal Servo (PTOS)

In PTOS, the velocity profile is calculated based on a rigid body plant model. By defining the velocity profile $v(p)$ as

$$v(p) = -sgn(p)\sqrt{2a|p|} - r_t \text{ if } |p| > \frac{2r_t^2}{a} \tag{3.1}$$

$$v(p) = -\frac{a}{2r_t}p \text{ if } |p| \leq \frac{2r_t^2}{a} \tag{3.2}$$

a profile function of the remaining seek distance p can be obtained [24] [51]. a, and r_t are maximum acceleration and the velocity offset, respectively. In this approach, the back $e.m.f.$ effect and the actuator bandwidth are not considered.

Improved PTOS

Improved PTOS considers the back $e.m.f.$ effects. The velocity profile for acceleration is the same as that in PTOS. The difference is in the deceleration and the settling period. The input voltage for the deceleration and the settling period is as shown in Fig. 3.2. The velocity profile is designed as follows:

1. Simulate the HDD plant model including the back $e.m.f.$ in the continuous-time domain for selected initial position and velocity combinations for deceleration;
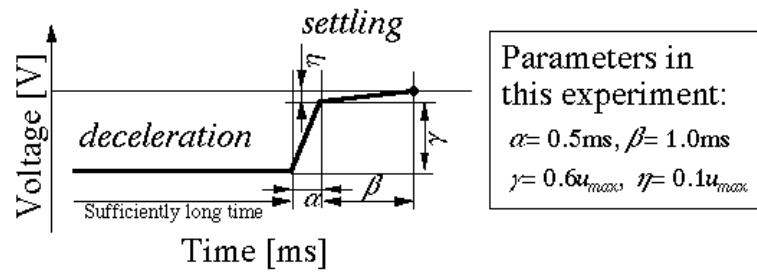
Figure 3.2: Control input voltage for velocity profile generation for the improved PTOS

2. Adjust the initial conditions (position and velocity) by iteration, repeat Step 1, and save the initial conditions from which the servo system can reach zero velocity and current simultaneously;

3. Use the initial conditions saved in Step 2, define the velocity-position relation in Fig. 3.3.

In this method, the input profile in Fig. 3.2 is determined by designer's experience.
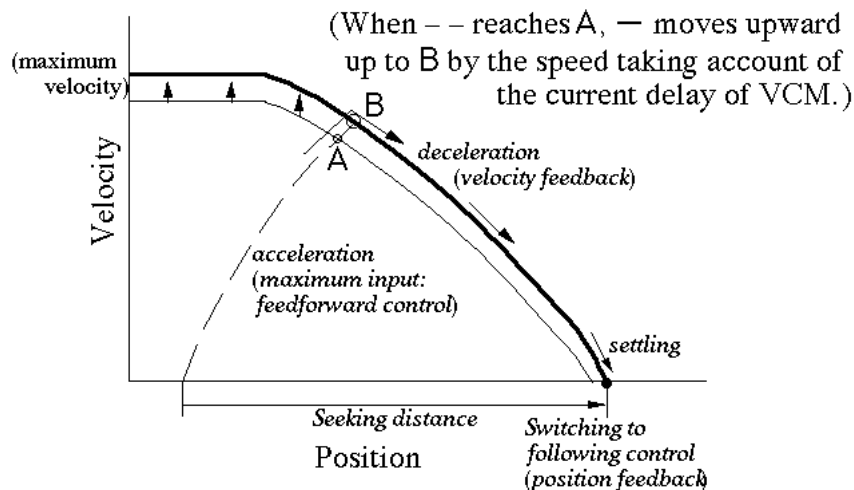
Figure 3.3: Velocity profile generation for the improved PTOS

In the improved PTOS, the track seeking is conducted in the following procedures:

1. Apply the maximum input voltage for acceleration. The velocity of the head is shown in the dashed line in Fig. 3.3;

2. When the head velocity (dashed line in Fig. 3.3) intersects with the velocity-position profile (solid line) for deceleration, velocity control is used to follow the profile. Note if the control input is changed at Point B in Fig. 3.3, an overshoot may occur due to the current response delay. Therefore, the servo is switched to the deceleration mode before the head reaches the velocity-position line (Point A). The head velocity will gradually move toward the desired velocity profile;

3. When the head velocity reaches zero, switch the HDD servo from the velocity control mode to the position feedback control mode.

In this approach, the design of the input voltage profile depends on the designer's experience, so does the velocity profile for the track seeking mode. Moreover, the velocity profile is designed without considering the errors introduced in the discretization for the digital HDD servo.

3.1.2 Motivation and Basic Structure of 2DOF Control

The primary motivation for 2DOF control is to solve the settling problems associated with MSC. 2DOF control structure used one unified servo. The unified controller does not have the mode changes, and therefore avoids abrupt control input changes that may exacerbate the settling.
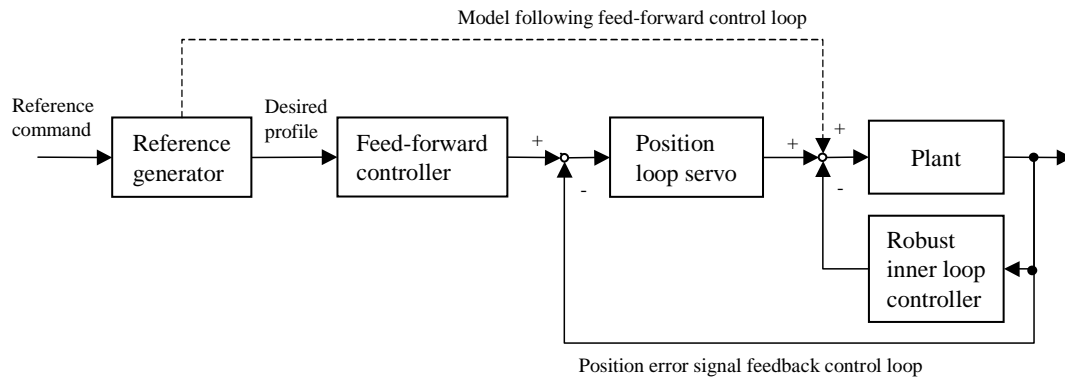
Figure 3.4: 2DOF control structure.

The 2DOF control structure is shown in Fig. 3.4. It has three major components: 1) robust feedback controller; 2) feedforward controller, and 3) reference generator. A 2DOF controller with DOB used for HDD servo is illustrated in Fig. 3.7, in which the three components are:

1. A discrete DOB, in addition to the position loop controller $C\left(z^{-1}\right)$;

2. A feedforward controller $G_{ff}\left(z^{-1}\right)$ and a bias compensator;

3. A position reference generator.

The reference generator provides the desired position profile for track seeking. The bias compensator is for compensating the pivot friction and the compliance torque from the flexible printed circuit (FPC, see Fig. 1.2).

3.2 Robust Feedback Control

In the 2DOF control, either a DOB [29] [19] or an ARC [69] can be used as the inner-loop robust controller. Figs. 3.7 and 3.17 illustrate the implementations. The robust controller is used to assure the servo system to have consistent behaviors even with unknown plant dynamics and external disturbances. As a result, the robust controller also leverages the advantage of feedforward control. The effectiveness of a feedforward controller is greatly affected by the knowledge of the servo system.

The use of DOB or ARC in the inner-loop eases the position-loop controller design, which is also based on the nominal plant model.

DOB and ARC are described in Section 3.2.1 and 3.2.2, respectively. Their effects on the HDD servo system are simulated and compared in Section 3.2.3.

3.2.1 Disturbance Observer (DOB)

The introduction of DOB is separated into two parts in this section: the first part describes the concept and analysis in continuous-time domain, and the second part discusses the design issues in discrete-time domain. Further details about DOB can be found in [37], [37], [39], [19], [58], and [56].

Continuous Time DOB Concepts and Analysis

DOB estimates the disturbance by subtracting known input from the estimated total input to the plant. The total input is obtained by processing the plant output through the inverse of the nominal plant model. The disturbance estimate can then be used to cancel

the original disturbance. The continuous-time domain DOB structure is shown in Fig. 3.5. An equivalent block diagram is shown in Fig. 3.6. In these figures, c is DOB input, u is the control input, d is the system disturbance, n is the sensor noise, and y is the system output. The nominal model of plant $G_p(s)$ is given by $G_n(s)$, which in general is a reduced-order system approximating $G_p(s)$. $Q(s)$ is a low pass filter to make the DOB realizable. Note that $G_n^{-1}(s)$ in Fig. 3.6 may not be proper (i.e., the order of the numerator exceeds that of the denominator). $Q(s)G_n^{-1}(s)$ can be made proper with an appropriately selected relative degree for $Q(s)$. $Q(s)$ is also tuned for disturbance rejection, noise attenuation and robustness. It is referred to as the Q filter [58], given as

$$Q(s) = \frac{(3\tau s + 1)}{(\tau s)^3 + 3 (\tau s)^2 + 3\tau s + 1} \tag{3.3}$$

where τ is a adjustable time constant of the DOB. The following relations can be derived from Fig. 3.6:

$$G_{cy}(s) = \frac{G_p(s)G_n(s)}{G_n(s) + Q(s)G_p(s) - Q(s)G_n(s)} \tag{3.4}$$

$$G_{dy}(s) = \frac{G_p(s)G_n(s)\,(1 - Q(s))}{G_n(s) + Q(s)G_p(s) - Q(s)G_n(s)} \tag{3.5}$$

$$G_{ny}(s) = \frac{G_p(s)Q(s)}{G_n(s) + Q(s)G_p(s) - Q(s)G_n(s)} \tag{3.6}$$

where $G_{\cdot y}(s)$ denotes the transfer function from $\cdot$ to y.

It can be found that as $Q(s)$ approaches 1 at low frequencies, $G_{cy}(s)$ approaches $G_n(s)$ and $G_{dy}(s)$ approaches 0. As $Q(s)$ approaches 0 at high frequencies, $G_{ny}(s)$ approaches 0. Figure 3.6 shows that DOB closes a high gain inner loop around the plant at frequencies where $Q(s) \approx 1$. Assuming $G_p(s) = G_n(s)$, from Fig. 3.6, it is easy to derive that the sensitivity function for the DOB loop is $1 - Q(s)$, and the complimentary sensitivity
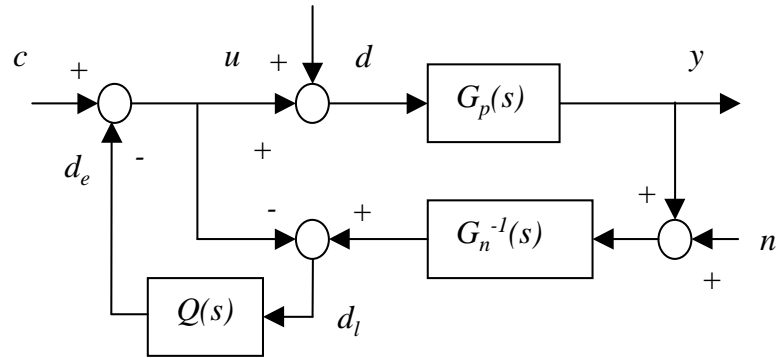
Figure 3.5: Continuous-time DOB
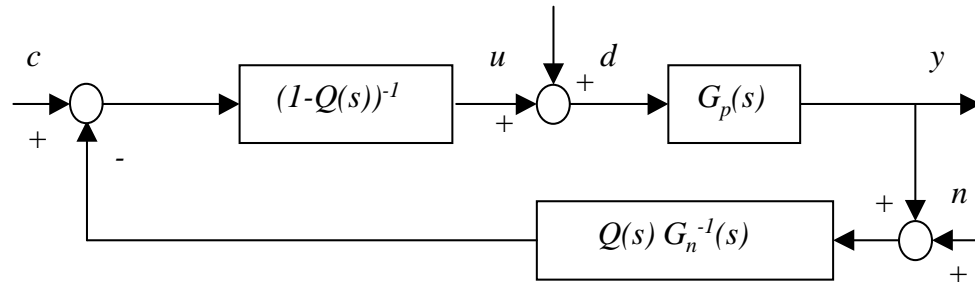
Figure 3.6: Alternative representation of the continuous-time DOB.

function is simply $Q(s)$. The open-loop dynamics of the DOB loop is $Q(s)/(1 - Q(s))$. To ensure that the DOB loop is stable, the infinity norm of $Q(s)\Delta(s)$ should be less than 1, where $\Delta(s)$ is the multiplicative perturbation of the plant. i.e.

$$G_p(s) = G_n(s)\left(1 + \Delta(s)\right) \tag{3.7}$$
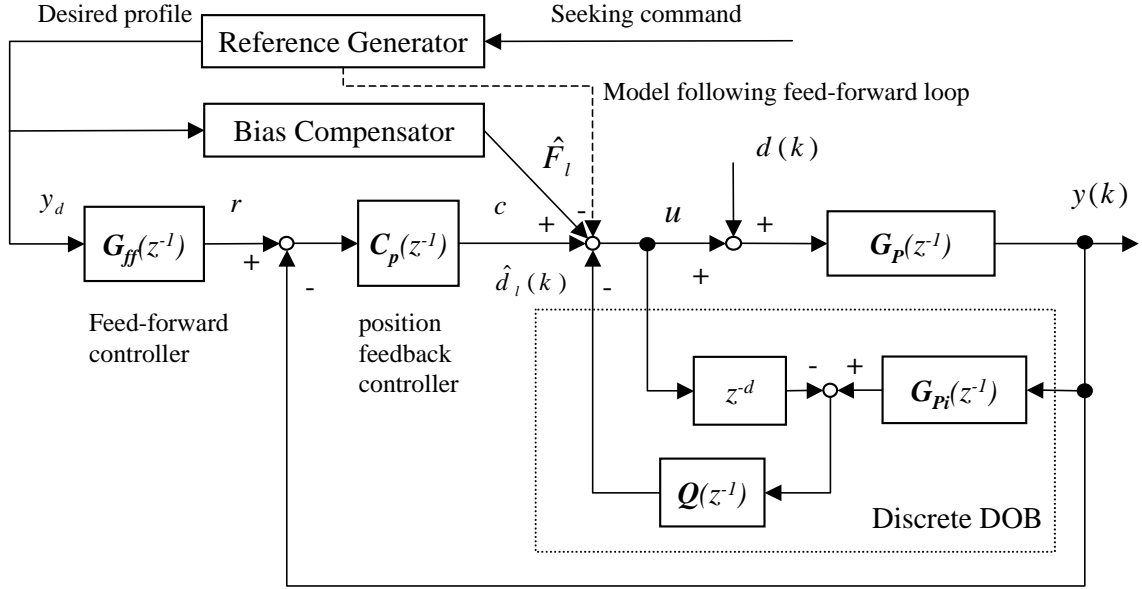
Figure 3.7: 2DOF Control with DOB

Discrete-Time DOB Implementation

In practice, the discrete-time DOB is implemented. A ZOH equivalent model of the plant $G_p(s)$, denoted as $G_p(z^{-1})$, is given by

$$G_p(z^{-1}) = G_{pn}(z^{-1})(1 + \Delta(z^{-1})) \tag{3.8}$$

$$G_{pn}(z^{-1}) = \frac{z^{-d}B(z^{-1})}{A(z^{-1})} \tag{3.9}$$

where $G_{pn}(z^{-1})$ represents the nominal plant, and $\Delta(z^{-1})$ is the multiplicative uncertainty term. $\Delta(z^{-1})$ is assumed to be a stable discrete-time transfer function. DOB compensates the external disturbance $d(k)$ by its estimate $\hat{d}_l(k)$. Analogous to the continuous-time case, the estimate is obtained by comparing the control signal u with the estimated input synthesized by the inverse of the nominal model $P_n(z^{-1})$ and the plant output $y(k)$. The

realizable inverse of the nominal plant is given as

$$G_{pi}\left(z^{-1}\right) = \frac{B\left(z^{-1}\right)}{A\left(z^{-1}\right)} \tag{3.10}$$

Note in Fig. 3.7, the delay z^{-d} in $P_n\left(z^{-1}\right)$ is applied to u, instead of using time advance z^d in $P_i\left(z^{-1}\right)$. If $\frac{B(z^{-1})}{A(z^{-1})}$ possesses unstable zeros, the zero phase inversion technique [54] can be used.

The transfer function from c to y is the synthesized plant model adjusted by the DOB loop. It is

$$G_{cy}\left(z^{-1}\right) = \frac{G_p\left(z^{-1}\right)}{\left(1 + G_p\left(z^{-1}\right)G_{pi}\left(z^{-1}\right)Q\left(z^{-1}\right) - z^{-d}Q\left(z^{-1}\right)\right)} \tag{3.11}$$

Choices of Q filter and $G_{pn}\left(z^{-1}\right)$ are the two primary factors in the DOB design. $G_{pn}\left(z^{-1}\right)$ does not have to be the nominal plant model. Because DOB affects mainly the low-frequency range, higher-frequency resonances can be ignored in $G_{pn}\left(z^{-1}\right)$. $G_{pn}\left(z^{-1}\right)$ and $G_{cy}\left(z^{-1}\right)$ using a pure inertia for the Fujitsu M2954 plant model are shown in Fig. 3.8. DOB adjusts $G_{cy}\left(z^{-1}\right)$ to approximate $G_{pn}\left(z^{-1}\right)$ at low frequencies below $1KHz$. Above the frequency, $G_{cy}\left(z^{-1}\right)$ is almost identical to the real plant $G_p\left(z^{-1}\right)$.

Note that there is still difference between $G_{cy}\left(z^{-1}\right)$ and $G_{pn}\left(z^{-1}\right)$ at low frequencies. The difference is caused by the modelling errors of $G_{pn}\left(z^{-1}\right)$ from the real plant.

By choosing the nominal plant model $G_{pn}\left(z^{-1}\right)$ closer to $G_p\left(z^{-1}\right)$ at low frequencies, the difference between $G_{cy}\left(z^{-1}\right)$ and $G_{pn}\left(z^{-1}\right)$ can also be reduced. When the pivot friction is modeled in $G_{pn}\left(z^{-1}\right)$ (Eq. 2.11), the frequency responses of $G_{cy}\left(z^{-1}\right)$, $G_{pn}\left(z^{-1}\right)$ and $G_p\left(z^{-1}\right)$ for the M2954 drive are shown in Fig. 3.9.

As shown in Fig. 3.7, the estimated lumped disturbance $\widehat{d_l}\left(k\right)$ includes the estimate of $d\left(k\right)$ as well as that of an equivalent disturbance due to modeling uncertainties. At
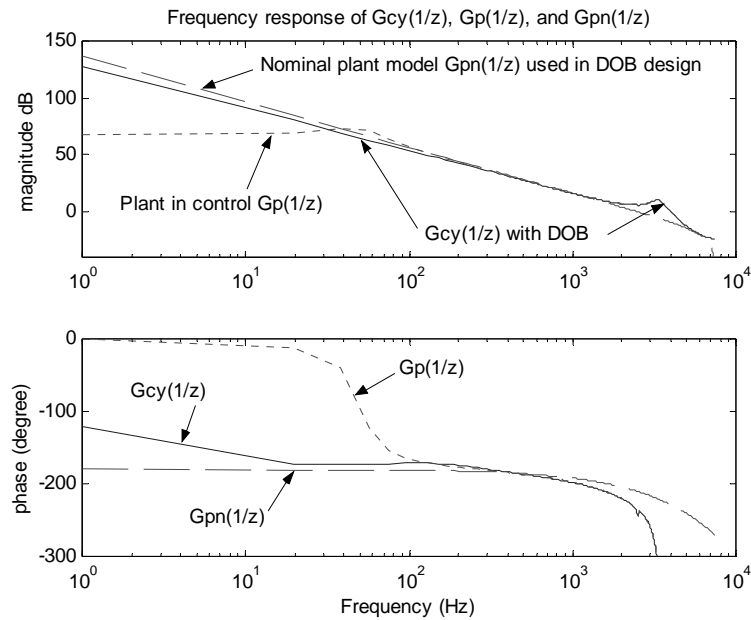
Figure 3.8: Use a pure inertia model as $G_{pn}\left(z^{-1}\right)$ in DOB desgin. $G_{cy}\left(z^{-1}\right)$ approximates $G_{pn}\left(z^{-1}\right)$ at low frequencies.
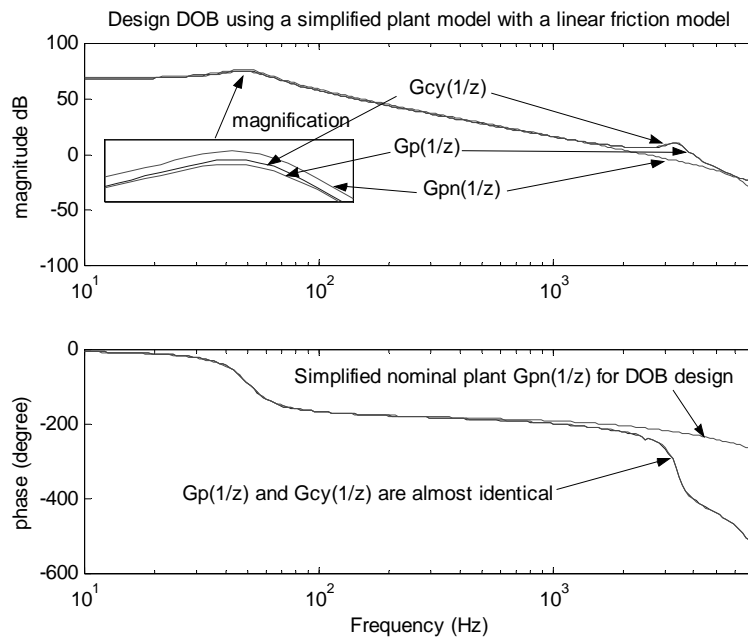
Figure 3.9: Include pivot friction in the nominal plant for DOB design. The difference between $G_{cy}\left(z^{-1}\right)$ and $G_{pn}\left(z^{-1}\right)$ at low frequencies can be reduced.

low frequencies, DOB forces $G_{cy}\left(z^{-1}\right)$ to approximate $G_{pn}\left(z^{-1}\right)$. $Q(z^{-1})$ is selected to be 1 at low frequencies, and zero at higher frequencies. The bandwidth of the lowpass filter $Q(z^{-1})$ determines the overall performance of the DOB.
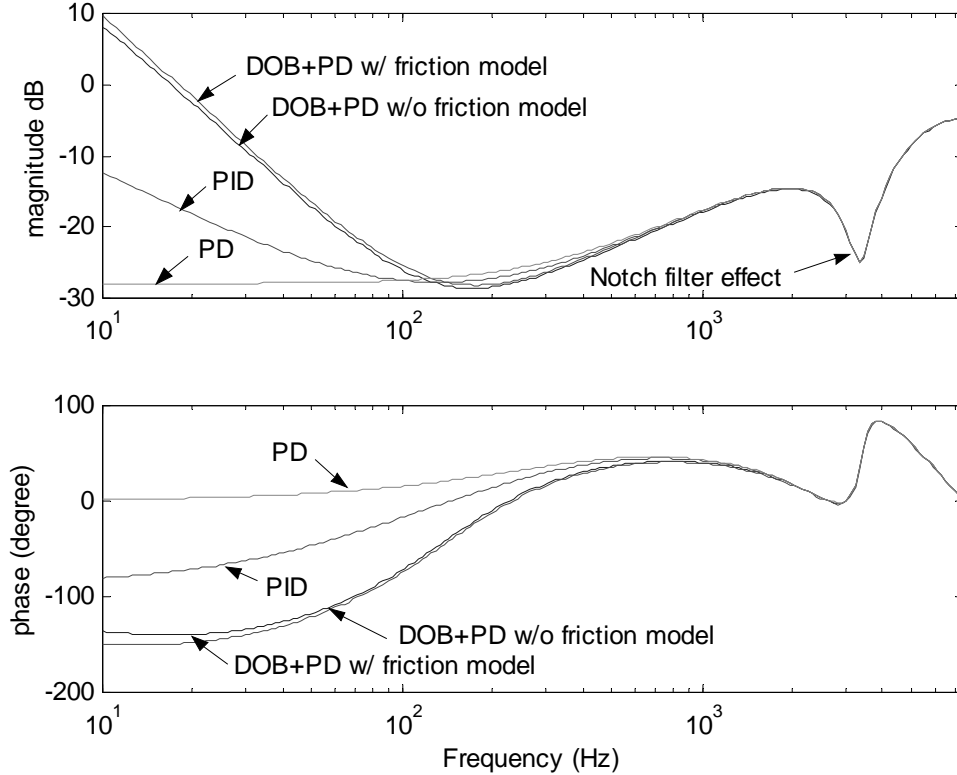
Figure 3.10: Open-loop transfer functions of different servo controllers

The DOB based servo is shown in Fig. 3.11, in which the disturbance torque, sensor noise, and disk modes are denoted as $d\left(k\right)$, $n\left(k\right)$, and $m\left(k\right)$. Control input $u\left(k\right)$ can be expressed as a function of the measured position $y\left(k\right)$ as

$$
\begin{aligned}
u\left(k\right) &= C_p\left(z^{-1}\right)\left(r\left(k\right) - y\left(k\right)\right) - Q\left(z^{-1}\right)\left(G_{pi}\left(z^{-1}\right)y\left(k\right) - z^{-d}u\left(k\right)\right) \\
&= C_p\left(z^{-1}\right)\left(r\left(k\right) - y\left(k\right)\right) - Q\left(z^{-1}\right)G_{pi}\left(z^{-1}\right)y\left(k\right) + Q\left(z^{-1}\right)z^{-d}u\left(k\right) \quad (3.12)
\end{aligned}
$$
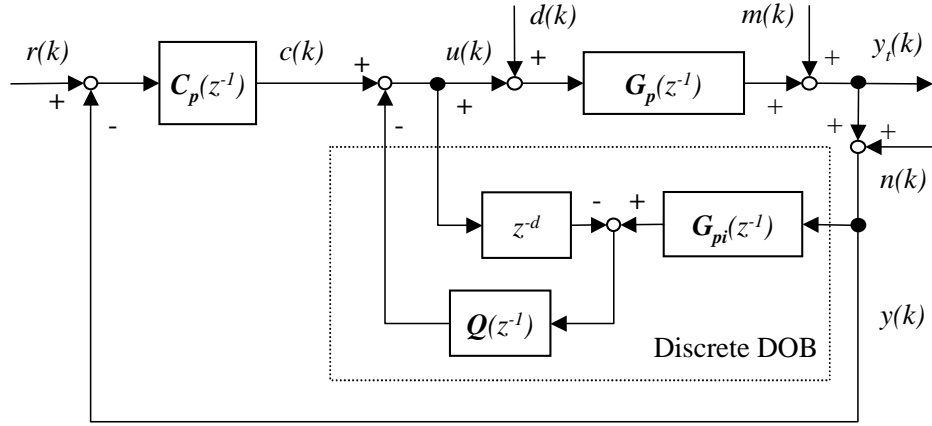
Figure 3.11: DOB for HDD servo.

therefore

$$u\left(k\right) = -\frac{C_p\left(z^{-1}\right) + Q\left(z^{-1}\right)G_{pi}\left(z^{-1}\right)}{1 - z^{-d}Q\left(z^{-1}\right)}y\left(k\right) + \frac{C_p\left(z^{-1}\right)}{1 - z^{-d}Q\left(z^{-1}\right)}r\left(k\right) \qquad (3.13)$$

Define the overall feedback controller $C_{fb}\left(z^{-1}\right)$ as the transfer function from $y\left(k\right)$ to $-u\left(k\right)$, and the feedforward term $C_{ff}\left(z^{-1}\right)$ from $r\left(k\right)$ to $u\left(k\right)$, then

$$C_{fb}\left(z^{-1}\right) \;=\; \frac{Q\left(z^{-1}\right)G_{pi}\left(z^{-1}\right) + C_p\left(z^{-1}\right)}{1 - z^{-d}Q\left(z^{-1}\right)} \qquad (3.14)$$

$$C_{ff}\left(z^{-1}\right) \;=\; \frac{C_p\left(z^{-1}\right)}{1 - z^{-d}Q\left(z^{-1}\right)} \qquad (3.15)$$

Equation 3.13 can be expressed as

$$u\left(k\right) = -C_{fb}\left(k\right)y\left(k\right) + C_{ff}\left(z^{-1}\right)r\left(k\right) \qquad (3.16)$$

Because

$$y_t(k) = m(k) + G_p(z^{-1})(d(k) + u(k))$$

$$= m(k) + G_p(z^{-1}) d(k) + G_p(z^{-1}) \left(-C_{fb}(z^{-1}) y(k) + C_{ff}(z^{-1}) r(k)\right)$$

$$= m(k) + G_p(z^{-1}) d(k) - G_p(z^{-1}) C_{fb}(z^{-1}) (y_t(k) + n(k))$$

$$+ G_p(z^{-1}) C_{ff}(z^{-1}) r(k) \tag{3.17}$$

the true position

$$y_t(k) = \frac{1}{1 + G_p(z^{-1}) C_{fb}(z^{-1})} m(k) + \frac{-G_p(z^{-1}) C_{fb}(z^{-1})}{1 + G_p(z^{-1}) C_{fb}(z^{-1})} n(k)$$

$$+ \frac{G_p(z^{-1})}{1 + G_p(z^{-1}) C_{fb}(z^{-1})} d(k) + \frac{G_p(z^{-1}) C_{ff}(z^{-1})}{1 + G_p(z^{-1}) C_{fb}(z^{-1})} r(k) \tag{3.18}$$

By defining the open-loop transfer function as $G_{op}(z^{-1}) = G_p(z^{-1}) C_{fb}(z^{-1})$, the sensitivity function as $S(z^{-1}) = \frac{1}{1 + G_{op}(z^{-1})}$, the complementary sensitivity function as $T(z^{-1}) = \frac{G_{op}(z^{-1})}{1 + G_{op}(z^{-1})}$, and disturbance transfer function as $D(z^{-1}) = \frac{G_p(z^{-1})}{1 + G_{op}(z^{-1})}$, Equation 3.18 can be expressed as

$$y_t(k) = S(z^{-1}) m(k) - T(z^{-1}) n(k) + D(z^{-1}) d(k) + D(z^{-1}) C_{ff}(z^{-1}) r(k) \tag{3.19}$$

Note that the closed-loop transfer function from $r(k)$ to $y(k)$ is not $T(z^{-1})$, because the transfer functions from $r(k)$ and $-y(k)$ to $u(k)$ are not the same. For a typical servo structure as shown in Fig. 2.9, the control input $u(k)$ is obtained by processing $r(k) - y(k)$. For a multi-loop feedback system in Fig. 3.11, both $r(k) - y(k)$ and $y(k)$ are processed independently to generate the control effect.

To get more insight on the DOB structure, frequency responses of the following four different controllers for M2954 are shown in Fig. 3.10:

1. DOB based controller, with $Q\left(z^{-1}\right)$ chosen as the discretized version of $Q\left(s\right)$ (3.3), with $\tau = 0.001$. The pure inertia model without pivot friction is used as $G_{pn}\left(z^{-1}\right)$. The position loop controller $C_p\left(z^{-1}\right)$ uses the PID controller given in Eq. 2.18, with the nominal gains K_d and K_p given in Table 2.2, and $K_i = 0$;

2. The same DOB based controller as in 1, except that the pivot friction mode is included in $G_{pn}\left(z^{-1}\right)$.

3. The same PID controller as in 1;

4. The same PID controller as in 1, except $K_i = 0$. This make it a PD controller.

The same notch filter (2.19) is added to all the controllers.

Note in Eq. 3.14 that $Q\left(z^{-1}\right)$ is approximately 1 at low frequencies and 0 at high frequencies. $C_{fb}\left(z^{-1}\right)$ can be observed to have a high gain at low frequencies, and approximate to $C_p\left(z^{-1}\right)$ at high frequencies. Because of the low frequency high gain introduced by DOB in the inner-loop, the integral control action is built-in. There is no need for the position loop controller $C_p\left(z^{-1}\right)$ to have an additional integral control action. This argument is supported by the frequency analysis in Fig. 3.10. Note that in that figure, the DOB based servo, either with a linear pivot friction mode or without, has a much higher gain at low frequencies; the PID controller has a higher gain than that of the PD controller at low frequencies. All the four controllers merge together at high frequencies.

Their sensitivity functions, servo open-loop transfer functions, and disturbance transfer functions are shown in Fig. 3.12, 3.13, and 3.14, respectively. The DOB based servo exhibits much higher attenuation ability at low frequencies, at which a large portion

of the HDD servo TMR sources are concentrated.
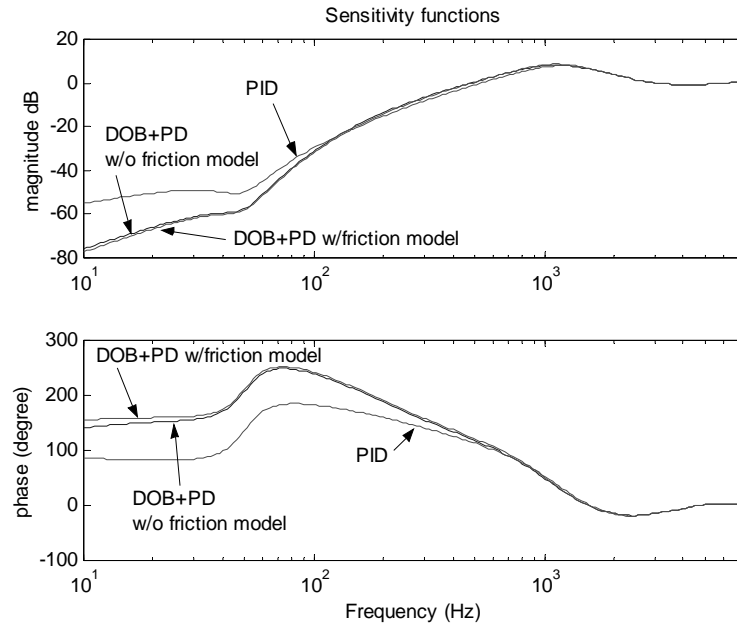
Figure 3.12: Sensitivity functions.

Due to the temperature variations and the R/W channel gain shifting, HDD servo open-loop gain variations are common. Figure 3.15 illustrates the frequency responses of the original plant and the perturbed plant with $\pm50\%$ gain variations. DOB can be used to solve the gain variation problems, with results shown in Fig. 3.16. The inner-loop system $G_{cy}\left(z^{-1}\right)$ (Eq. 3.11) is regarded as the synthesized plant for $C_p\left(z^{-1}\right)$.

3.2.2 Adaptive Robust Control (ARC)

An alternative robust controller used in the inner loop is ARC, which is illustrated in Fig. 3.17. As in the DOB design, the objective of ARC is to synthesize a control input u such that the resulting system from c to y behaves like its nominal model, even under the
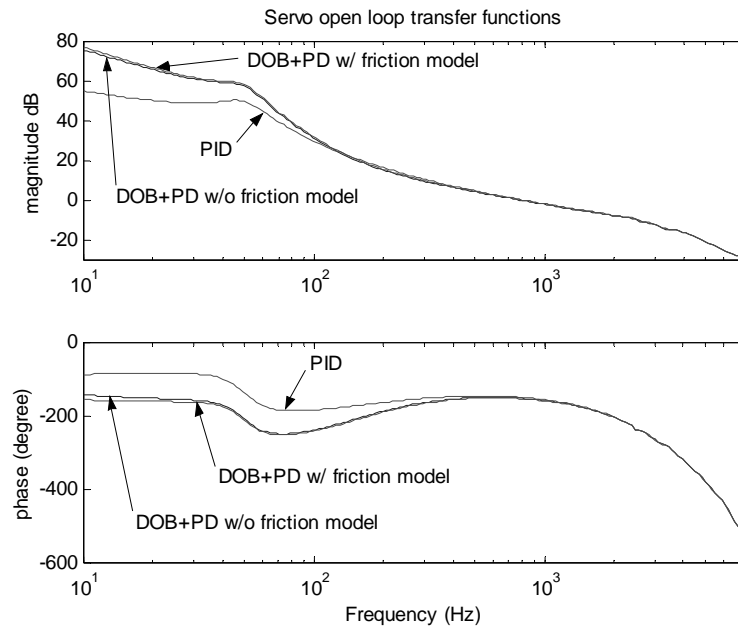
Figure 3.13: Open loop transfer functions
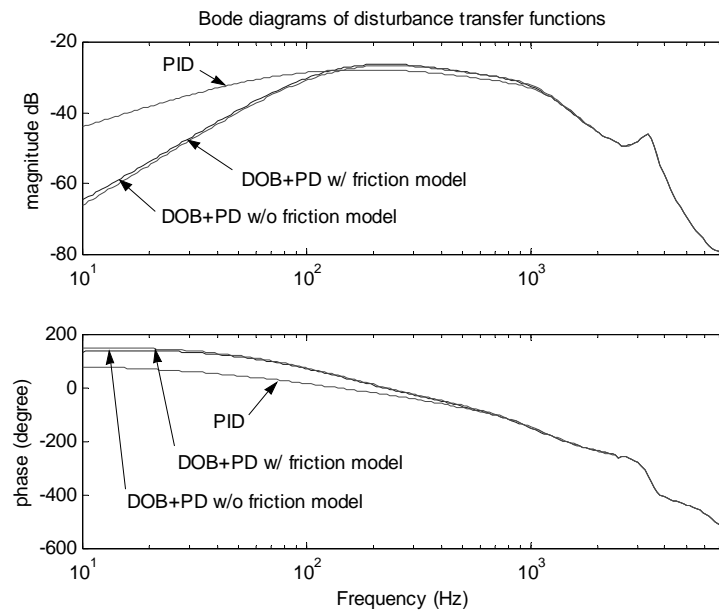
Figure 3.14: Disturbance transfer functions
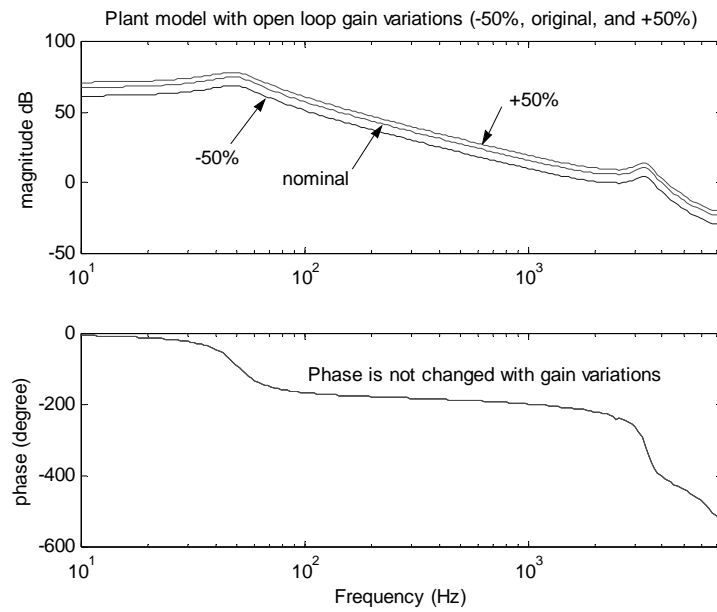
Figure 3.15: Servo plant gain variations.
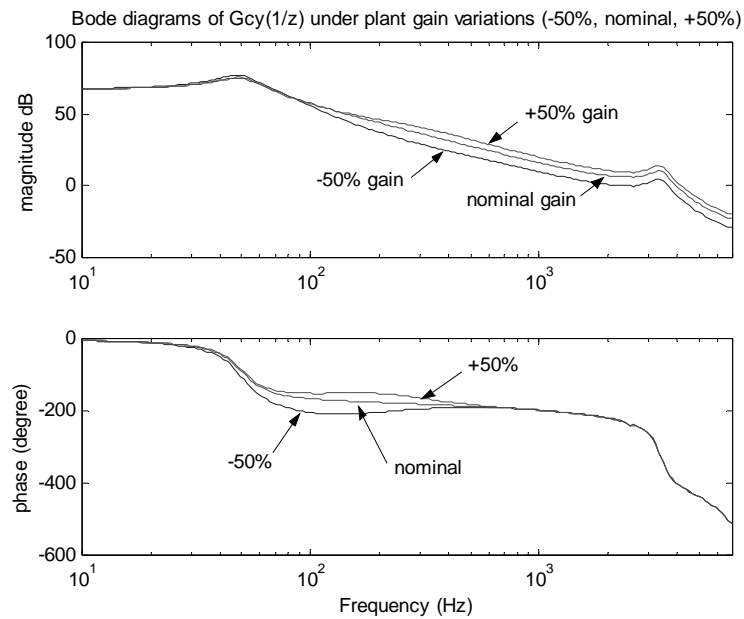
Figure 3.16: Inner loop system $G_{cy}\left(z^{-1}\right)$ in the DOB based servo, under $\pm 50\%$ gain variations of the plant in control.
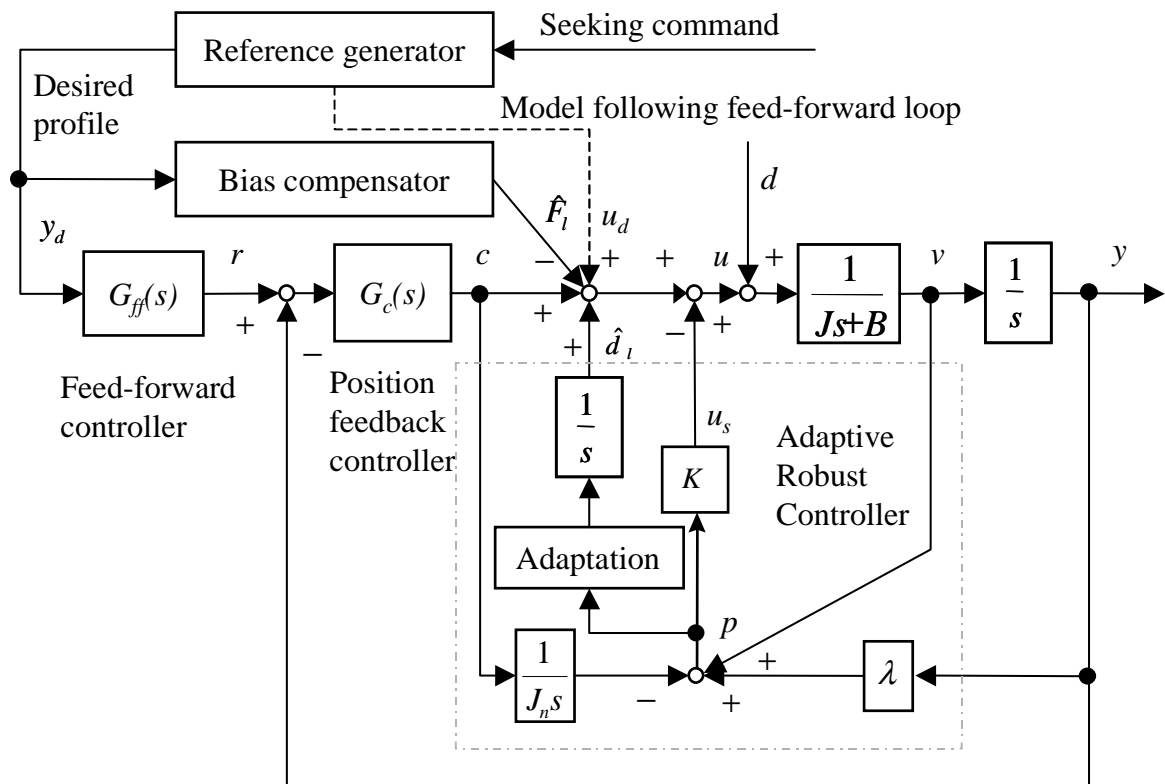
Figure 3.17: 2DOFS with ARC

presence of the external disturbance d. Considering the simplified model of a HDD

$$J\ddot{y} + B\dot{y} = u + d \tag{3.20}$$

we want

$$J_n\ddot{y} + B_n\dot{y} = c \tag{3.21}$$

where J_n and B_n are the nominal values of J and B, respectively. To gain insight about the proposed ARC and its advantages, we assume that the variations of J and B can be neglected in the design, i.e., $J = J_n$ and $B = B_n$. Dealing with the bounded disturbance d is emphasized in this design. Define a switching-function-like quantity p as

$$p = \dot{y} + \lambda y - \frac{1}{J_n}\int_0^t c(\tau)d\tau \tag{3.22}$$

where $\lambda = \frac{B_n}{J_n}$. Then

$$J_n\dot{p} = u + d - c \tag{3.23}$$

If $\dot{p} = 0$, then we have the desired relationship in (3.21). If all signals involved are uniformly continuous, then $p \to 0$ means $\dot{p} \to 0$. Therefore, u could be synthesized by feedback control such that p is as small as possible. Let the control law be

$$u = u_s + u_f,\, u_s = -Kp,\, u_f = c - \widehat{F_l} - \widehat{d_l} \tag{3.24}$$

where $K > 0$, $\widehat{F_l}$ is any fixed bias compensation, and $\widehat{d_l}$ is the estimate of the lumped uncompensated disturbance $d_l = d - \widehat{F_l}$. d_l is bounded and can be assumed that

$$d_l \in [d_m, d_M] \tag{3.25}$$

where d_m and d_M are known constants. From (3.24) and (3.23), the p dynamics is

$$J_n \dot{p} + Kp = -\widetilde{d_l} \tag{3.26}$$

where $\widetilde{d_l} = \widehat{d_l} - d_l$ is the estimation error.

Equation (3.26) is a stable first-order system with respect to p with a bounded uncompensated disturbance input $\widetilde{d_l}$ if fixed $\widehat{d_l}$ is used. From

$$|p(\infty)| \leq \widetilde{d_l}(\infty)/K \tag{3.27}$$

p can be made as small as possible by increasing feedback gain K. The modeling uncertainties are addressed by the robust feedback control. However in practice, K can not be arbitrarily large. Once K is fixed, the final tracking error p, is proportional to the size of the modeling uncertainty $\widetilde{d_l}$. In order to further improve performance, an adaptive algorithm can be added to make a better estimate of the lumped disturbance $\widehat{d_l}$. We can update $\widehat{d_l}$ on-line by the following adaptation law

$$\dot{\widehat{d_l}} = \{ \begin{array}{ll} 0 & if \; (\widehat{d_l} = d_M \text{ and } p > 0) \text{ or } (\widehat{d_l} = d_m \text{ and } p < 0) \\ \Gamma p & \text{otherwise} \end{array} \tag{3.28}$$

where $\Gamma > 0$ is the adaptation rate. It can be proven in the same way as in [69] that if the disturbance is constant, the modeling uncertainty $\widetilde{d_l}$ converges to zero and zero final tracking error can be obtained for any feedback gain K. If $d_m < \widehat{d_l}(t) < d_M$ for all t, then the error dynamics is

$$J_n \dot{p} + Kp + \Gamma \int_0^t p \, dt = d_l \tag{3.29}$$

Thus, the adaptation law can be interpreted as adding an integrator of p. Further remarks on ARC can be found in [69], [67], [66] and [68].

Modeling Parameters	Symbol	Value
Track to track pitch	L_{track}	$6.245 \ \mu m$
Track density	TPI	$4067.4 \ track/inch$
Spindle speed	RPM	$7200 \ rev/Minute$
Sampling time	T_s	$80 \ \mu s$
Arm distance	L_{arm}	$0.052 \ m$
VCM coil resistance	R_m	$4.9 \ \Omega$
Current sensor resistance	R_s	$0.715 \ \Omega$
Coil inductance	L	$0.637 \times 10^{-3} \ H$
Back e.m.f.	K_{eb}	$7.57 \times 10^{-2} \ Vs/rad$
Torque constant	K_t	$7.57 \times 10^{-2} \ Nm/A$
Moment of inertia	J	$5.7 \times 10^{-6} \ Kgm^2$
Closed-loop PA gain	G_{pacl}	0.5556
PA op-amp gain	G_{pa}	20000
PA close loop gain adjustment	G_{op}	0.2381
Op-amp maximum voltage output	U_{max}	$9 \ V$
Actuator later mode frequency	f_{LM}	$4000 \ Hz$

Table 3.1: Plant parameters of the NEC drive

3.2.3 Simulation Comparisons

Comparisons of effectiveness of DOB and ARC through simulations have been made using a NEC hard disk drive model. The plant model uses the structure illustrated in Fig. 2.1, and parameters given in Table 3.1.

For comparison of the simulation results, the following performance index are used. They are the average tracking performance index

$$L_2[e] = \sqrt{\frac{\sum_{k=1}^{N} e^2(k)}{N}} \tag{3.30}$$

in units of $track$, the maximum tracking error e_M in $track$, the normalized control input variations

$$L_2\left[\Delta u\right] = \sqrt{\frac{1}{N}\sum_{k=1}^{N}\left[u(k) - u(k-1)\right]^2} \qquad (3.31)$$

and the control input chattering index

$$c_u = L_2\left[\Delta u\right]/L_2\left[u\right] \qquad (3.32)$$

During the simulations of the NEC drive using either DOB or ARC, an uncompensated bias $0.1V$ (equivalent to torque $0.0078\ Nm$) is present from the initial time at $t = 0\ ms$. An external shock $0.2V$ (equivalent to torque $0.0156\ Nm$) enters the control input channel at time $t = 5\ ms$. A white noise with a standard deviation $0.1\ mV$ is applied in the control input channel throughout the simulations.

Both ARC and DOB in the comparisons are designed in the continuous-time domain, and then transformed into discrete-time domain for simulations.

In the ARC design, the feedback controller $G_c(s)$ is designed to make the closed-loop transfer function with a nominal plant model critically damped, and have a corner frequency of $800Hz$. K and Γ are chosen to make the dynamics described in Eq. 3.29 to have a bandwidth at about $800Hz$. ARC controller designed in the continuous-time domain is transformed into discrete-time domain using the forward euler approximation. Considering the physical meaning of the bounds of the estimated disturbance, d_M is set to $0.5\ Volts$ and d_m is set to $-0.5\ Volts$.

In the DOB design, the Q filter is chosen as

$$Q(s) = (3\tau s + 1)/\left((\tau s)^3 + 3(\tau s)^2 + 3\tau s + 1\right) \qquad (3.33)$$

	D_1	A_1	D_2	A_2	D_3	A_3	D_4	A_4	D_5	A_5	D_6	A_6
e_M	.37	.15	.37	.16	.37	.16	.57	.27	.56	.39	1.23	.52
$L_2[e]$	.08	.04	.10	.04	.08	.04	.16	.07	.3	.29	.45	.32
$L_2[\Delta u]$	.07	.07	.07	.07	.12	.19	.12	.15	.13	.13	.17	.18
c_u	.89	.98	.80	.85	.63	.63	.53	.58	.11	.11	.13	.17

Table 3.2: Comparison of DOB and ARC

where τ is set to make $Q(s)$ have a time constant $\tau = 0.15\ ms$, therefore a bandwidth at about $1200Hz$. $Q(s)$ is transformed into the discrete-time domain using the bilinear transformation.

Simulations using ARC and DOB are performed for each of the following 6 cases. Each of them contains a track seeking phase and a track following phase after the seek:

1. 1 track seek of the nominal plant;

2. 1 track seek of the perturbed plant with 20% gain variation.

3. 8 tracks seek of the nominal plant;

4. 8 tracks seek of the perturbed plant with 20% gain variation;

5. 1000 tracks seek of the nominal plant;

6. 1000 tracks seek of the perturbed plant with 20% gain variation.

Simulation results are summarized in Table 3.2. D and A stand for DOB and ARC in the table, respectively. Their subscript number from 1 to 6 refers to the case number listed above. For Case 1 and Case 2, simulation results are also shown in Figs. 3.18 and 3.19.

The results show that both DOB and ARC (except for D_6) assure tracking performance with errors smaller than one track throughout the seek transient. Note that the scales of the upper left plots (for DOB) are twice the scales of the upper right plots (for ARC) in both Figs. 3.18 and 3.19. These figures show that ARC is about two times more effective than DOB under the testing conditions. As we can see from Table 3.2, in Case 1, the maximum tracking error is 0.37 track with DOB, while it is only 0.15 track with ARC. The average tracking performance index $L_2[e]$ for ARC is also two times better than that of DOB. When model uncertainties are introduced in Case 2, the ARC approach still does better, with e_M and $L_2[e]$ about one half of those of the DOB approach. The advantages of ARC are also shown in Case 3 to Case 6, in terms of both e_M and $L_2[e]$.

The simulation results demonstrated that under the testing external disturbances, ARC is more robust and has achieved better performance. Compared with DOB, ARC can handle larger parameter variations. It also offers more flexibility because of the presence of the extra nonlinear robust control terms and the parameter adaptation to improve the transient response and tracking performance. Anti-integration windup mechanisms are built into ARC, so the control saturation problems are alleviated.

In the simulations, the velocity signal was assumed to be accessible for constructing p in the ARC design (see Fig. 3.17). In actual hard disk drives, the velocity signal is not directly measurable, and it has to be estimated. However, without requiring the velocity signal, the DOB structure was easier to implement. So far, DOB has been successfully implemented. The experimental results will be described in Chapter 4.
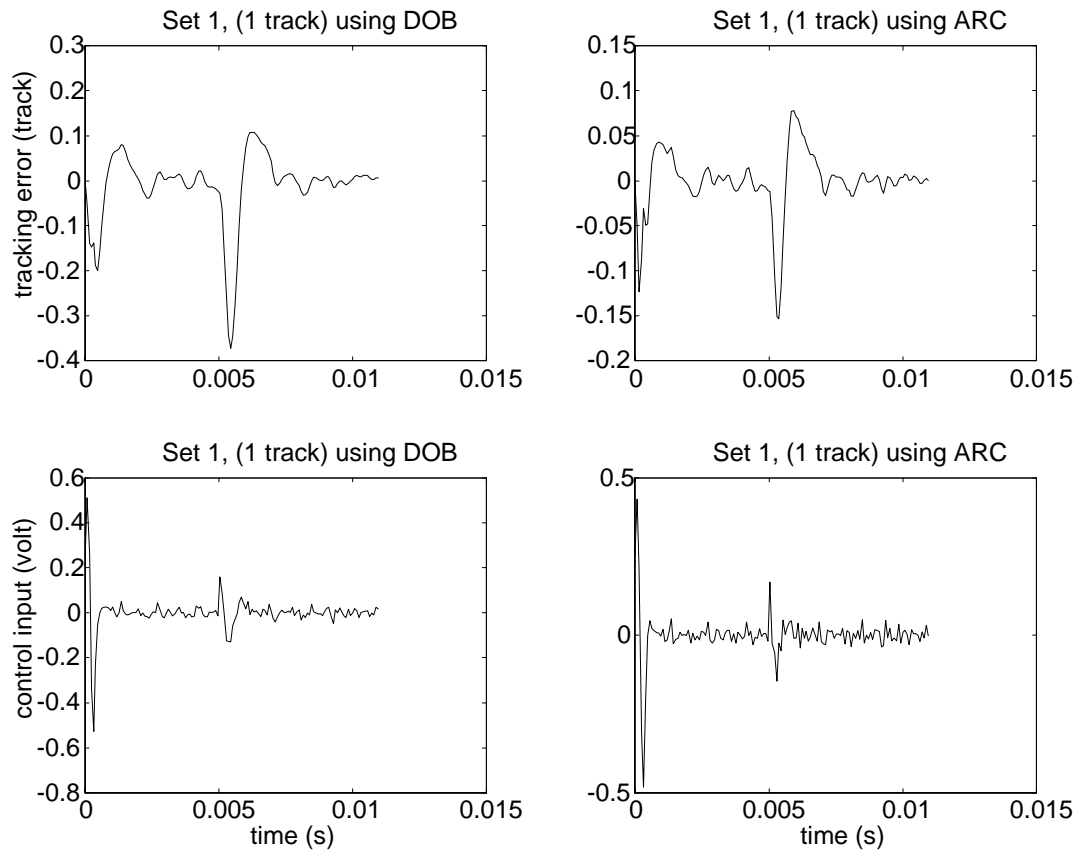
Figure 3.18: Simulation results for Set 1

3.3 Feedforward Control

The feedforward control is another important element of the 2DOF control structure. Zero Phase Error Tracking (ZPET) [55][40] or model following control can be used for the feedforward controller design. The controller is designed based on the closed-loop system dynamics and the nominal plant model. DOB or ARC is used to take care of the external disturbances and parameter variations.

ZPET is discussed in the Section 3.3.1. The model following control is discussed
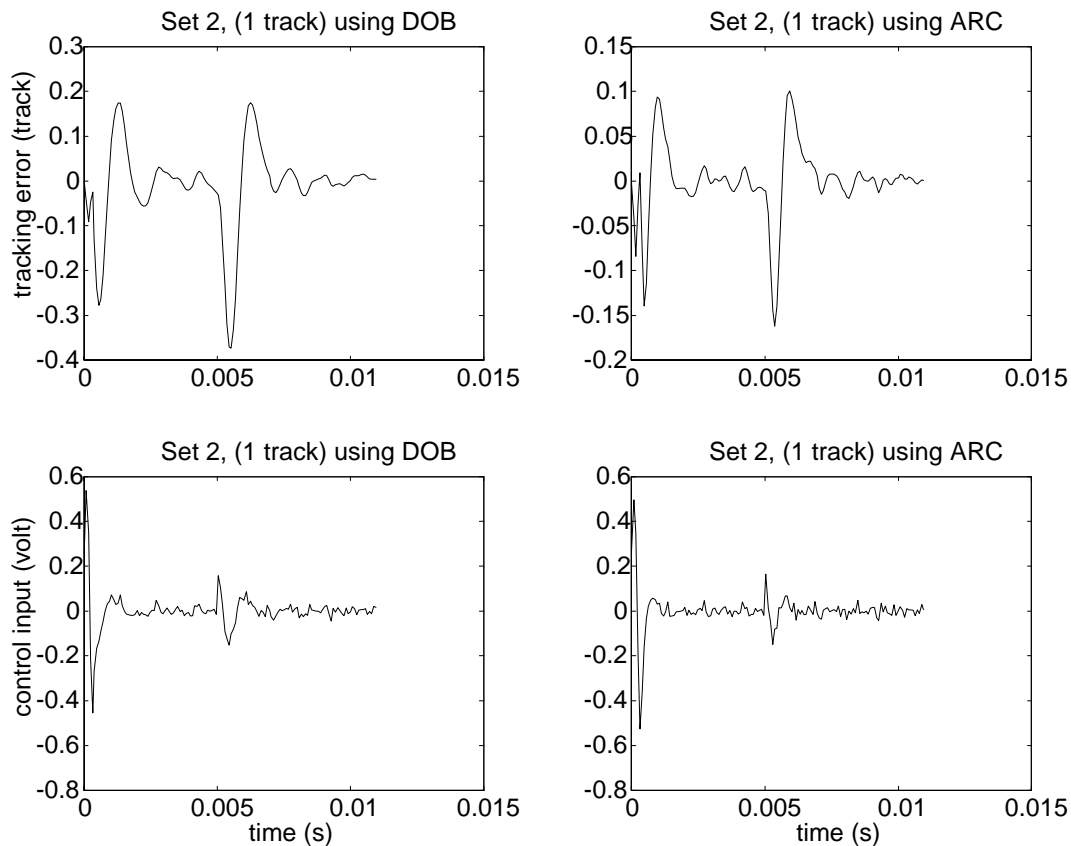
Figure 3.19: Simulation results for Set 2

briefly in Section 3.3.2.

3.3.1 Zero Phase Error Tracking Feedforward Control

The feedforward controller shapes the desired output to compensate for the dynamic lag of the closed-loop system. For the low sampling rate systems such as the HDD sector servos, feedforward control plays an important role in processing the reference profile for the closed-loop controller. Let the closed-loop system be expressed as

$$G_{clp} = \frac{z^{-d}B(z^{-1})}{A(z^{-1})} \tag{3.34}$$

where

$$A(z^{-1}) \quad = \quad 1 + a_1 z^{-1} + a_2 z^{-2} + ... + a_n z^{-n} \qquad (3.35)$$

$$B(z^{-1}) \quad = \quad b_0 + b_1 z^{-1} + b_2 z^{-2} + ... + b_m z^{-m} \qquad (3.36)$$

and $z^{-1} = e^{-sT}$. z^{-1} may be interpreted as an one-step delay operator. Then refer to Fig. 3.7, assuming disturbance $\widehat{F}_l = 0$ and $d(k) = 0$,

$$y(k) = -a_1 y(k-1) - ... - a_n y(k-n) + b_0 r(k-d) + ...b_m r(k-d-m) \qquad (3.37)$$

If it is desired for $y(k)$ to follow the desired output $y_d(k)$, the ideal feedforward controller is the inverse of $G_{clp}(z^{-1})$, i.e.

$$G_{ff}(z^{-1}) = \frac{z^d A(z^{-1})}{B(z^{-1})} \qquad (3.38)$$

Assuming that $y_d(k)$ is known d steps in advance of $y(k)$, the feedforward controller can be implemented as

$$r(k) \quad = \quad -b_0 r(k) - ... - b_m r(k-m) + y(k+d) + a_1 y(k+d-1) + ... + a_n y(k+d-n)$$

$$= \quad -b_0 r(k) - ... - b_m r(k-m) + y_d(k) + a_1 y_d(k-1) + ... + a_n y_d(k-n) \qquad (3.39)$$

Then the transfer function from y_d to y is

$$G_{ff}(z^{-1}) G_{clp} = \frac{z^d A(z^{-1})}{B(z^{-1})} \cdot \frac{z^{-d} B(z^{-1})}{A(z^{-1})} = 1 \qquad (3.40)$$

which implies $y(k) = y_d(k)$ under the ideal conditions.

Unfortunately, the ideal feedforward controller above can not be implemented when $B(z^{-1})$ possesses any zero outside the unit circle (unstable zeros). In this situation, the zero

phase error tracking (ZPET) controller is used to implement the feedforward controller. To introduce the idea of ZPET, the closed-loop transfer function is first written as

$$G_{clp}(z^{-1}) = \frac{z^{-d}B^+(z^{-1})B^-(z^{-1})}{A(z^{-1})}$$

where $B^-(z^{-1})$ contains all zeros outside of the unit circle, and $B^+(z^{-1})$ contains all zeros inside. The ZPET controller is [55]

$$G_{ZPET}(z^{-1}) = \frac{z^d A(z^{-1})B^-(z)}{[B^-(1)]^2 B^+(z^{-1})} \tag{3.41}$$

where $B^-(z)$ is obtained by replacing every z^{-1} in $B^-(z^{-1})$ with z.

The resulted transfer function from y_d to y is

$$G_{clp}(z^{-1})G_{ZPET}(z^{-1}) = \frac{B^-(z^{-1})B^-(z)}{[B^-(1)]^2} \tag{3.42}$$

Note that the ZPET controller cancels the closed-loop poles, stable zeros, and the phase shift due to unstable zeros. This transfer function in Eq. 3.42 has zero phase at all frequencies. This means that it does not introduce any phase shift for sinusoidal inputs. In another word, if the desired input has certain shape, its output will keep the shape unchanged.

3.3.2 Model Following Control

With the use of the robust controller ARC or DOB, the inner loop system behave as the nominal plant at low frequencies, where the frequency contents of the track seeking commands are concentrated. Using the nominal model of the plant in the reference generator, the desired control input u_d can be synthesized for open-loop control as shown in

Figs. 3.7 and 3.17. The track errors introduced by the modeling error are corrected by the closed-loop servo.

This model following control technique is used in the experiments for the 2DOF structure in the Fujitsu M2954 drive. The details are in Chapter 4.

3.4   Reference Generation

As shown in Fig. 3.4, 2DOF controller operates without the mode switches through the simultaneous use of a robust feedback controller and a feedforward controller. TMR performance for accurate track following is achieved by the robust feedback controller. Fast and smooth track seeking is accomplished by the feedforward controller along with the reference generator. It can be seen from Figs. 3.7 and 3.17 that the 2DOF control system is a position tracking system. Performance requirements and velocity constraints during the track seeking are all reflected in the position reference profile. This make the reference profile a key element in the 2DOF control structure.

For MSC, the seeking velocity profiles are designed based on a rigid body (double integrator) model. Such approaches did not consider the physical difference between the acceleration and the deceleration. Back $e.m.f.$, which behaves like the friction torque, resists the movement of the actuator, and slows down the acceleration. It also reduces the deceleration time. Reference generation model without considering the back $e.m.f.$ is not complete and therefore can not realize a smooth profile. Ishikawa, et al. [18] used a Voice Coil Motor (VCM) model which includes the back $e.m.f.$ effect. In [18], the eigenvectors of the VCM model are used for designing the reference trajectories. Yi and Tomizuka [73]

also proposed a reference design method using the same VCM model and additional off-line simulation results.

The requirements for the reference generation for 2DOF control servo system is listed in Section 3.4.1. One among them is to require that the reference profile have no overshoot at the end of a seek. At that time, the head velocity and the VCM current need to be zero simultaneously. To achieve this, a new method is proposed and developed. Similar to the reference generation method presented in [73], the reference generator uses the plant model with back $e.m.f.$ effects. It is described in Section 3.4.2. The reference profile is generated in two stages: the first stage is based on off-line simulations, and the second stage uses an on-line reference generator together with a data table saved in the first stage. These two stages are described in Section 3.4.4 and Section 3.4.3, respectively. In the second stage, the idea of SMART (Structural vibration Minimized AcceleRation Trajectory) [47] is utilized to adjust a seek profile. Comparisons of the new reference generation method with the conventional PTOS for MSC are made by simulations and experiments. The simulation results are presented in Section 3.4.5, and the experiments on the Fujitsu M2954 drive are discussed in Chapter 4.

3.4.1 Reference Profiles Requirements

The requirements for the reference profiles for the 2DOF control structure include the following:

1. It should generate aggressive profiles to decrease the seek time;

2. The profiles must be achievable by the actuator, considering the power amplifier sat-

uration and its limited bandwidth;

3. The profiles should take advantage of the back $e.m.f.$ effects to help the deceleration;

4. The profiles should be smooth enough not to excite high-frequency suspension resonance modes;

5. The profiles should have no overshoot at the end of a seek;

6. The implementation should not be too complicated, considering the computing power and memory constraints.

3.4.2 Reference Generator

To meet all of the above requirements for the reference profiles, a simple plant model capturing the key characteristics of the real plant in the low frequencies is used as the reference generator. The reference generator reflects the plant in the worst operation conditions during saturation of the power amplifier. In that situation, the assumption to model the power amplifier as a constant gain is invalid, and the overall servo system is dictated by the bandwidth of the VCM admittance transfer function $\frac{1}{Ls+R}$. The back $e.m.f.$ effects are also included in the generator and utilized to decrease the deceleration time. This reference generator provides the desired position profile for seeking, as well as the desired velocity and current profiles for model following control.

The generator is shown in Fig. 3.20. In the continuous-time domain, its state space equations are given as:

$$\dot{\mathbf{x}}_r(t) = A_r \mathbf{x}_r(t) + B_r u_r(t) \tag{3.43}$$

$$\mathbf{x}_r(t) = \begin{bmatrix} y_r(t) & v_r(t) & i_r(t) \end{bmatrix}^T \tag{3.44}$$

$$A_r = \begin{bmatrix} 0 & 1 & 0 \\ 0 & 0 & \frac{K_t}{J} \\ 0 & -\frac{K_{eb}}{L_r} & -\frac{R_r}{L_r} \end{bmatrix} \tag{3.45}$$

$$B_r = \begin{bmatrix} 0 \\ 0 \\ \frac{1}{L_r} \end{bmatrix} \tag{3.46}$$

where $y_r(t)$, $v_r(t)$ and $i_r(t)$ are the desired position, velocity and current, respectively; u_r denotes the control input. In Fig. 3.20, J, K_t, K_{eb}, L_r, and R_r are the moment of inertia of the actuator, the torque constant, the back $e.m.f.$ constant, the coil inductance and the resistance, respectively. L_r and R_r can be different from the real values for the track profile performance tuning. Reference generator with a lower bandwidth of $\frac{1}{L_r s + R_s}$ provides slower position profiles. A reference generator without back $e.m.f.$ is shown in Fig. 3.21.
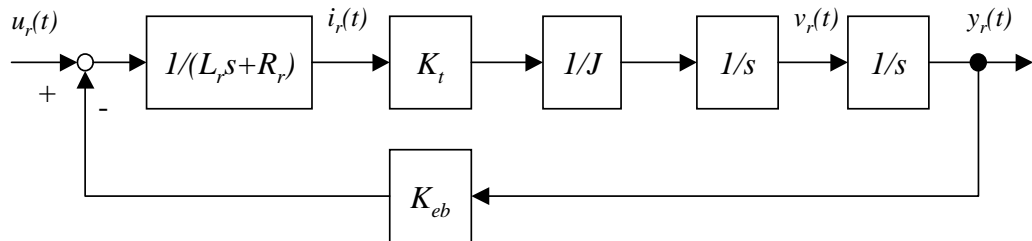
Figure 3.20: Reference generator with back $e.m.f.$
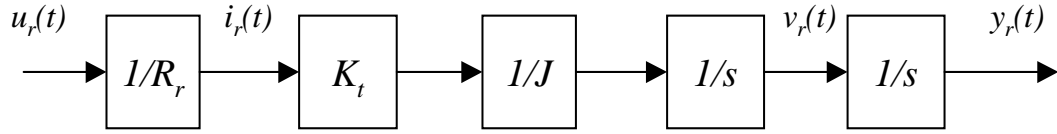
Figure 3.21: Reference generator without back $e.m.f.$

In the design of reference trajectories, the continuous-time model shown in Fig. 3.20 is converted to a normalized zero order hold equivalent. After the normalization, the units of the position, velocity and current are $track$, $tracks/sample$, and the least significant bit (LSB) value of the voltage command before DAC, respectively. The normalized reference generator is given as

$$\mathbf{x}_{rd}(k+1) = A_{rd}\mathbf{x}(k) + B_{rd}u_{rd}(k) \qquad (3.47)$$

where k denotes the discrete-time instance, or the sample number.

Due to the memory constraints of the HDD controller, the reference trajectories are designed in two stages. The first stage is based on off-line simulations, and the second stage uses an on-line reference generator together with a data table saved in the first stage.

3.4.3 Stage One: Off-line Simulations

As pointed out in [52], there is no closed form expression for a voltage-constrained deceleration velocity profile in terms of the remaining head travel distance to the target track center. However, the profile and the reference trajectory can be numerically determined by off-line simulations. The results can be saved in a look-up table used later for
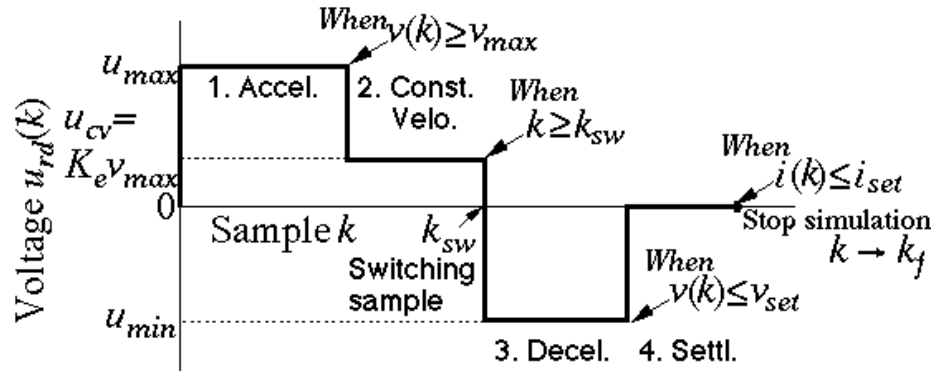
Figure 3.22: Control input to the reference generator in the offline simulations

implementations.

As shown in Fig. 3.22, the reference generator is used in the following procedures to create the look-up table:

1. Apply the maximum input voltage $u_r(k) = u_{\max}$ for acceleration;

2. If the velocity $v_r(k)$ reaches the safety limit v_{coast}, change the voltage to $u_r(k) = K_{eb}v_{coast}$ to maintain the speed;

3. When the sample number k reaches an pre-defined switching sample k_{sw}, apply the minimum input voltage $u_r(k) = u_{\min}$ for deceleration;

4. When the velocity $v_r(k)$ is decelerated to a pre-defined threshold value v_{set}, set $u_r(k) = 0$ and let the current $i_r(k)$ decay at its natural time constant;

5. When the current $i_r(k)$ decays to a pre-defined threshold value, stop the simulation, and save k_{sw} and the final $i_r(k)$, $v_r(k)$, $y_r(k)$ and time t_f;

6. Change k_{sw} in an iteration manner for all meaningful values, and repeat from 1 to 5.

Profiles	Initial boundary conditions	Final boundary conditions
Position	$y_{smart}(0) = 0$	$y_{smart}(t_f) = y_f$
Velocity	$v_{smat}(0) = 0$	$v_{smart}(t_f) = v_f$
Current	$i_{smat}(0) = 0$	$i_{smart}(t_f) = i_f$

Table 3.3: Trajectory boundary conditions to minimize seek-induced vibrations

7. The final position data $y_r(k)$ is saved in a look-up table for on-line reference generation, which will be presented in the next section.

3.4.4 Stage Two: On-line Trajectory Adjustment

SMART (Structural vibration Minimized AcceleRation Trajectory)[47] is obtained by solving an optimal control problem for a double integrator plant. The performance index is given by

$$J_{smart} = \min_{u_{smart}} \int_{t_0}^{t_f} \left[\frac{du_{smart}(t)}{dt} \right]^2 dt \qquad (3.48)$$

where t_f comes from the look-up table obtained in the off-line simulations. By choosing the plant as a double integrator, Equation 3.48 can be solved and the profile with certain boundary conditions can be obtained. For the track seeking, the boundary conditions listed in Table 3.3 must be satisfied. In Table 3.3, the final position y_f, velocity v_f, and current i_f of SMART are calculated using the information in the same look-up obtained in the off-line simulations. y_f is the difference between $y_r(t_f)$ and the seek distance Y_f; $v_f = v_r(t_f)$; and $i_f = i_r(t_f)$.

The SMART profile can be analytically obtained, and the SMART position y_{smart}, velocity y_{smart} and current i_{smart} can be expressed as in Eq. 3.49, 3.50, and 3.51, respectively. For convenience of the implementation, time t is substituted by the discrete sample index k in those equations.

$$
\begin{aligned}
y_{smart}(k) &= \left(6y_f - 3v_f k_f + \frac{a_f}{2}k_f^2\right)\left(\frac{k}{k_f}\right)^5 \\
&\quad + \left(-15y_f + 7v_f k_f - a_f k_f^2\right)\left(\frac{k}{k_f}\right)^4 \\
&\quad + \left(10y_f - 4v_f k_f + \frac{a_f}{2}k_f^2\right)\left(\frac{k}{k_f}\right)^3 \tag{3.49}
\end{aligned}
$$

$$
\begin{aligned}
v_{smart}(k) &= \left(30y_f\frac{1}{k_f} - 15v_f + \frac{5a_f}{2}k_f\right)\left(\frac{k}{k_f}\right)^4 \\
&\quad + \left(-60y_f\frac{1}{k_f} + 28v_f - 4a_f k_f\right)\left(\frac{k}{k_f}\right)^3 \\
&\quad + \left(30y_f\frac{1}{k_f} - 12v_f + \frac{3a_f}{2}k_f\right)\left(\frac{k}{k_f}\right)^2 \tag{3.50}
\end{aligned}
$$

$$
\begin{aligned}
i_{smart}(k) &= \frac{JK_y}{K_t T_s^2}[\left(120y_f\frac{1}{k_f^2} - 60v_f\frac{1}{k_f} + 10a_f\right)\left(\frac{k}{k_f}\right)^3 \\
&\quad + \left(-180y_f\frac{1}{k_f^2} + 84v_f\frac{1}{k_f} - 12a_f\right)\left(\frac{k}{k_f}\right)^2 \\
&\quad + \left(60y_f\frac{1}{k_f^2} - 24v_f\frac{1}{k_f} + 3a_f\right)\left(\frac{k}{k_f}\right)] \tag{3.51}
\end{aligned}
$$

where k_f, K_y, and T_s are the final sample number, one track pitch angle in $rad/track$, and the sampling time in second, respectively. The final current error i_f is converted to the unit

of acceleration errors in $track/sample^2$ by

$$a_f = \frac{K_t T_s^2}{J K_y} i_f \tag{3.52}$$

In the track seeking mode, the controller is first given a specific seeking command: a number of tracks Y. The final position $y_r(t_f)$ closest to Y can be found in the look-up table, as well as the corresponding switching sample k_{sw}, $v_r(t_f)$, $i_r(t_f)$. Using the switching sample information, and the same reference generator in the off-line simulations to generate the profiles on the fly during the track seeking. The profiles contains the same y_r, v_r, and i_r. At time t_f, their values should be equal to those obtained from the look-up table.

By choosing the boundary conditions listed in Table 3.3,

$$y_f = y_r(t_f) - Y \tag{3.53}$$

$$v_f = v_r(t_f) \tag{3.54}$$

$$i_f = i_r(t_f) \tag{3.55}$$

SMART profiles y_{smart}, v_{smart}, and i_{smart} can be generated using Eqs. 3.49, 3.50, and 3.51. The final adjusted profiles are

$$y_{rg} = y_r - y_{smart} \tag{3.56}$$

$$v_{rg} = v_r - v_{smart} \tag{3.57}$$

$$i_{rg} = i_r - i_{smart} \tag{3.58}$$

Note the final value of the profiles are

$$y_{rg}\left(t_f\right) \quad = \quad Y \tag{3.59}$$

$$v_{rg}\left(t_f\right) \quad = \quad 0 \tag{3.60}$$

$$i_{rg}\left(t_f\right) \quad = \quad 0 \tag{3.61}$$

At a finite time t_f, the reference velocity and current are equal to zero simultaneously. At the same time, the reference position reaches the target track center.

In this reference profile generation method, the entire profiles of the position, velocity and current trajectories are adjusted throughout the seeking time, instead of being corrected only at the deceleration or settling time. Because the reference trajectories are dynamically generated by the simple on-line calculations with assistance of a data table, they are easy to implement on typical commercial HDDs within the limited computing power and memory size constraints.

A reference profiles design example for the Fujitsu M2954 drive is shown in Figs. 3.23 and 3.24. Velocity profiles shown in Fig. 3.23 are the off-line simulation results used in three cases: A) 300 track seeking; B) 2000 track seeking; and C) 5000 track seeking. In these simulations, $u_{\max}$ is $9.0V$ and $u_{\min}$ is $-9.0V$ for Case A. $u_{\min}$ is $-8.5V$ for Case B and C. v_{coast}, v_{set}, and i_{set} are set to $37.5 \; tracks/sample$, $5.0 \; tracks/sample$ and $-0.03A$, respectively. Note that the end of these profiles are not zero due to the current influence from the VCM model. Figure 3.24 illustrates the SMART adjustment for the velocity profile. The boundary condition v_f from the off-line simulation results is adjusted by the SMART velocity profile v_{smart} by its superposition to the biased results, resulting in the final velocity profile with a zero value at sample k_f.
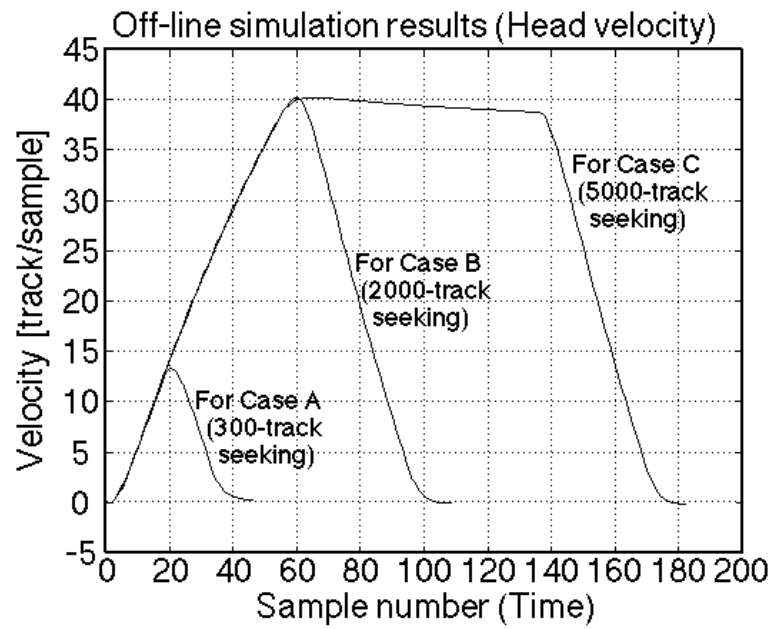
Figure 3.23: Velocity profile obtained from the off-line simulation results
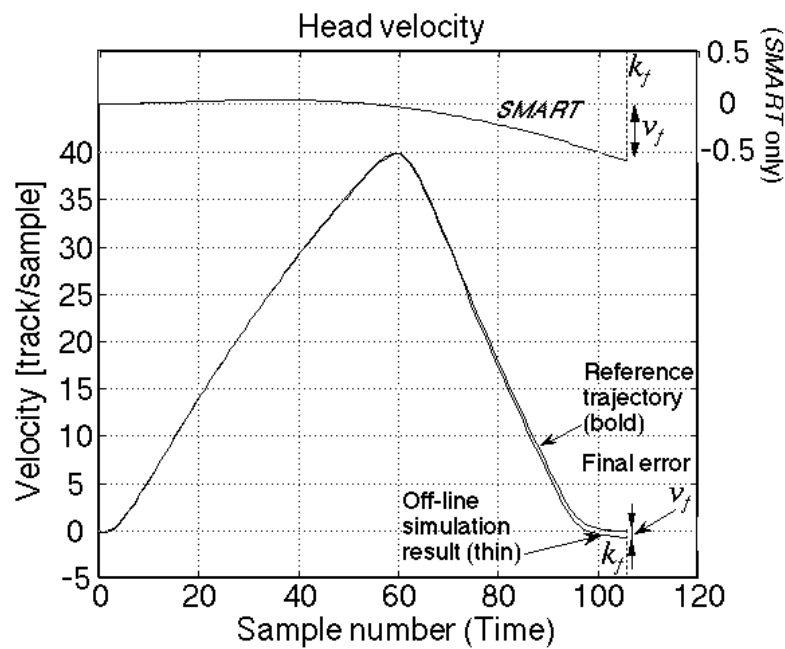
Figure 3.24: SMART adjustment of the velocity reference profile
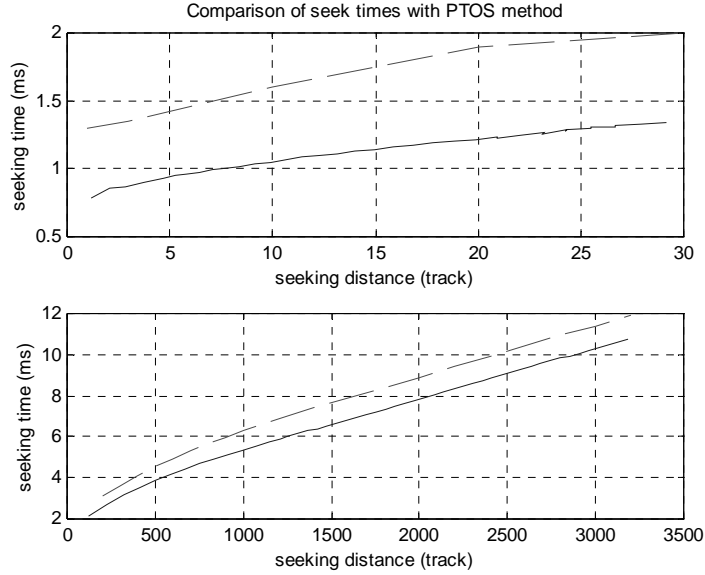
Figure 3.25: Comparison of simulated seek times for the proposed 2DOF control and PTOS, using the NEC drive model.

3.4.5 Simulation Comparisons

Track seeking has been simulated using both the NEC drive model, given Table 3.1, and the Fujitsu M2954 drive model, given in Table 2.1.

For the NEC drive, simple PTOS method and the proposed new reference generation method are compared. The results are shown in Fig. 3.25, in which the dashed lines are the seek time curves over the seek distance for MSC with the conventional PTOS method introduced in Section 3.1.1, and the solid lines are the seek time curves for 2DOF control structure with the new reference generation method. 2DOF control shortens the seeking time by $0.5ms$ to $1.5ms$. In the simulation, the bandwidth of $\frac{1}{L_r s + R_r}$ in the reference generator is set to $1.2kHz$. The maximum voltage $u_{\max}$ is $7.8Volts$.

Simulation comparisons using the Fujitsu M2954 drive are made using three dif-

Tracks	Proposed method (simulation)	PTOS (simulation)
300	5.03	5.65
2000	8.87	10.35
5000	13.98	15.79

Table 3.4: Comparison of seek times of the proposed 2DOF control and PTOS

ferent methods. The first is the proposed reference generation method, the second is the improved PTOS method, and the third is the simple PTOS method. Three cases shown in Fig. 3.23 are simulated and their seeking time are compared in Table 3.4. The seeking end condition is defined as the time when the position error $y \leq 0.5\mu m$ for consecutive 20 servo samples. The results show that the proposed method has a shorter seek time than the other two methods.

More complete comparisons are made by simulations using the proposed method and MSC with the improved PTOS method. The results are given in Fig. 3.26. As seen in the figure, the proposed method improves the seek time by 5% to 15%.

3.5   Summary

In this chapter, two degree of freedom (2DOF) control structure and its three major components are described in detail. The unified 2DOF structure operates for both track seeking and following, therefore making the mode changes in MSC unnecessary, therefore avoiding the its abrupt control input changes and the resulted settling problems. Another major benefit of 2DOF control is that many sophisticated feedforward control algorithms
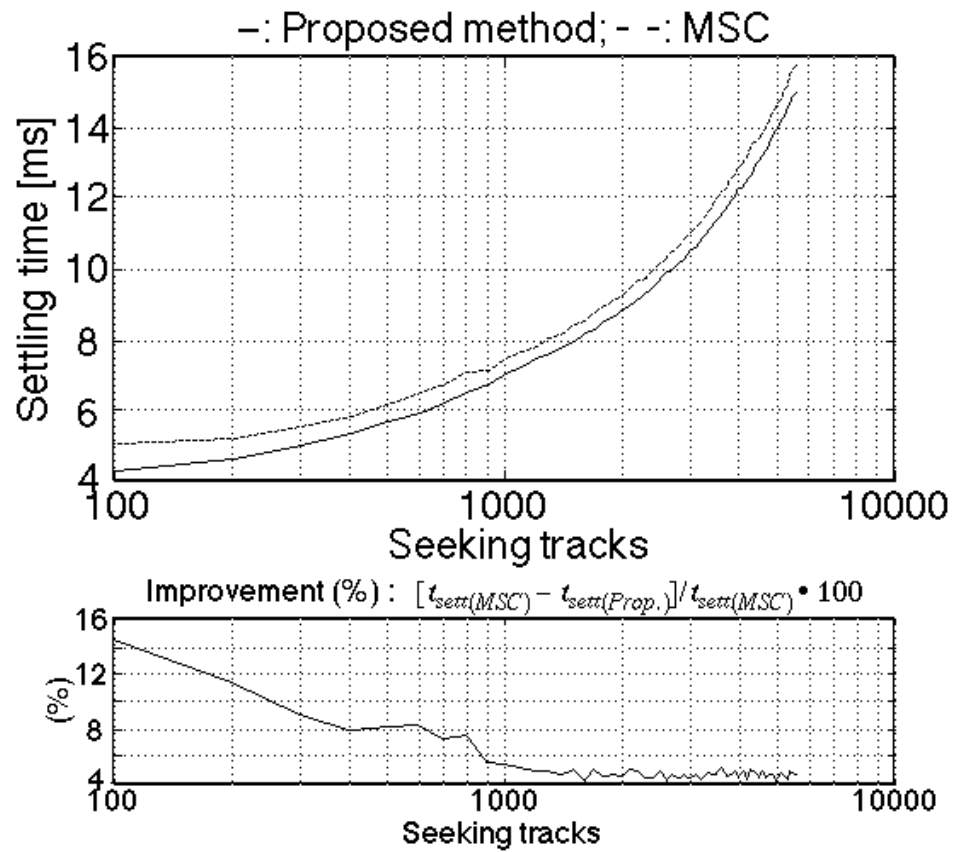
Figure 3.26: Comparison of seek times between the proposed 2DOF control and the improved PTOS, using Fujitsu M2954 model.

can be used together with the robust inner loop feedback controller. DOB and ARC for the inner loop controller were presented and discussed. Their comparisons were made by simulations. The feedforward control algorithms, including zero phase error tracking control and model following control, were described. A new reference generation method was proposed. The 2DOF control structure with the reference profile was shown to perform better than MSC with PTOS. With the use of this new reference generation method, track seeking time can be reduced. The improvement was mostly achieved in the deceleration period due to the use of back $e.m.f.$ effects.

Experimental investigations of 2DOF control and the effectiveness of its components will be presented in the next chapter.

Chapter 4

Applications to Hard Disk Drive

In the year of 2000, the single stage actuator servo is still dominating in the HDD industry. The dual stage actuator servo system, with a PZT or a slider based actuator attached to the suspension, is able to achieve a higher bandwidth and better TMR performance than the single stage actuator servo system. However, it is still in the research and development phase for most HDD companies. Its reliability, system integration cost, and added complexity are among the most concerned issues for its implementation. Although it has been projected that the dual stage servo will be introduced in commercial products for a track density around $40K - 50K\ TPI$, it is still desired that the single stage servo system may also handle such a TPI or even a higher one. Extending the TMR performance of the single stage servo system is critical for sustaining the product road map as well as for the timely introduction of the dual stage servo solutions.

Given a mechanical platform based on a single stage actuator, there are two major issues in improving the TMR performance of its servo system. The first is the selection of

the servo structure; and the second is the optimization of the servo TMR performance for the specific HDD platform.

The 2DOF controller with DOB is implemented for a single stage servo system in this Chapter. Its effectiveness is evaluated by experiments on a Fujitsu M2954 experimental setup. This setup is described in Section 4.1. The effectiveness of the new reference generation and the disturbance observer (DOB) structure is evaluated in Sections 4.2.1 and 4.2.2, respectively. A new RRO compensation technique using the servo burst fields for the feedforward control is introduced in Section 4.3.

For fair PES TMR performance comparisons, different servo structures have to be fully optimized for the same mechanical platform and noise environment, under similar stability and implementation constraints. This issue is addressed in Section 4.4. The optimization is conducted based on the fixed servo structure and the pertinent TMR source models (Section 4.4.2). In Section 4.4.1, the optimization is formulated as a problem of performance index minimization with constraints on the servo stability margins. The index contains the sampled discrete-time domain servo transfer functions, and the corresponding weighting sequences are obtained from the TMR source models. The optimization procedures and results are given for the conventional PID controller and the proposed 2DOF controller in Section 4.4.3. Finally, the chapter is summarized in Section 4.5.

4.1   Experimental Setup

Advantages of the new reference generation method and DOB are demonstrated by experiments on a Fujitsu $4.3GB$ SCSI hard disk (model $M2954$). The same setup was

also used in [26], [73], [25]. Modeling parameters for this drive are given in Table 2.1.

The M2954 drive used in the experiments is a commercial product. A Texas Instrument $TMS320C25$ fixed-point DSP is used to implement its servo system. It was found that there is little room for extra servo functions due to the on chip memory size and the computing power. Existing servo and interface functions left little idle DSP time between servo samples. It was not possible to test the entire 2DOF controller proposed in this drive using its on-board DSP. For example, it takes approximately 100 machine cycles to implement the proposed reference generator, and another 100 machine cycles to implement DOB or ARC. For the drive DSP, 100 machine cycles equal the time of $10\mu s$. Implementing the whole 2DOF controller will use an extra $20\mu s$, which is almost one third of the sampling time $T_s = 67.2\mu s$. Nevertheless, it was found that more than $10\mu s$ but less than $20\mu s$ DSP computing time is still available for extra tasks. Therefore, it is still possible to implement and evaluate the proposed reference generation method and the robust feedback controller separately, or once a time.

4.2   Experiments on Track Seeking Control

Because the 2DOF control structure is an unified servo structure for both track seeking and following modes, the same controller applies to the two modes. The seeking control in 2DOF control is initiated by the reference profile. For track following, the reference is simply zero. In the MSC approach, two different servo controllers work in the two modes, with the transition instance determined by the R/W position and the estimated velocity information. As mentioned before, the mode changes sometimes cause undesired
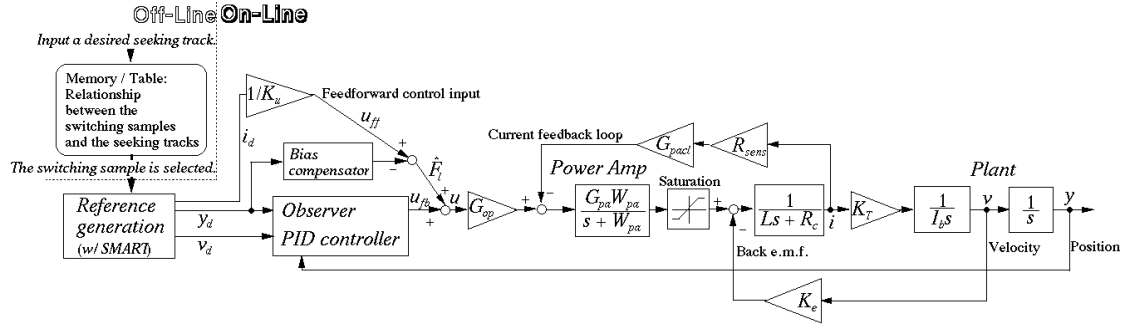
Figure 4.1: Implementaion of the new reference generation method

PES oscillations, which make the settling of the R/W head difficult.

For the track seeking control, 2DOF control and MSC with the improved PTOS method (Chap. 3) are compared experimentally. The Fujitsu $M2954$ is used as the testing platform. As explained before, the new reference generation and the DOB based robust feedback system are implemented and evaluated separately as described in the following two subsections.

4.2.1 Implementation of the New Reference Generation Method

For 2DOF control using the new reference generation method, the overall control system is shown in Fig. 4.1, in which y_d, v_d and i_d are the position, the velocity and the current reference profiles, respectively. The reference profiles are derived using the proposed method described in Section 3.4. The model following feedforward control input u_{ff} is obtained by dividing the reference current i_d by the DC gain K_u of the power amplifier. The observer provides the estimates of the head position and velocity based on the PES measurement and control input u. The gains of the PID controller are chosen to achieve

the open-loop crossover frequency at about 700 Hz. A bias compensator is also used to compensate for the FPC tension disturbances.

For the MSC approach, the improved PTOS method described in Section 3.1.1 is used.

Three cases of track seeking are implemented using both the new reference generation method and the MSC with the improved PTOS method. They are 1) 300 tracks, 2) 2000 tracks, and 3) 5000 tracks seeking. The off-line reference generation is shown in Fig. 3.23. The on-line reference generation is simulated in Section 3.4.5.

For fair comparisons, the same feedback controller is used for both approaches. The experimental results are shown in Figs. 4.2, 4.3, and 4.4. The seek trigger is low when the servo is in the seeking mode, and is high when the seek ends in the following mode. The end of a seek is defined as the time when consecutive 20 samples position signals are within $0.5\mu m$ near the target track center after a seek. It can been seen in these figures that the position is settled without large overshoot in every case, and that the current in the deceleration period has a larger value using the new reference generation method than that using the MSC approach. This is due to the utilization of the back $e.m.f.$ effects, which shorten the seeking period.

The experimental results along with the simulation results in Table 3.4 are summarized in Table 4.1 and Fig. 4.5. The new reference generation method has achieved better seeking performance than MSC with the PTOS and the improved PTOS methods.

Mode switching control method: 300-track seeking

Head position   1/3 track

VCM current   0.6 A

Seeking   (On-track signal)

Time [ms]

Proposed method 300-track seeking

Head position   1/3 track

VCM current   0.6 A

Seeking   (On-track signal)

Time [ms]
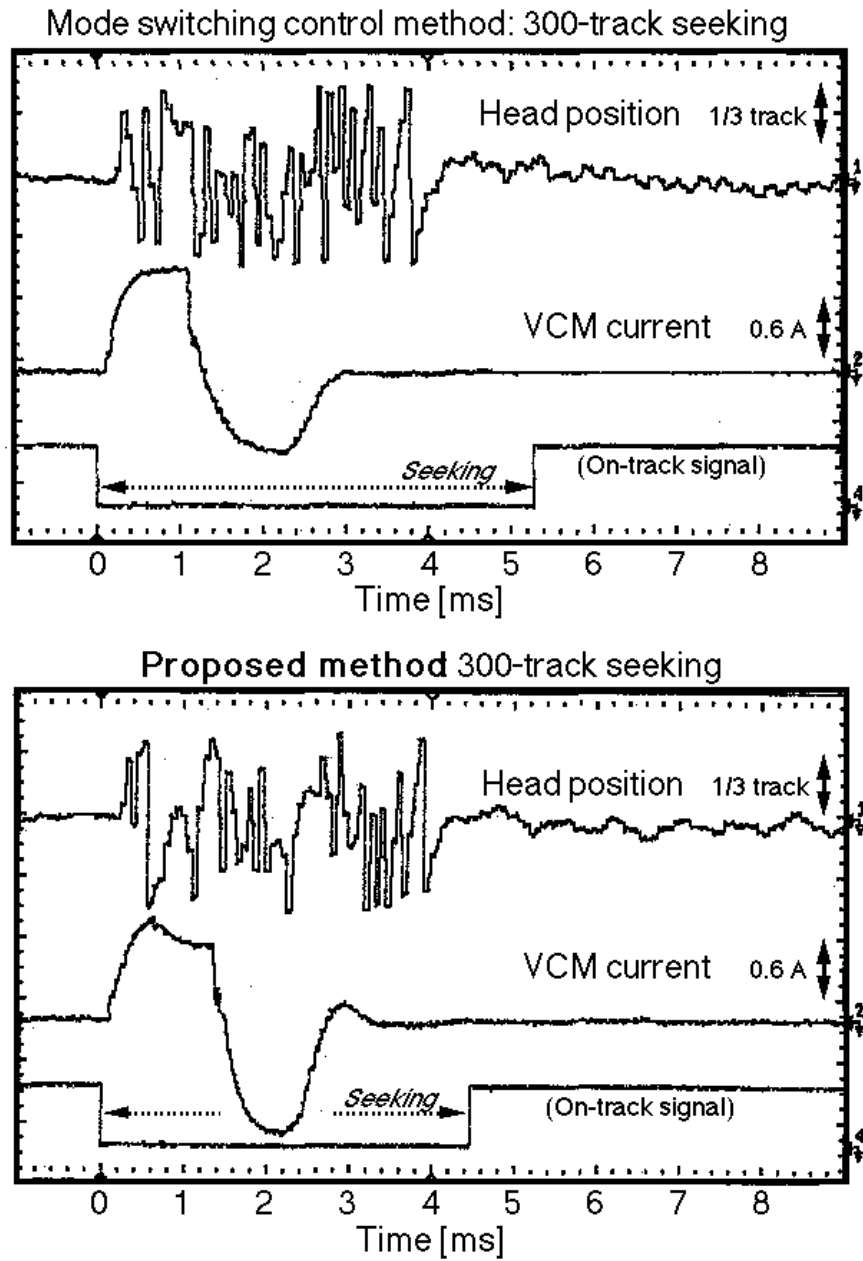
Figure 4.2: 300-track seek comparison
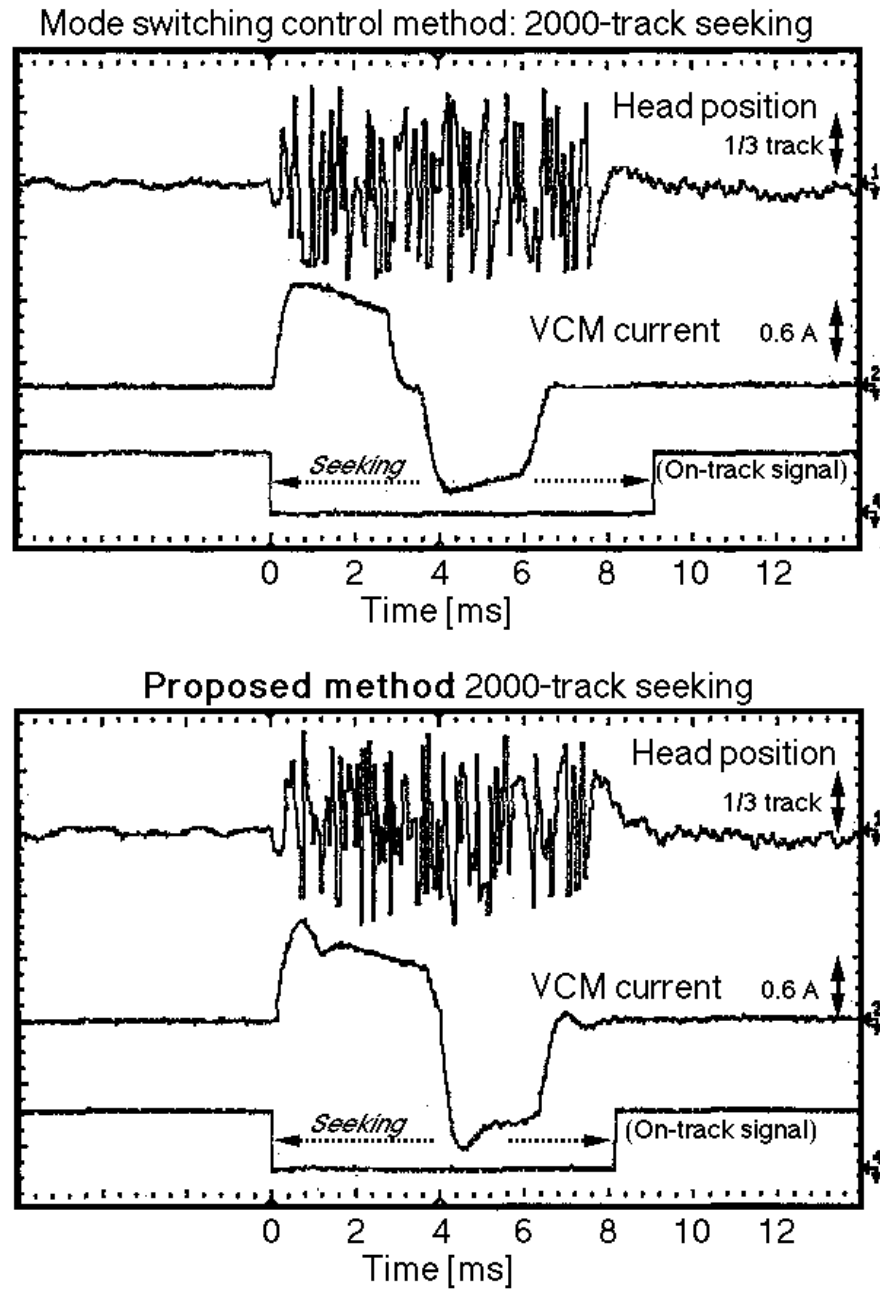
Figure 4.3: 2000-track seek comparison
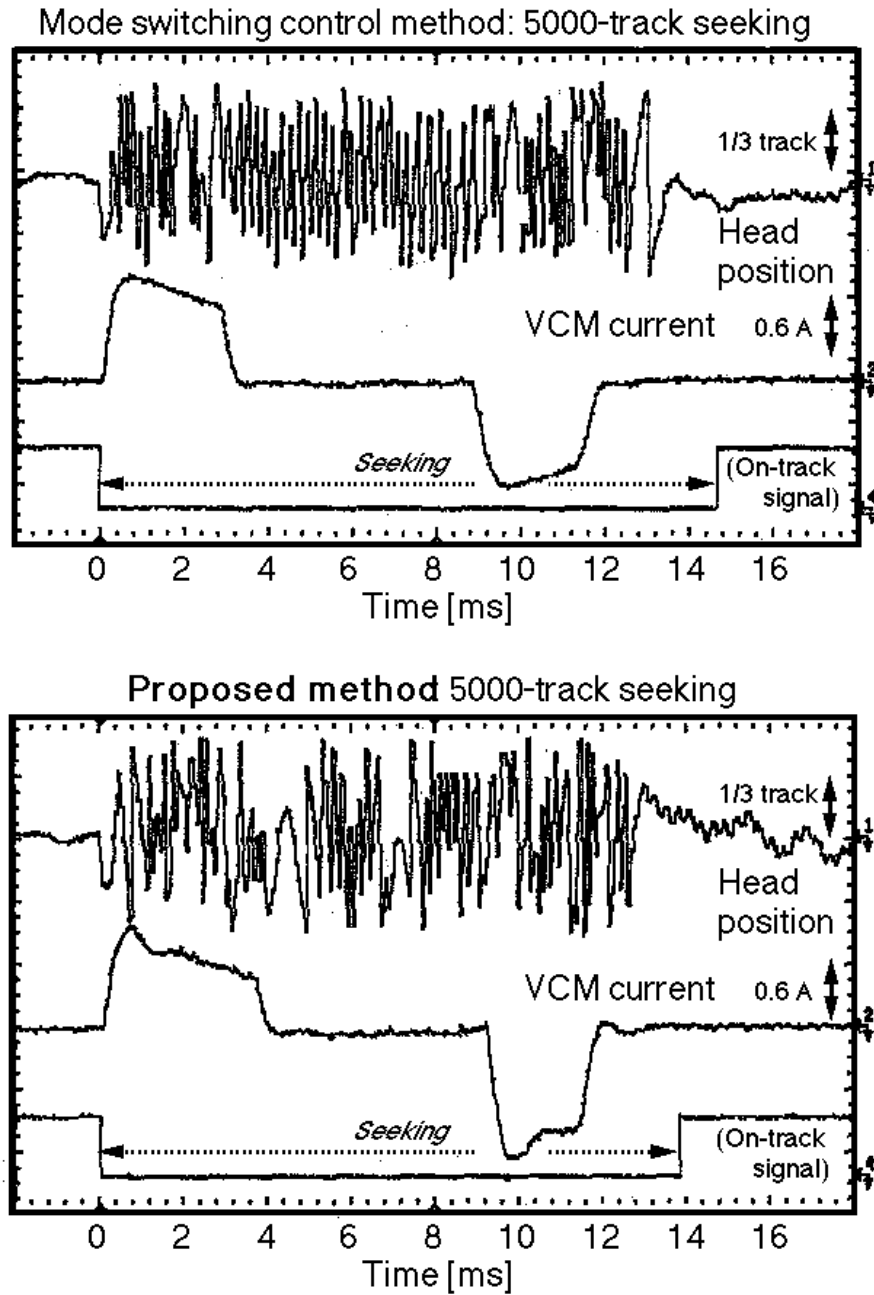
Figure 4.4: 5000-tracks seek comparison

Tracks to seek	Proposed (experiments)	Improve PTOS (experiments)	Proposed (simulations)	PTOS (simulations)
300	5.3	5.6	5.03	5.65
2000	8.9	9.23	8.87	10.35
5000	14.36	14.72	13.98	15.79

Table 4.1: Experimental and simulation comparison of seek times of the proposed 2DOF control and PTOS
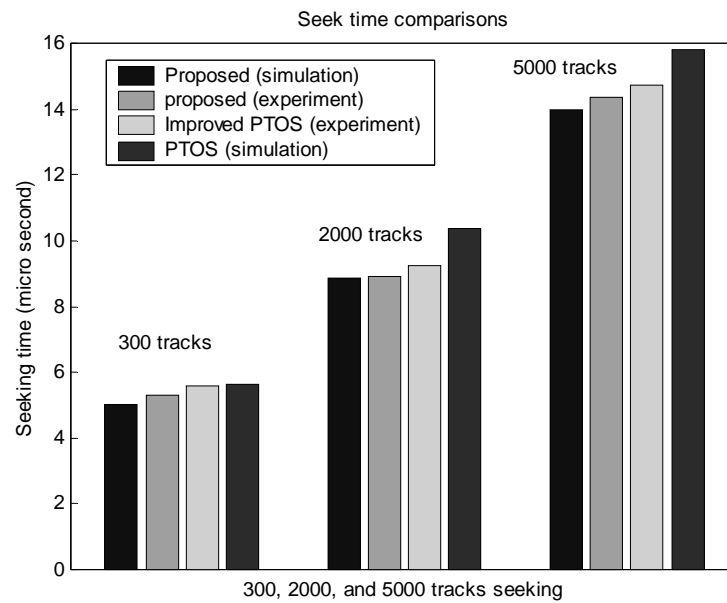
Figure 4.5: Seek time comparisons

4.2.2 Implementation of Disturbance Observer

The effectiveness of the robust inner loop feedback controller DOB for 2DOF structure is also verified by experiment. As mentioned before, it was not possible to simultaneously implement the robust controller and the proposed reference generator. In order to do a fair comparison with the conventional PID controller for the HDD servo, the same simple reference profile is used for both the DOB based servo and the conventional PID servo. Generated using the SMART technique[47], the profile is a fifth order polynomial function of time t, with only three non-zero parameters associated with t^2, t^3, and t^4, respectively. Experimental results are shown in Fig. 4.6, in which the lower plot is for 1800 tracks seek using 2DOF control with DOB, and the upper one is using the conventional PID servo. In both the plots, the first curve is the position error signal, the second one is the current, and the third one is the seek command trigger signal. For the DOB design, a second order low pass digital IIR filter is used as the Q filter, with its bandwidth chosen at $350Hz$.

The experimental results shown in Fig. 4.6 demonstrated that the DOB in 2DOF control structure has achieved smaller tracking errors and faster settling of the R/W head than the conventional PID controller.

4.3 RRO Compensation

As introduced in Chapter 1, repeatable runout (RRO) PES is caused by the servo written-in errors and disk slippage. Its frequency contents are concentrated at the fundamental frequency at the spindle speed and its harmonics. As seen in the PES TMR
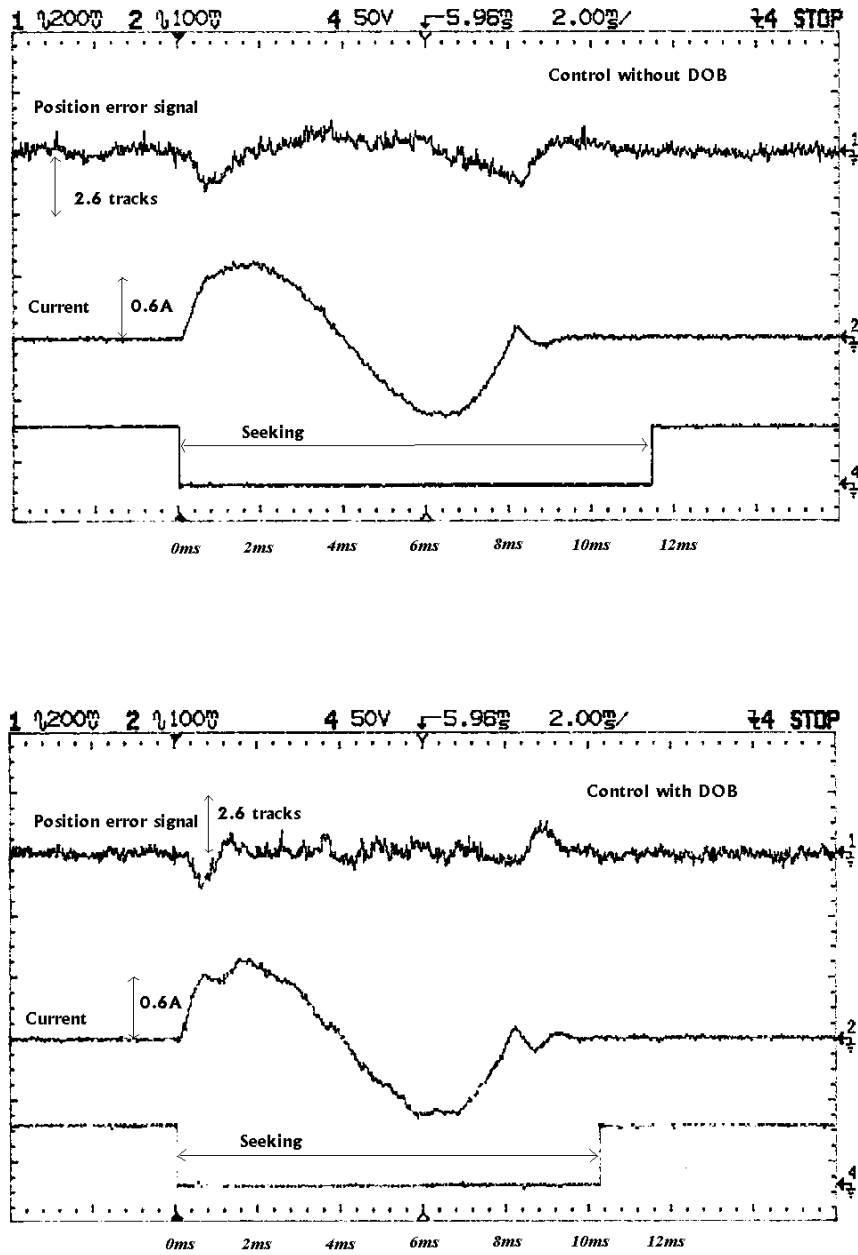
Figure 4.6: Experimental comparisons of 2DOF without DOB and with DOB

sources pie charts in Figs. 2.38 and 2.39, RPES is a major TMR source (43% in variance of the measured PES). In many cases, the RRO components make about half of the PES in variance.

Naturally, the first solution to reduce the RPES should be the action applied to its source: servo written-in errors. This is in fact the most popular approach in practice. For high TPI disk drives, precision improvement of the servo-writers is required. Given the PES TMR budget, there is an associated budget with the servo written-in errors. New or improved servo-writers should meet the new budget requirement. However, it is often costly to purchase or improve servo-writers in quantity for the massive production of hard disk drives. As a result, it is desired to reduce the RPES using improved servo control algorithms. Such a cost-effective approach involves only DSP firmware changes. It also helps extend the life cycles of the expensive servo-writers.

As seen in Fig. 3.10, the integral action and the DOB structure increase the open-loop gains at low frequencies, and can be used to reduce the RPES. If this is not sufficient to meet the TMR budget, additional RRO compensation techniques, such as the repetitive control, must be applied. The repetitive control is briefly introduced in Section 4.3.1, as well as its adverse effects on the hard disk drive applications. A new RRO compensation technique using the servo sector RRO field information is proposed in Section 4.3.2. Simulation results are also presented.

4.3.1 Repetitive Control

The internal model based repetitive control introduces poles at the fundamental frequency and its harmonics of the repetitive disturbances to the servo open-loop transfer

function. In the HDD servo systems, the effects of the disturbances on PES may be examined by the sensitivity function. The repetitive controller reduces the gains of the sensitivity function at the frequencies of the introduced poles, and minimizes the disturbances effects at the repetitive frequencies.

Previous researches have demonstrated the effectiveness of the repetitive control. However, it is still not widely used in the HDD applications, mainly due to its effects on the NRPES and its implementation cost.

1. While the magnitude of the sensitivity function at the RRO frequencies is reduced, it is magnified in-between.

2. The effectiveness of the repetitive controller depends on the time to identify the RPES from the random NRPES. In general, their variance is abut the same, as shown in Fig. 2.38. It usually takes serval revolutions to identify the RPES with an acceptable accuracy. Previous researches have shown the effectiveness of the repetitive controller for HDD in the steady track following mode. However, its transients behavior must also be considered for the implementation. For example, the track to track seek time of the 7200 RPM Fujitsu 2954 drive is 1 ms (The actual value is close, so is for many other commercial HDD). The average latency (the time for half of the disk revolution) and the longest possible latency time (the time for one full disk revolution) is 4.2 ms and 8.4 ms, respectively. It is desired that the R/W head can operate on the data stored on a track immediately after it seeks to the track and waits for the latency time, which has an average of 5.2 ms, or in the worst case, 9.4 ms. It is not acceptable for the servo to take several revolutions to learn the RRO patterns. Moreover, the RRO

patterns are unique for each different track, so it is not possible to learn it once for one track and use the pattern for the other tracks. Therefore, the learning process has to be repeated for each track after the R/W head settles to it, taking the time of several disk revolutions. This approach undermines the efforts to reduce the track seeking time for improving the HDD data transferring rate.

3. Even in the steady following mode, the implementation of the repetitive control for a complete cancellation of the RRO disturbances requires PES at all servo sectors on a track to be stored in the DSP memory. The required number of the DSP memory registers is equal to the sector numbers, which is up to more than a hundred. Compared with a typical PID controller plus notch filters usually taking less than 10 data memory registers to process the PES and generate control input, the repetitive control is much more demanding on the computing hardware.

These adverse effects undermine the effectiveness of the repetitive controllers. This dissertation proposes and evaluates a new method using the servo sector RRO fields for position feedforward control to reduce the RPES. It is described in the following section.

4.3.2   Feedforward Control using Embedded RRO fields in Servo Sectors

Because servo sectors in one track do not generally form a perfect circle, only an irregular pattern is available for the R/W head to follow. However, perfect tracking is not possible due to the dynamics of the servo feedback system, and the noisy environment of the drive operation. As mentioned in the previous section, the irregular pattern is unique for each single track, and learning the pattern through the PES may take several disk

revolutions. These can constrain the implementation of the internal model based repetitive control for HDD during its operation.

It would be desired if the irregular pattern of the servo sectors could be learned and saved within themselves on each track. As seen in Fig. 1.5, the RRO fields in the sectors can be used to store such information. The servo written-in errors can be identified and saved to these fields during the disk drive manufacturing process, or just before its shipment to the market. The RPES identification, dynamic servo written-in errors estimation, and simulation results of the methods are presented below.

RPES Identification

Let $\cdot(m, n)$ denote the value of $\cdot$ at n^{th} servo sample in the mth revolution. $m = 1, 2, .., M$. $n = 1, 2, ..., N_{Sector}$. N_{Sector} is the number of the servo sectors along one track. Assuming $y(m, n)$ as M revolutions of PES observation available for RPES identification, at each sector n, $y(m, n)$ consists of a deterministic value $y_r(m, n)$ plus a Gaussian distribution white noise $y_{nr}(m, n)$, or

$$y(m, n) = y_r(m, n) + y_{nr}(m, n) \tag{4.1}$$

$$y_r(m, n) = C(n) \tag{4.2}$$

where $C(n)$ is a constant array, representing the constant RPES value at the nth sector. The maximum likelihood (ML) estimate of $y_{RRO}(n)$ is the sample mean of the observations:

$$y_{r_e}(n) = \frac{1}{M} \sum_{m=1}^{m=M} y(m, n)$$

$$= C(n) + \frac{1}{M} \sum_{m=1}^{m=M} y_{nr}(m, n) \tag{4.3}$$

The estimation error is

$$y_{re}(n) = \frac{1}{M} \sum_{m=1}^{m=M} y_{nr}(m,n) \tag{4.4}$$

for the nth sector. Based on the assumption that $y_{nr}(m,n)$ is a zero mean, Gaussian, independent distributed white noise with its standard deviation equal to σ_{nr}, the standard deviation of the estimation error $y_{re}(n)$ is given as

$$\sigma_{re}(M) = \frac{\sigma_{nr}}{\sqrt{M}} \tag{4.5}$$

This equation gives a guideline for deciding how many revolutions of PES should be necessary to estimate the PES RRO component.

Simulation results of the RPES estimation using the Fujitsu M2954 drive model are shown in Fig. 4.7. For all the 124 sectors, the estimation errors show a decreasing trend with the increase of the learning revolutions. Figure 4.8 shows the theoretical relationship between the estimation errors, in terms of its standard deviation, and the number of the learning disk revolutions. The relationship was also given in Eq. 4.5.

Dynamic Servo Written-in Errors Estimation

The purpose of the RPES identification is for the reconstruction of its source: servo written-in errors, which affect PES through the servo sensitivity function. To reconstruct the source, the inverse of the sensitivity function $S(z^{-1})$ is used to filter the RPES estimation $y_r(n)$, as given in Eq. 4.3. A proposed dynamic servo written-in errors estimation is

$$y_{TMR\_RRO}(N_{Sector}(m-1)+n) = S^{-1}(z^{-1})\,\hat{y}_r(m,n) \tag{4.6}$$
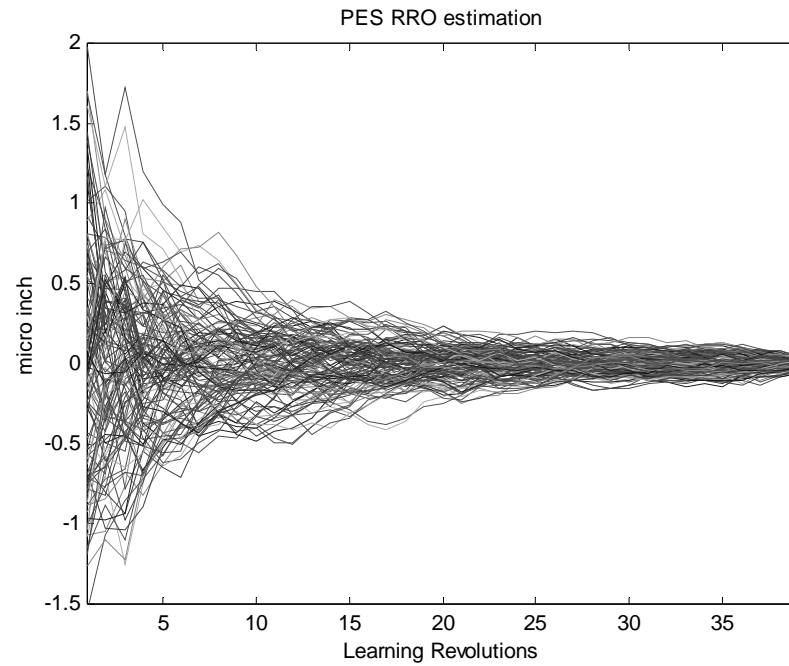
Figure 4.7: RPES estimation errors for all sectors, as a function of the learning revolutions
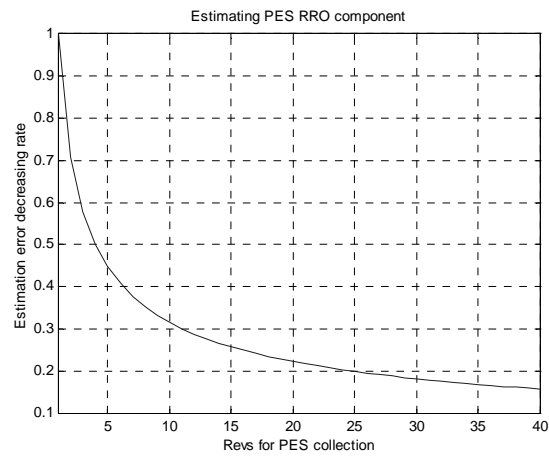
Figure 4.8: RPES estimation error decreases as $\frac{1}{\sqrt{M}}$, where M is the number of the revolutions.

where m is the learning revolution, and $\hat{y}_r(m,n)$ equals to $y_r(n)$ in Eq. 4.3 at the mth learning revolution. In order to shorten the processing time, the reconstruction of the RRO TMR source is performed simultaneously with the estimation of the RPES. Figure 4.9 shows the simulation results of the RRO TMR source dynamic learning process using the Fujitsu M2954 drive model. The initial oscillations of the estimation are caused by the transients of the inverse dynamics of the sensitivity function, as well as the larger estimation errors of the RPES at the initial revolutions. After the transients, the estimation of the servo written-in errors is then saved to their corresponding servo sectors.

When the head reads PES from the servo sector, the written-in error information in the sector is used to adjust the PES. The correction to the burst center mis-alignment is then achieved.

If $S(z^{-1})$ contains unstable zeros or is not strictly proper, it can not be directly inverted. In this case, the zero phase inverse technique discussed in Section 3.3.1 can be used. Time advance z^d introduced in the inversion can first be ignored during the estimation of the written-in errors. When writing the results to the servo sectors, the delays can be taken into consideration by shifting the saving locations of the results.

Simulations

The simulation of the position feedforward control using the servo sector RRO fields are performed using the Fujitsu M2954 drive model. The TMR sources are re-sampled time-domain traces obtained in Section 2.3. For the simulation, at the certain track at OD, the PES RRO $3\sigma = 2.82\ \mu inch$, and PES NRRO $3\sigma = 2.55\ \mu inch$ before the RRO fields
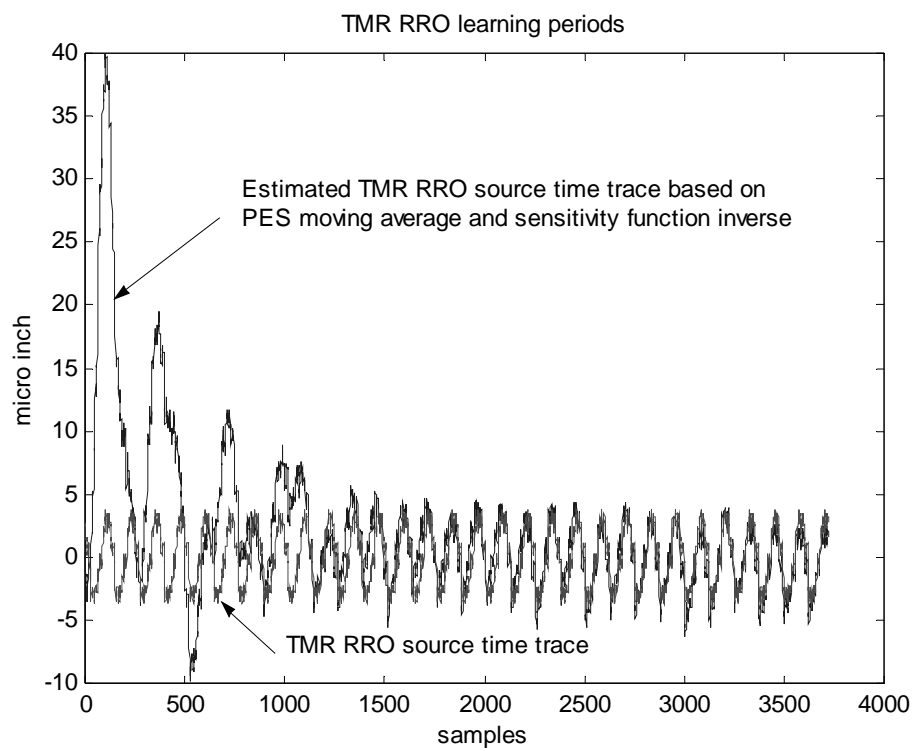
Figure 4.9: Estimating servo written-in errors by filtering the estimated RPES through $S^{-1}\left(z^{-1}\right)$.

position feedforward. The servo written-in errors learning period takes 30 revolutions. At the 31st revolution, or from the sample number at $124*30+1=3721$, the feedforward begins to correct the PES. The RPES $3\sigma = 1.66$ $\mu inch$ and PES $3\sigma = 2.35$ $\mu inch$ after the feedforward. The potential TPI improvement is

$$\frac{\left(\frac{1}{2.35} - \frac{1}{3.04}\right)}{\frac{1}{3.04}} = \frac{3.04}{2.35} - 1 \approx 30\% \tag{4.7}$$
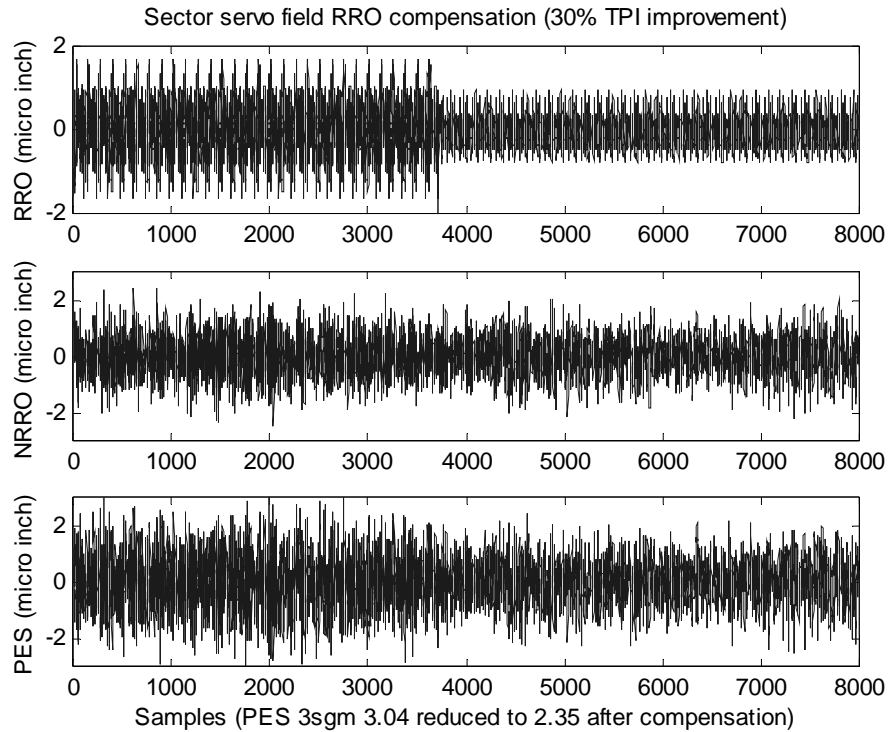
Figure 4.10: Use RRO fields of servo sector to compensate for RRO. Results shown 30% improvement on PES standard deviations.

4.4 Fixed-Structure Servo Optimization

For most commercial disk drive products, real time adaptive controllers have not been well adopted in their servo implementation. HDD servo with a fixed-structure, such

as the typical PID controller with one or more notch filters, is still most popular because of the following:

1. Fixed-structure servo is easier to implement. The relatively simple algorithms make its parameter tuning intuitive and straightforward;

2. Fixed-structure servo can be well modeled as a linear system. The conventional and powerful frequency-domain analysis tools can be used;

3. The uncertainties associated with the plant are not as many as those with the TMR sources. Variations of some major parameters, such as the open-loop gain, can be identified using simple drive calibration techniques. Although the time-domain trace of the random TMR sources convey little meaningful information, their frequency contents have been shown to have strong patterns in Chap. 2. There are still variations of the frequency contents of the TMR sources among different drives, and different zones on the same disk. For example, the power spectrum magnitude and the DFT magnitude of the TMR sources are higher at OD than those at ID. For PES TMR performance requirements, the worst case is always considered.

4. Stability criteria are easier to define in the frequency-domain for a linear fixed-structure servo, using gain margin and phase margin of the open-loop transfer function.

Due to these listed concerns, a linear fixed-structure HDD servo is typically used. Traditionally, the tuning of the controller parameters is based on trial and error, and the success is relied on engineering experience and judgement.

A systematic way to optimize a linear fixed-structure servo is proposed and described in the following sections.

4.4.1 Problem Formulation

Note the PES variance R_y consists of the variance R_{rro} of RPES, R_{sn} of the sensor noise, R_d of the torque disturbances, and R_m of the disk modes and other unaccounted TMR sources, as

$$R_y = R_{rro} + R_{sn} + R_d + R_m \tag{4.8}$$

According to Eq. 2.39,

$$
\begin{aligned}
R_y &= \frac{\sum_{k=1}^{M} F_{rro}^2(k)}{2} + \frac{\sum_{k=1}^{M} F_{sn}^2(k)}{2} + \frac{\sum_{k=1}^{M} F_{d}^2(k)}{2} + \frac{\sum_{k=1}^{M} F_{m}^2(k)}{2} \\
&= \frac{1}{2} \sum_{k=1}^{M} \left(F_{rro}^2(k) + F_{sn}^2(k) + F_{d}^2(k) + F_{m}^2(k) \right) \tag{4.9}
\end{aligned}
$$

where $F_{rro}(k)$, $F_{sn}(k)$, $F_d(k)$, $F_m(k)$ are the normalized DFT magnitude sequence of the RPES, PES contributed by sensor noise, torque disturbances, and the disk mode plus all other TMR sources, respectively. Their relationships with the DFT magnitude of the contributing TMR sources are

$$F_{rro}(k) \;\; = \;\; F_{TMR\_rro}(k) S(k) \tag{4.10}$$

$$F_{sn}(k) \;\; = \;\; F_{TMR\_sn}(k) T(k)$$

$$= \;\; c_{sn} T(k) \tag{4.11}$$

$$F_d(k) \;\; = \;\; F_{TMR\_d} D(k)$$

$$= \;\; c_d D(k) \tag{4.12}$$

$$F_m(k) \;\; = \;\; F_{TMR\_m}(k) S(k) \tag{4.13}$$

where $S(k)$, $T(k)$, $D(k)$ are the frequency sampled magnitude sequence of the sensitivity function, the complementary sensitivity function, and the disturbance transfer function, respectively. $F_{rro}(k)$, $F_{sn}(k)$, $F_d(k)$ and $F_m(k)$ have the same equally spaced frequency sampling intervals. c_{sn} and c_d are the DFT magnitude of the sensor noise and the torque disturbances, respectively. These noises are modeled as white noises, as explained in Chap. 2. Eqs. 4.10 and 4.13 are also illustrated in Figs. 4.11 and 4.12, respectively.

The cost index for the servo TMR performance optimization is chosen as

$$J = \min_{C} \sigma_y^2 = \min_{C} R_y \tag{4.14}$$

where R_y is the PES variance calculated from the frequency-domain:

$$R_y = \frac{1}{2} \sum_{k=1}^{M} \left(\left(F_{TMR\_rro}^2(k) + F_{TMR\_m}^2(k) \right) S^2(k) + c_{sn}^2 T^2(k) + c_d^2 D^2(k) \right) \tag{4.15}$$

and C is the stabilizing servo controller with the required stability margins.

The servo TMR optimization problem has been transformed into a numerical minimization problem with some constraints. The objective is then to minimize the cost index
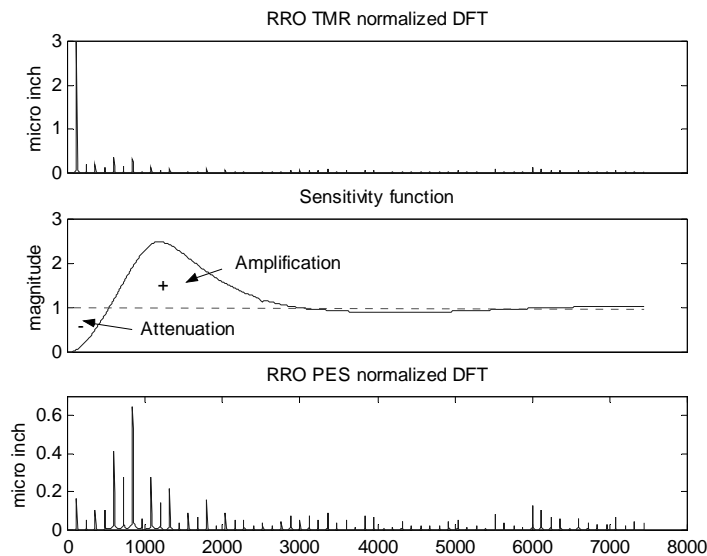
Figure 4.11: Servo written-in errors affect PES through the sensitivity transfer function. They are attenuated at low frequencies, but amplified at certain other middle frequencies due to the Bode theorem effect.
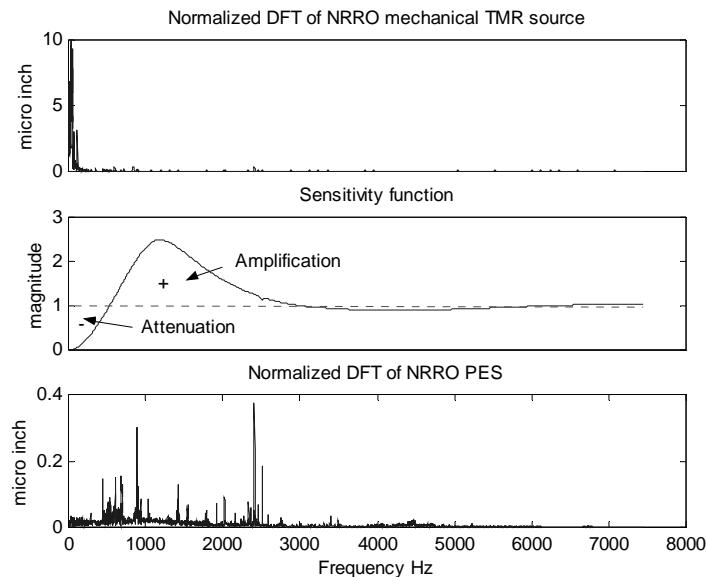
Figure 4.12: NRRO TMR sources also affect PES through the sensitivity function. They are attenuated at low frequencies, but amplified at some middle frequencies..

function J by varying a stabilizing servo controller C. The cost function itself has an intuitive physical meaning: the variance of the PES calculated from the DFT domain. For a fixed-structure servo controller C, its parameters are the tuning factors. DFT of the TMR sources have been naturally used as the weighting sequences associated with the frequency samples of the servo sensitivity function, the complementary sensitivity function and the disturbance transfer function. Using the worst case at OD, these weighting sequences obtained from the TMR sources are fixed and also have intuitive physical meanings related to the power spectrums of the TMR sources. Unlike the common practice in H_∞ optimal control, in which the noise models are approximated using linear models, the DFT magnitude of the TMR noises are directly used as the weighting sequences. For H_∞ optimal control, the order of the linear weighting models is added to the final controller. For the servo written-in errors and the disk modes, it is almost impossible to approximate their power spectrum accurately using low order linear models. The proposed optimization method has the advantage that the final controller structure is fixed and not affected by the weighting sequences.

The optimization is performed directly in the discrete-time-domain. The optimized digital servo controller is immediately ready to use. There are no modeling errors introduced from the continuous to discrete conversion. It is also easy to obtain all the sequences used to construct the cost function J in Eq. 4.14. Note that the stability margins should always be satisfied during the optimization. For the servo asymptotic tracking requirement, an integral action, or a disturbance observer should be used.

4.4.2   Weighting Sequences

As described in Eq. 4.14, the cost function J uses the DFT magnitude of the servo written-in errors, the sensor noise, torque disturbances, and the disk modes plus other TMR sources. The methods to identify and construct them are presented in Chap. 2, in which a commercial drive (see Table 2.3) is used for the illustration purpose. Time domain traces and DFT magnitude of these TMR sources are obtained for the PES and the nominal model of the drive servo system.

For the TMR performance optimization of the M2954 drive servo, the TMR sources of the drive should be first identified so that their DFT magnitude can be obtained and used as the weighting sequences in the cost function given in Eq. 4.14. However, it was not possible to obtain the PES information in the digital format from the Fujitsu M2954 drive using the current available experimental setup and equipment. The available PES information is the analog output from an on-board DAC. Without the servo sector index output synchronizing the PES reading, TMR sources identification methods described in Chap. 2 can not be used.

In order to evaluate and compare different control algorithms for the Fujitsu $M2954$ drive, the same TMR source models and weighting sequences should be used. In this case, the TMR source models obtained of the commercial drive described in Table 2.3 are used for servo optimizations for the Fujitsu $M2954$ drive. Because their spindle speeds and the sampling rates are different, the TMR source models used for the $M2954$ drive are derived from the re-sampled time domain sequences of the available TMR sources. The re-sampled time-domain sequences of servo written-in errors are given in Fig. 4.13. OD, MD and ID

are shown. Their DFT magnitude plots are shown in Fig. 4.14. The standard deviation and the DFT magnitude of the torque disturbances and sensor noise are constants and can be obtained using Eq. 2.42. The DFT magnitude of the re-sampled time trace of the disk modes and other TMR sources at OD are shown in the first plot in Fig. 4.12.

The worst case happened at OD is used to construct the weighting sequences for the TMR optimizations of the $M2954$ drive servo systems.
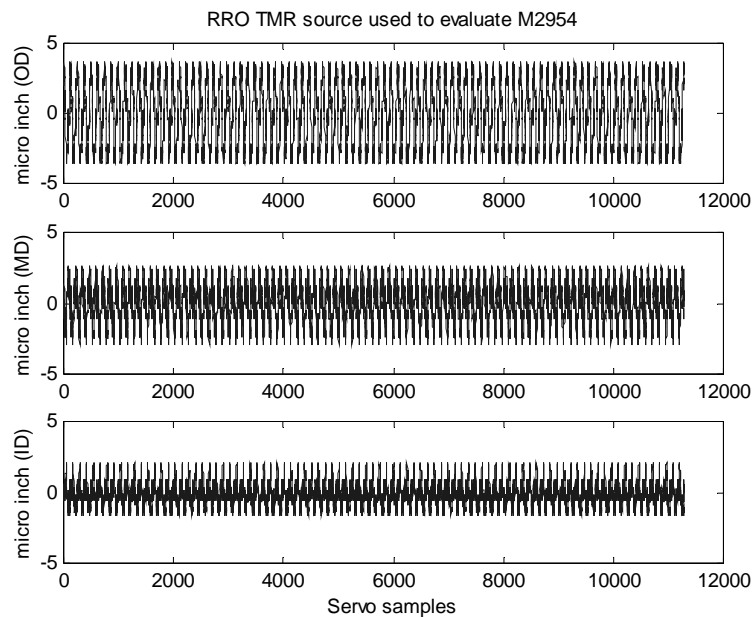
Figure 4.13: Time traces of servo written-in errors.

4.4.3   Procedures and Simulation Results

There are two equally important factors in designing the HDD following servo controllers. One is the selection of its structure, and the other is the selection of the parameters in the fixed-structure controller to meet the TMR and stability requirements.
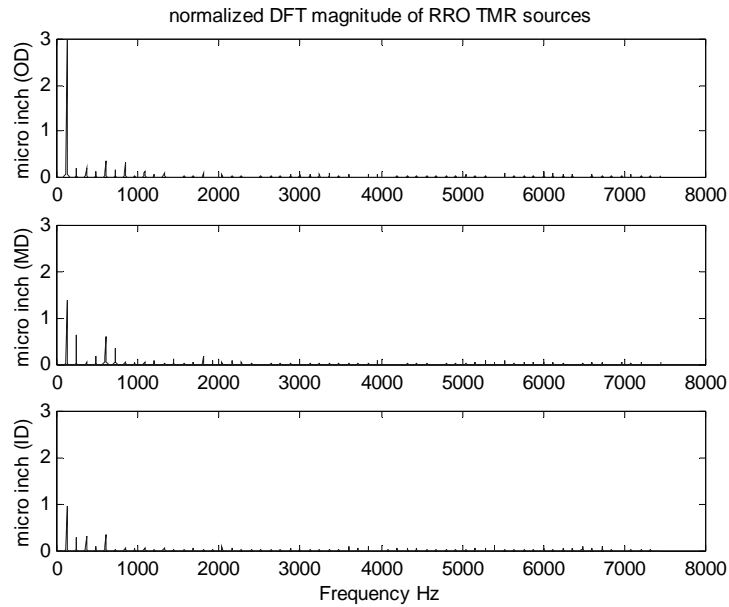
Figure 4.14: DFT of the servo written-in errors.

Therefore, before any controller optimization, its structure has to be carefully chosen and studied. The frequency responses of the nominal PID, a PD, and two DOB based controllers plus a notch filter for the Fujitsu $M2954$ drive are shown in Fig. 3.10. As described in Chap. 2, the PD controller does not provide the asymptotic tracking ability, therefore it can not be used alone as the following servo controller. However, the DOB based controllers with the PD controller in the position loop have such tracking abilities.

In this section, two servo controllers for the Fujitsu M2954 drive are studied and used for the TMR optimization. One is the nominal PID controller with a notch filter; the other is the proposed 2DOF servo controller with a DOB structure in the inner feedback loop and a PD controller in the position feedback loop.

Another purpose of the study is to further compare these two servo controllers.

Although the experimental results in Section 4.2.2 have shown the advantage of the DOB based servo, it was not certain that the DOB based servo and the original servo are all optimized for the PES TMR performance. Only when these two controllers are fully optimized can the comparison results based on TMR performance validly support the argument that the DOB based servo outperforms the original PID servo.

Given these two fixed servo structures, the optimization problem formulated by Eq. 4.14 is to search the parameter sets to minimize the cost function J. Although this can be treated as a pure mathematical optimization problem, investigation and physical intuitions of the servo system can help achieve the parameter optimization more efficiently.

PID Controller Parameter Set for TMR Optimization

Similar to that given in Eq. 2.18, the nominal PID controller is

$$C_{PID}(z^{-1}) = K_p + K_d \left(1 - z^{-1}\right) + \frac{K_i}{1 - z^{-1}} \tag{4.16}$$

which can be re-written as

$$
\begin{aligned}
C_{PID}\left(z^{-1}\right) &= K_p + K_d - K_d z^{-1} + \frac{K_i}{1 - z^{-1}} & (4.17) \\
&= (K_p + K_d)\left(1 - \frac{K_d}{K_p + K_d}z^{-1}\right) + \frac{K_i}{1 - z^{-1}} & (4.18) \\
&= K_l\left(1 - az^{-1}\right) + \frac{K_i}{1 - z^{-1}} & (4.19)
\end{aligned}
$$

where

$$
\begin{aligned}
K_l &= K_p + K_d & (4.20) \\
a &= \frac{K_d}{K_p + K_d} & (4.21)
\end{aligned}
$$

For the nominal controller, K_p, K_d, and K_i are given in Table 2.2. The reason to express the PID controller in Eq. 4.16 as in Eq. 4.19 is because that the two parts in Eq. 4.19 have separate effects on the low and high frequencies. It can be seen from Fig. 4.15 that the integral term (I term) $\frac{K_i}{1-z^{-1}}$ dominates $C_{PID}\left(z^{-1}\right)$ below $500\ Hz$, and the PD term $K_l\left(1-az^{-1}\right)$ is dominating at higher frequencies. Figure 4.16 also shows the open-loop transfer function with the I term and without it. The PD term $K_l\left(1-az^{-1}\right)$ affects the stability margins, while the I term $\frac{K_i}{1-z^{-1}}$ affects the low frequency attenuation abilities.
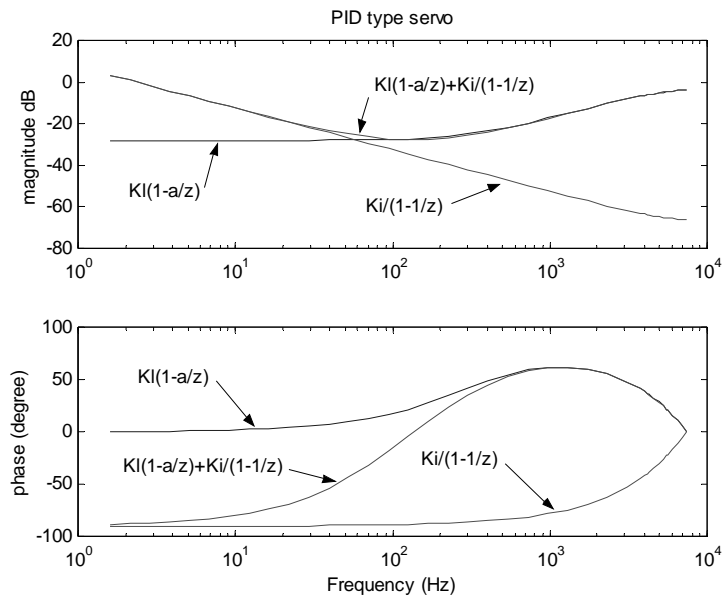
Figure 4.15: Bode diagrams of the PID controller.

The following well known qualitive properties can be quantified through the analysis of the PID controller:

1. the PD term $K_l\left(1-az^{-1}\right)$ is used to lift the phase of the plant, and to achieve the required stability margins. The shape of the open-loop transfer function at the
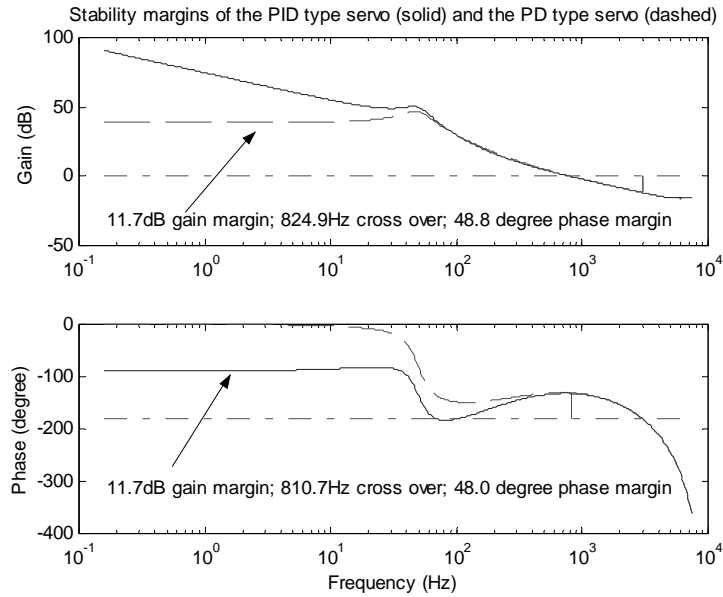
Figure 4.16: The integral control has little effect on the stability margins.

crossover frequency, which is usually above $500\ Hz$, is therefore dominated by the PD term $K_l \left(1 - az^{-1}\right)$.

2. the I term $\frac{K_i}{1 - z^{-1}}$ dominates the PID controller $C_{PID}\left(z^{-1}\right)$ at low frequencies. It is used to raise the gains of the open-loop transfer function for higher attenuation of the low frequency noises, pivot friction torque, and asymptotic tracking ability of the servo.

To further investigate the effects of the PD term to the overall servo system, the Bode diagrams of $\left(1 - az^{-1}\right)$ are shown in Fig. 4.17, in which their phase and magnitude determined by the parameter a are plotted. As a increases from 0 to 1, $\left(1 - az^{-1}\right)$ lifts more and more phase, and raises its gain at high frequencies. Denoting f_m in Hz as the frequency where the filter achieves the maximum phase, its normalized frequency θ_m (with

FIR filter (1-a/z) frequency response (with a = .2, .375, .55, .725, .9)

as 'a' increases

as 'a' increases
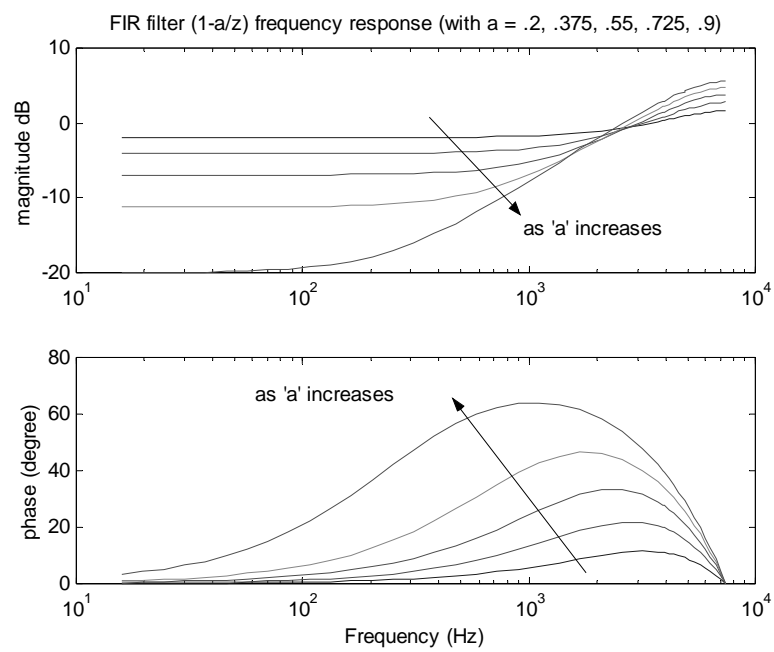
Figure 4.17: Frequency response of the PD filter (1-a/z)

the Nyquist frequency equal to π) is

$$\theta_m = \frac{2\pi f_m}{F_s} \tag{4.22}$$

where F_s is the sampling frequency in Hz. Suppose the frequency ω is in rad/s and the

sampling time $T_s = \frac{1}{F_s}$, by defining $\theta = \omega T_s$

$$1 - az^{-1} = 1 - ae^{-j\theta} \tag{4.23}$$

$$= 1 - a\cos\theta + aj\sin\theta \tag{4.24}$$

The phase Φ of $\left(1 - az^{-1}\right)$ is related to frequency θ in $radian$ by

$$\tan\Phi = \frac{a\sin\theta}{1 - a\cos\theta} \tag{4.25}$$

The following equation holds true at θ_m

$$\frac{d\tan\Phi}{\theta}\big|_{\theta_m} = 0 \tag{4.26}$$

Because

$$\frac{d\tan\Phi}{\theta} = \frac{d}{d\theta}\left(\frac{a\sin\theta}{1 - a\cos\theta}\right)$$
$$= \frac{a\cos\theta - a^2}{\left(1 - \cos\theta\right)^2} \tag{4.27}$$

it can be solved from Eqs. 4.26 and 4.27 that

$$\theta_m = \cos^{-1}(a)\,,\ \text{where}\ a \in [0, 1] \tag{4.28}$$

and the maximum phase which can be achieved is

$$\Phi_m = \tan^{-1}\left(\frac{a}{\sqrt{1 - a^2}}\right)$$
$$= \sin^{-1}(a) \tag{4.29}$$

Eqs. 4.28 and 4.29 can be used to determine where the PD term $K_l \left(1 - a^{-1}\right)$ achieves the maximum phase Φ_m and the value of Φ_m. K_l only affects the magnitude of the controller in the frequency-domain, and does not affect the phase.

According to Eqs. 4.20 and 4.21, a and K_l are uniquely determined by K_p and K_d. Therefore, K_l, a, and K_i, instead of K_p, K_d, and K_i, can be used as the parameter optimization set for TMR performance. The advantage is the better intuition associated with the new set in the frequency-domain. K_l affects the magnitude of the controller, and a determines the controller shape and phase at high frequencies (normally above $500\ Hz$); K_i only affects the controller at low frequencies (normally below $500\ Hz$), and has little effects on the stability margins.

To make the optimization process and results even more intuitive and presentable, we can further convert the parameter optimization set to the open-loop crossover frequency f_{co} in Hz, a, and K_i. Given the fixed plant model $G_p\left(z^{-1}\right)$, at the open-loop crossover frequency $\omega_{fo} = 2\pi f_{co}$ in rad/s,

$$\left| G_p \left(e^{-j\omega_{co}T_s} \right) C_{PID} \left(e^{-j\omega_{co}T_s} \right) C_{notch} \left(e^{-j\omega_{co}T_s} \right) \right| = 1 \tag{4.30}$$

therefore

$$\left| \frac{K_i}{1 - e^{-j\omega_{co}T_s}} + K_l \left(1 + ae^{-j\omega_{co}T_s} \right) \right| = \left| C_{notch} \left(e^{-j\omega_{co}T_s} \right) G_p \left(e^{-j\omega_{co}T_s} \right) \right|^{-1} \tag{4.31}$$

Note the right hand of the Eq. 4.31 is constant. Given fixed a, K_i, and f_{co}, K_l can be uniquely determined. If $\frac{K_i}{1 - e^{-j\omega_{co}T_s}}$ and $\left(1 + ae^{-j\omega_{co}T_s} \right)$ are fixed complex variables, Equation 4.31 can be expressed as:

$$\left|\bar{I} + K_l \bar{D}\right| = K \tag{4.32}$$

where $K = \left|C_{notch}\left(e^{-j\omega_{co}T_s}\right) G_p\left(e^{-j\omega_{co}T_s}\right)\right|^{-1}$, $\bar{I} = \frac{K_i}{1-e^{-j\omega_{co}T_s}} = I_r + jI_m$, $\bar{D} = 1 + ae^{-j\omega_{co}T_s} = D_r + jD_m$. Because

$$\left|\bar{I} + K_l \bar{D}\right|^2 = \left(D_r^2 + D_m^2\right) K_l^2 + 2\left(I_r D_r + I_m D_m\right) K_l + I_r^2 + I_m^2 = K^2 \tag{4.33}$$

K_l can be determined from

$$\left|\bar{D}\right|^2 K_l^2 + 2\left(I_r D_r + I_m D_m\right) K_l + \left|\bar{I}\right|^2 - K^2 = 0 \tag{4.34}$$

The above analysis proves that K_l can be uniquely determined by f_{co}, K_i, and a, if the notch filter $C_{notch}\left(z^{-1}\right)$ is fixed. Therefore, the parameter optimization set of the PID controller can be converted to f_{co}, a, and K_i. This gives intuitive meanings to servo engineers in the disk drive industry, where the servo open-loop crossover frequency f_{co} is quoted as the "bandwidth" of the system and used as one of the major servo performance criteria. With f_{co} being fixed, a determines the shape of the controller and affects both gain and phase margins. K_i is still dominating the low frequency performance as described before.

Disturbance Observer Based Servo Parameter Set for TMR Optimization

For the disturbance observer based controller described in Chap 3, a PD controller is used in the position loop. It is

$$C_{PD}\left(z^{-1}\right) = K_p + K_d - K_d z^{-1} \tag{4.35}$$

$$= K_l\left(1 - az^{-1}\right) \tag{4.36}$$

Same as in Eqs. 4.20 and 4.21, K_l and a are determined by K_p and K_d. As described in Eq. 3.14, the overall controller for the servo (except the same notch filter used in the PID control) is

$$C_{DOB+PD}\left(z^{-1}\right) = \frac{Q\left(z^{-1}\right)G_{pi}\left(z^{-1}\right) + C_{PD}\left(z^{-1}\right)}{1 - z^{-d}Q\left(z^{-1}\right)} \tag{4.37}$$

where $Q\left(z^{-1}\right)$ is the discretized version of $Q\left(s\right)$ given in Eq. 3.33. The only parameter to tune for the DOB structure is its time constant τ; $G_{pi}\left(z^{-1}\right)$ is the inverse of the nominal plant. Anatomy of the controller in the frequency-domain is shown in Fig. 4.18, in which the frequency responses of the two components of $C_{DOB+PD}\left(z^{-1}\right)$: $\frac{Q\left(z^{-1}\right)G_{pi}\left(z^{-1}\right)}{1-z^{-d}Q\left(z^{-1}\right)}$ and $\frac{C_{PD}\left(z^{-1}\right)}{1-z^{-d}Q\left(z^{-1}\right)}$ are plotted as Curves 1 and 2, respectively. The frequency responses of their summation $C_{DOB+PD}\left(z^{-1}\right)$ is plotted as Curve 3. Curve 2 and 3 are almost overlapped. Curve 1 $\left(\frac{Q\left(z^{-1}\right)G_{pi}\left(z^{-1}\right)}{1-z^{-d}Q\left(z^{-1}\right)}\right)$ has significantly smaller gain, and therefore has little effects when added to the Curve 2 $\left(\frac{C_{PD}\left(z^{-1}\right)}{1-z^{-d}Q\left(z^{-1}\right)}\right)$. Further insights can be obtained by breaking Curve 2 into two multiplicative parts: $C_{PD}\left(z^{-1}\right) = K_l\left(1 - a^{-1}\right)$ and $\frac{1}{1-z^{-d}Q\left(z^{-1}\right)}$, whose frequency responses are plotted as Curve 4 and 5, respectively. As described in Chap. 3 and shown in Fig. 4.18, Curve 5 $\left(\frac{1}{1-z^{-d}Q\left(z^{-1}\right)}\right)$ approximates to 1 as the magnitude of $Q\left(z^{-1}\right)$ rolls off at higher frequencies (above $200\,Hz$). As a result, the product of Curve 4 and 5 is determined by the PD controller $C_{PD}\left(z^{-1}\right)$. $Q\left(z^{-1}\right)$ approximates to 0 with decreasing frequencies, resulting in the high gains of Curve 5 $\left(\frac{1}{1-z^{-d}Q\left(z^{-1}\right)}\right)$ at low frequencies. The product of Curve 4 and 5 is the Curve 2 $\left(\frac{C_{PD}\left(z^{-1}\right)}{1-z^{-d}Q\left(z^{-1}\right)}\right)$..

From the above analysis, we can conclude that for the DOB+PD controller,

1. $C_{PD}\left(z^{-1}\right)$ determines the controller shape at high frequencies above $200\,Hz$, therefore
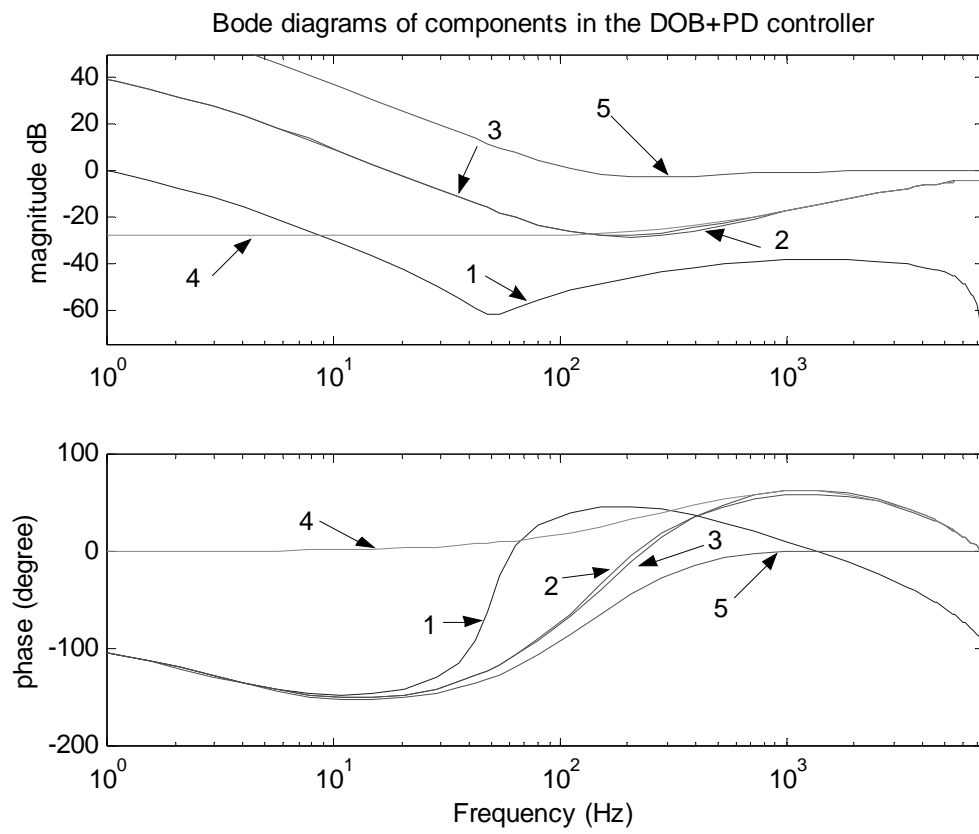
Figure 4.18: Bode diagrams of the components in the DOB+PD controller.

determines the phase and gain margin of the servo system;

2. The $Q\left(z^{-1}\right)$ filter in the DOB structure determines the low frequency shape of the controller. It has little effects on the stability margins;

3. Because the only parameter in the Q filter design is its time constant τ, the parameter set for PES TMR performance optimization can be chosen as τ, K_l, and a.

At the crossover frequency $\omega_{co} = 2\pi f_{co}$

$$\left|G_p\left(e^{-j\omega_{co}T_s}\right) C_{DOB+PD}\left(e^{-j\omega_{co}T_s}\right) C_{notch}\left(e^{-j\omega_{co}T_s}\right)\right| = 1 \qquad (4.38)$$

from Eqs. 4.36 and 4.37,

$$
\begin{aligned}
&\left|\frac{Q\left(e^{-j\omega_{co}T_s}\right) G_{pi}\left(e^{-j\omega_{co}T_s}\right) + K_l\left(1 - ae^{-j\omega_{co}T_s}\right)}{1 - e^{-jd\omega_{co}T_s} Q\left(e^{-j\omega_{co}T_s}\right)}\right| \\
&= \left|C_{notch}\left(e^{-j\omega_{co}T_s}\right) G_p\left(e^{-j\omega_{co}T_s}\right)\right|^{-1}
\end{aligned}
\qquad (4.39)
$$

therefore

$$
\begin{aligned}
&\left|Q\left(e^{-j\omega_{co}T_s}\right) G_{pi}\left(e^{-j\omega_{co}T_s}\right) + K_l\left(1 - ae^{-j\omega_{co}T_s}\right)\right| \\
&= \left|C_{notch}\left(e^{-j\omega_{co}T_s}\right) G_p\left(e^{-j\omega_{co}T_s}\right) \left(1 - e^{-jd\omega_{co}T_s} Q\left(e^{-j\omega_{co}T_s}\right)\right)\right|^{-1}
\end{aligned}
\qquad (4.40)
$$

Given fixed τ, f_{co} and a, Equation 4.40 can be written as Eq. 4.32, in which

$$\bar{I} = Q\left(e^{-j\omega_{co}T_s}\right) G_{pi}\left(e^{-j\omega_{co}T_s}\right) \qquad (4.41)$$

$$\bar{D} = \left(1 - ae^{-j\omega_{co}T_s}\right) \qquad (4.42)$$

$$K = \left|C_{notch}\left(e^{-j\omega_{co}T_s}\right) G_p\left(e^{-j\omega_{co}T_s}\right) \left(1 - e^{-jd\omega_{co}T_s} Q\left(e^{-j\omega_{co}T_s}\right)\right)\right|^{-1} \qquad (4.43)$$

K_l can be solved using Eq. 4.33.

The purpose of this analysis is to convert the parameter optimization set from K_l, a and τ to f_{co}, a and τ, for the same advantages in the physical intuitions and results presentations.

Optimization Procedures

Assuming a fixed notch filter $C_{notch}\left(z^{-1}\right)$ is used, the PES TMR performance optimization for the PID controller involves the following procedures:

1. Construct the discrete-time domain servo system plant model, as described in Chap. 2;

2. Form the weighting sequences using the DFT magnitude of various TMR sources, as described in Section 4.4.2;

3. Select an initial crossover frequency f_{co} for evaluation;

4. Select an initial a for evaluation. a determines the shape of the controller and stability margins. The initial choice of a should be the most conservative in keeping the stability margins, therefore it can be chosen so that the PD controller $\left(1 - az^{-1}\right)$ have the maximum phase. Based on Eqs. 4.22 and 4.28, chose $a = \cos\left(\frac{2\pi f_{co}}{F_s}\right)$, where F_s is the sampling frequency. Given K_i and f_{co}, K_l can be uniquely determined using the methods described before. Therefore the controller $C_{PID}\left(z^{-1}\right) = K_i\left(1 - az^{-1}\right)$ is determined;

5. Construct the frequency samples $S\left(k\right)$, $T\left(k\right)$, and $D\left(k\right)$ from the servo sensitivity function, complementary sensitivity function, and the disturbance transfer function,

respectively;

6. Solve for the cost index in Eq. 4.14; the result is the computed PES variance obtained from the frequency-domain;

7. Vary a and K_i, and repeat Step 5 and 6. Use available numerical optimization tools, such as the Optimization Toolbox in MATLAB, to obtain a local minimum of the cost index J. Because the weighting sequences are obtained from the processed experimental data, it is not guaranteed that the cost function is convex $w.r.t.$ the parameter set a, f_{co} and K_i; the local minimum of the cost function is not necessary its global minimum. Special attention should be paid to the physical meanings of the results. During the optimization, the required stability margins have to be met. If the gain margin is less than $5\,dB$ or the phase margin is less than $30°$, the optimization loop $(5 \rightarrow 6 \rightarrow 7 \rightarrow 5...)$ is broken and the Step 8 is executed;

8. Go to Step 3 with different open-loop crossover frequency f_{co}. Parameter a and K_i for PES TMR performance optimization will be selected for the current f_{co} through Steps 4, 5, 6, and 7.

The same procedure is used for the DOB+PD controller, except that in all the steps, the time constant τ of the Q filter is used instead of the integral gain K_i.

Optimization Results and Discussion

Figure 4.19 illustrates the optimization results for the DOB based servo with fixed $\tau = 0.001$. The height of the surface is the PES 3σ value in micro inch. The x and y axis are a and f_{co}, respectively. It can bee seen that the trend of the decreasing PES 3σ with
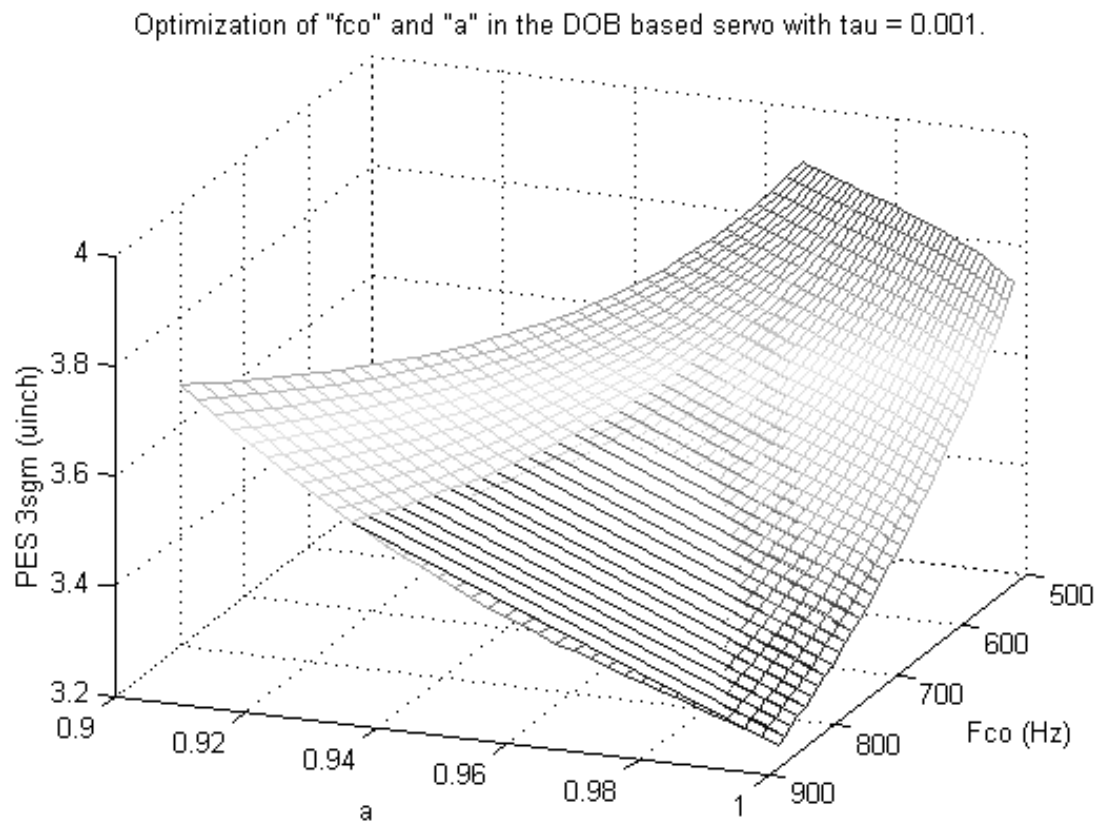
Figure 4.19: Optimizing DOB based servo with $\tau = 0.001$.
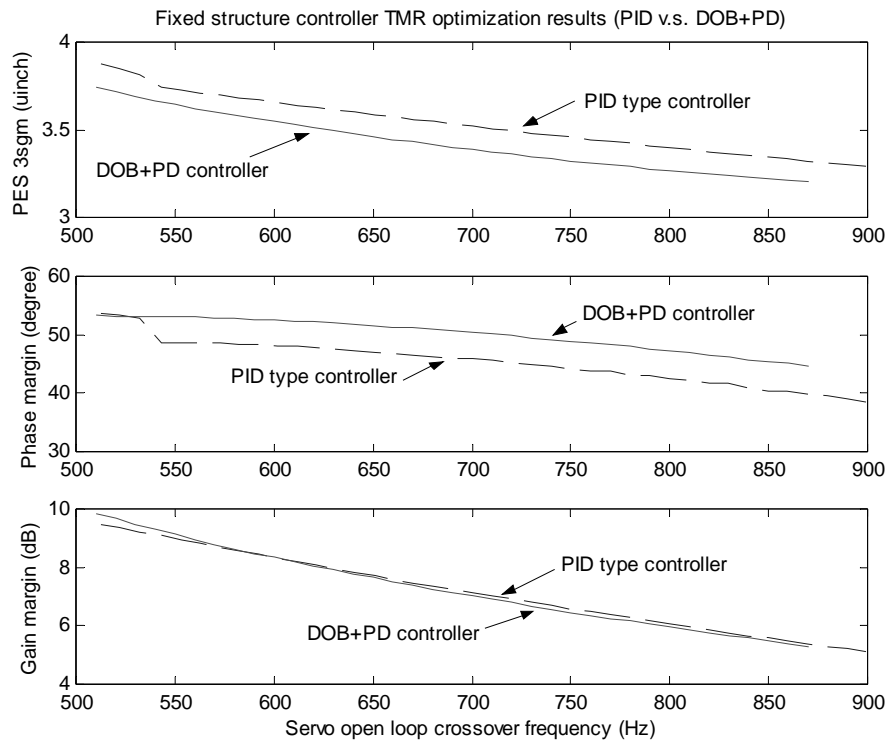
Figure 4.20: Comparison between DOB controller and the PID controller.

the increase of the open-loop crossover f_{co} and a. The stability margins are satisfied for all points on the surface, but are not illustrated in the figure. For each f_{co}, there is at least one point having the smallest PES 3σ value. These points for all f_{co} are shown in the first plot in Fig. 4.20, together with their associated stability margins.

The optimization results of the PID servo are also shown in Fig. 4.20. The best achievable PES 3σ, and the associated phase and gain margins at different open-loop crossover frequencies f_{co} are compared with the DOB based servo. It can be seen from the figure that the stability margins decrease with increase of f_{co}. It is easy to see the trade-off between the stability margins and the best achievable TMR performance for a

fixed-structure controller. At each f_{co}, the 2FOF controller with DOB achieved better PES variance and better stability margins than the PID controller.
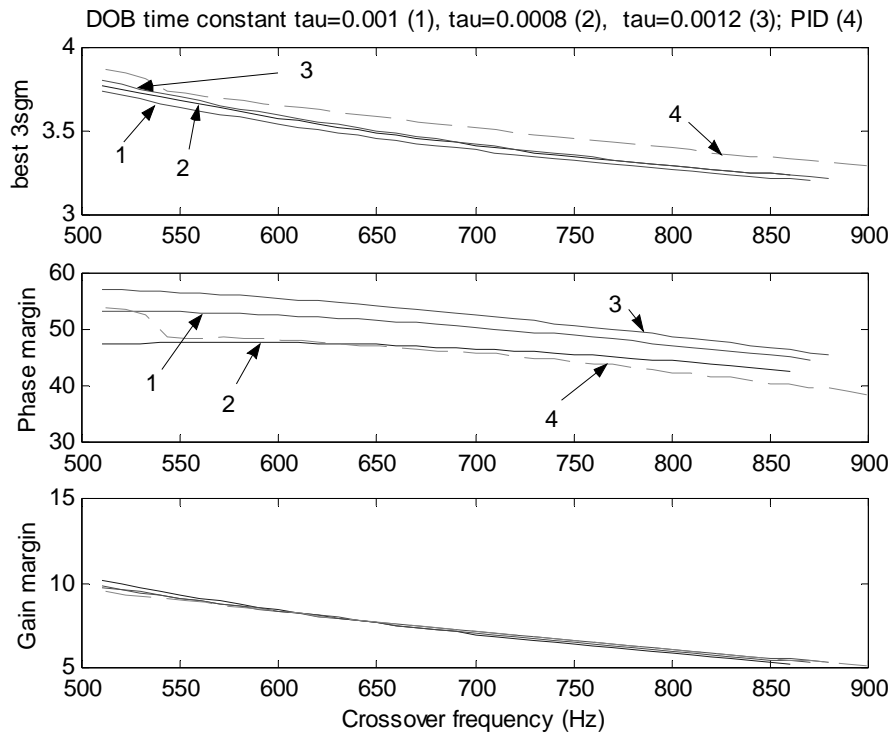
Figure 4.21: Effects of different DOB time constant τ on the optimization results. Curve 1: $\tau = 0.001$; Curve 2: $\tau = 0.0008$; Curve 3: $\tau = 0.0012$; Curve 4: the optimized PID type controller

The effects of the DOB time constant τ on the optimization results are shown in Fig. 4.21. The optimized DOB+PD servo with $\tau = 0.001$ (shown as Curve 1) achieves better TMR performance than that with $\tau = 0.0008$ (Curve 2) or $\tau = 0.0012$ (Curve 3). The servo with $\tau = 0.001$ also have a better phase margin that with $\tau = 0.0008$. The gain margins are similar.

Figure 4.22 shows the relationship between the weighting components in the cost function (Eq. 4.14) and the open-loop crossover frequency f_{co}. Curve m, d, sn denote the
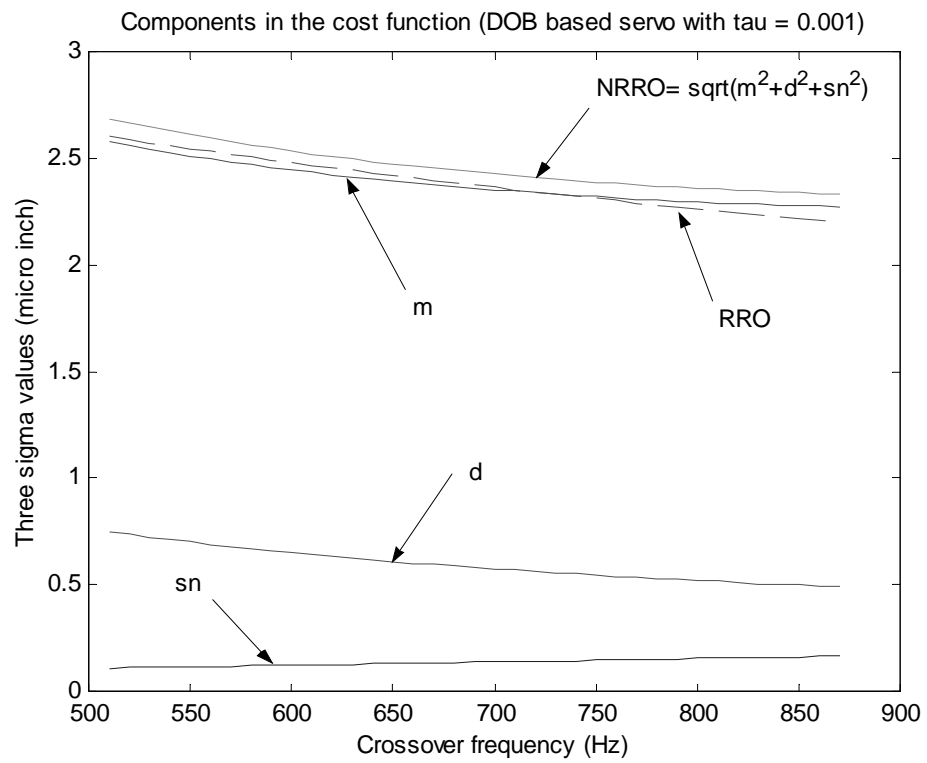
Figure 4.22: Components in the weighting function v.s. the crossover frequency f_{co}

three sigma plots of PES caused by the disk modes, torque disturbances, and the sensor noise, respectively. The effects of the sensors noise on PES increases with the crossover frequency, while those of the other two components decrease with it.

4.5   Summary

This chapter was devoted to presenting and validating various new approaches to improve the servo systems used in the single stage actuator based disk drive. Those new approaches were based on the knowledge of the servo system and TMR modeling in Chap. 2, and benefited from the two degree of freedom structure servo described in Chap. 3.

The experimental results of the 2DOF control structure for the HDD servo systems are presented. The experiments on a Fujitsu M2954 SCSI drive setup verified the effectiveness of the new reference generation method, as well as the disturbance observer structure used in the 2DOF control. The new reference profiles were designed in two stages: off-line simulations and on-line reference generation with adjustments using the SMART (Structural vibration Minimized AcceleRation Trajectory) technique. This systematic profile design method achieved a higher seeking performance than the conventional proximate time optimal servo (PTOS) approach. The disturbance observer structure was implemented in the track seeking servo to achieve smaller tracking errors than the conventional PID controller, and shorter seeking time.

Repetitive control for RPES compensation and its constraints on HDD applications were discussed. A new position feedforward control method using the servo sector RRO fields was proposed. It first identifies the RRO TMR source patterns along each track from

raw PES, then save the information to the RRO fields within the associated servo sectors. The analysis and the procedures to obtain the RRO TMR source patterns are presented. The saved information within each servo sector was used to correct the PES reading from the bursts of the sector. The simulation results have shown that this position feedforward method achieved 30% improvement of the track density.

TMR performance optimization of the fixed-structure controllers were stressed in this Chapter. Without the optimizations of the servo controllers for a specific mechanical platform and noise environment, their comparisons based on PES TMR performance are not fair and groundless. The optimization problem was first formulated using the PES variance obtained from the DFT domain as the cost function. The TMR source DFT were used as weighting sequences associated with servo system transfer functions. For a fixed-structure controller, its parameters are the tuning factors. When used for the PID controller and the DOB based 2DOF controller, the parameter sets for optimization were converted to have more intuitive physical meanings. Servo open-loop crossover frequency (so called servo bandwidth in the HDD industry) was used as one of the parameters for TMR optimization. As seen from the optimization process, the bandwidth itself is only one of a few parameters to determine the PES TMR performance. The shape of the controller, and the stability margins are equally important as the servo bandwidth to the TMR performance.

The optimization procedures and results were presented in detail. A fully optimized 2DOF controller with DOB demonstrated a superior TMR performance than that of the conventional PID controller. This result further validated the advantage of the 2DOF control for HDD servo systems.

Chapter 5

Conclusions and Suggestions on the Future Research

5.1 Conclusions

This dissertation investigated a two degree of freedom (2DOF) controller for HDD servo systems. The unified 2DOF controller operates for both track seeking and following, therefore making the mode changes in MSC unnecessary. The abrupt control input changes associated with the mode changes sometimes make the settling of the R/W head difficult. Another major benefit of 2DOF control is that sophisticated feedforward control algorithms can be used together with the robust inner loop feedback controller.

Servo design criteria were first defined before the hard disk drive servo plant modeling was introduced in Chap. 2. Certain stability margins and TMR performance, the asymptotic tracking ability, and the quick and quiet track seeking are desired for the overall

servo systems.

The noise environment in the hard disk drive application was addressed in the dissertation. The noise is made by various TMR sources, which were categorized into four major components: RRO servo written-in errors, sensor noise, torque disturbances, and disk modes and other unaccounted-for TMR sources. Each of the components was individually analyzed. Based on their key characteristics in the frequency-domain, simple procedures to identify them from raw PES were proposed and used. To re-construct the TMR sources modeling, both time-domain and frequency-domain techniques to process PES were used. In the frequency-domain, normalized discrete-time Fourier transform (DFT) was used instead of the power spectrum. The time-domain TMR source sequences can be represented by the superposition of complex sinusoids described by the sample values of their DFT sequences. Variance and standard deviations of the time-domain sequence were shown to be easily obtained from their DFT magnitude.

In Chap. 3, the 2DOF controller and its three major components are described in detail. DOB and ARC are used as the inner loop controllers, and are compared by simulations. The feedforward control algorithms, including the zero phase error tracking (ZPET) control and the model following control, are also described in Chap. 3. A new reference generation method is proposed. The new reference profiles were designed in two stages: off-line simulations and on-line reference generation with adjustments using the SMART (Structural vibration Minimized AcceleRation Trajectory) technique. Simulations demonstrated that the 2DOF control structure with the new reference generation method performs better than MSC with PTOS. The improvement was mostly achieved in the deceleration

period due to the use of back $e.m.f.$ effects.

Chap. 4 is devoted to presenting and validating various new approaches to improving the servo systems used in the single-stage actuator based disk drive. Those new approaches all benefited from the 2DOF structure.

The experimental results of 2DOF control on a Fujitsu M2954 SCSI drive setup verified the effectiveness of the new reference generation method, as well as of the disturbance observer structure. The new systematic profile generation method achieved a higher seeking performance than the conventional proximate time optimal servo (PTOS) approach. The disturbance observer structure was implemented in the track seeking servo and achieved smaller tracking errors than the conventional PID controller, and a shorter seeking time.

Repetitive control for RPES compensation and its constraints on HDD applications were discussed in Chap. 4. A new position feedforward control method using the servo sector RRO fields was proposed. The simulation results showed that this position feedforward method achieved 30% improvement of the track density.

TMR performance optimization of fixed-structure controllers was emphasized. The optimization problem was formulated to minimize the PES variance. The TMR source models were used as weighting sequences in the cost function. Both a 2DOF controller with DOB and a conventional PID controller are optimized for the TMR performance. The former achieved better PES variance and stability margins. This further validated the proposed 2DOF controller.

5.2   Suggestions on Future Research

To improve the hard disk drive servo systems, it is crucial to characterize the noise environment in which they operate. In a disk drive company, this could be achieved by a close working relationship between the servo team and the mechanical team. In an academic setting, research on servo techniques may also need to be tied to that on the mechanical aspects of hard disk drives, such as disk platter vibrations, media noise, etc.

More accurate TMR sources models are required for better servo system designs and optimizations. For example, in Chap. 2, the torque disturbance model was approximated using simple white noises. Although this greatly simplified the servo design and optimization procedures, it may not accurately reflect the true torque disturbances. The identification of their frequency contents may be best achieved with a theoretical analysis of the windage effects on the HSA together with sophisticated experiments, such as using an LDV to measure the position of a floating arm.

TMR sources identification is even more important for the dual stage servo systems. In general, the position of their first stage actuator is not directly available, and there are more noise injection points in the system. It is more difficult to de-couple the effects of various TMR sources on the PES due to the added complexity of the dual stage servo systems, and therefore it is more difficult to reconstruct the TMR source models from the raw PES readings.

There are several tasks that remain unfinished in this dissertation due to the constraints imposed by the experimental setups. For the 2DOF controller, a complete experiment implementing both the new reference generation method and the disturbance

observer structure simultaneously needs to be performed on a hard disk drive with a faster DSP than that of the Fujitsu M2954 drive. It is also desirable to have experimental results validating the proposed TMR optimization method for fixed-structure servos, and validating the proposed position feedforward control using servo sector RRO fields. All the experiments require access to the DSP firmware and the ability to successfully modify it.

The TMR optimization for a fixed-structure controller for a dual stage servo needs to be modified. The cost function may also be the PES variance, which has more weighting terms due to the added complexity of the servo structure and TMR sources, such as the windage and control input noise affecting the position of the second actuator. The system transfer functions are more complicated, and the TMR sources are more difficult to characterize. These TMR related issues need to be investigated in the future.

Current research on dual stage servo systems also includes the design of effective track seeking control algorithms. For long stroke seeks, the difference between the single stage and the dual stage tracking controllers is small. However, the latter has the potential to achieve much better performance for the short seeks and smoother head settling at the end of a seek, due to its increased servo bandwidth. These track seeking performance related issues should be addressed for dual stage servo systems.

Bibliography

[1] Daniel Abramovitch, Terril Hurst, and Dick Henze. Decomposition of baseline noise sources in hard disk position error signals using the pes pareto method. In *Proceedings of the American Control Conference*, pages 2901–2905, Albuquerque, USA, 1997.

[2] Daniel Abramovitch, Terril Hurst, and Dick Henze. Measurement for the pes pareto method of identifying contributors to disk drive servo systems errors. In *Proceedings of the American Control Conference*, pages 2896–2900, Albuquerque, USA, 1997.

[3] Daniel Abramovitch, Terril Hurst, and Dick Henze. The pes pareto method: uncovering the strata of position error signals in disk drives. In *Proceedings of the American Control Conference*, pages 2888–2895, Albuquerque, USA, 1997.

[4] Daniel Abramovitch, Terril Hurst, and Dick Henze. An overview of the pes pareto method for decomposing baseline noise sources in hard disk position error signals. *IEEE Transactions on Magnetics*, 34:17–23, 1998.

[5] B. Amstrong-Helouvry, P. Dupont, and C. C. De Wit. A survey of models, analysis tools and compensation methods for the control of machines with friction. *Automatica*, 30:1083–1138, 1994.

[6] K. J. Astrom, P. Hagander, and J. Sternby. Zeros of sampled systems. *Automatica*, 20:31–38, 1984.

[7] K. J. Astrom and B. Wittenmark. A survey of adaptive control application. In *Proceedings of the 34th Conference on Decision and Control*, pages 649–654, New Orleans, 1995.

[8] H. S. Chang, S. E. Baek, J. H. Park, and Y. K. Byun. Modeling of pivot friction using relay function and estimation of its frictional parameters. In *Proceedings of the American Control Conference*, pages 3784–3789, San Diego, USA, 1999.

[9] Kok-Kia Chew. Control system challenges to high track density magnetic disk storage. *IEEE Transactions on Magnetics*, 32, 1996.

[10] Kok-Kia Chew. Constrained linearization of embedded position error signals (pes). In *Proceedings of the 24th Annual Conference of the IEEE Industrial Electronics Society*, pages 1477–80, Aachen, Germany, 1998.

[11] Kok Kia Chew and Masayoshi Tomizuka. Digital control of repetitive errors in disk drive systems. *IEEE Control Systems*, pages 16–20, 1990.

[12] Evert S. Cooper. Minimizing power dissipation in a disk file actuator. *IEEE Transactions on Magnetics*, 24(3):2081–2091, 1988.

[13] C. Canudas de Wit and P. Lischinsky. Adaptive friction compensation with dynamic friction model. In *IFAC*, pages 197–202, San Francisco, 1996.

[14] C. Mohtadi MA DPhil. Bode's integral theorem for discrete-time systems. *IEE Proceedings*, 137(2):57–66, 1990.

[15] Rick Ehrich. Tpi growth is key to delaying superparamagnetism's arrival. *Data Storage*, 6(10), 1999.

[16] Rick Ehrich and Dick Curran. Major hdd tmr sources and projected scaling with tpi. *IEEE Transactions on Magnetics*, 32(3):1799–1804, 1996.

[17] H.T. Goh et al. Modeling and compensation of pivot friction in a disk drive actuator. In *ACC*, pages 4141–4145, Seattle, 1995.

[18] Jun Ishikawa et al. Head positioning control for low sampling rate systems based on two degree-of-freedom control. *IEEE Transactions on Magnetics*, 32(3):Reprint, 1996.

[19] Masayoshi Tomizuka et al. Disturbance rejection through an external model. *Journal of Dynamics, Measurement, and Control*, 112(6):559–564, 1990.

[20] S. Weerasooriya et al. Design of a time optimal variable structure controller for a disk drive actuator. *IEEE Transactions on Magnetics*, ?(?):?, 199?

[21] T. H. Lee et al. Dsp-based seek controller for disk drive servomechanism. *IEEE Transactions on Magnetics*, 29(6):4071–4073, 1993.

[22] T. Yamaguchi et al. Mode switching control design with initial value compensation and its application to head positioning control on magnetic disk drives. *IEEE Transactions on Industrial Electronics*, 43(1):65–73, 1996.

[23] W. N. Patten et al. A minimum time seek controller for a disk drive. *IEEE Transactions on Magnetics*, 31(3):2380–2387, 1995.

[24] G. F. Franklin, J. D. Powell, and M. L. Workman. *Digital Control of Dynamic Systems (2nd Ed.)*. Anderson Wesley, 1990.

[25] Susumu Hara, Takeyori Hara, Li Yi, and Masayoshi Tomizuka. Novel reference generation for two-degree-of-freedom controller for hard disk drives. *IEEE/ASME Transactions on Mechatronics*, 5(1):73–78, March 2000.

[26] Takeyori Hara and Masayoshi Tomizuka. Multi-rate controller for hard disk drive with redesign of state estimator. In *Proceedings of American Control Conference*, pages 3033–3037, Philadelphia, 1998.

[27] M. Hirata, K. Z. Liu, T. Mita, and T. Yamaguchi. Head positioning control of a hard disk drive using h_∞ theory. In *Proc. of the 31st IEEE Conference of Decision and Control*, pages 2460–2461, Tucson, AZ, 1992.

[28] Hai T. Ho. Noise impact on servo tmr. In *Proceedings of the American Control Conference*, pages 2906–2909, Albuquerque, USA, 1997.

[29] Y. Hori. Robust motion control based on a two-degree-of-freedom servo system. *Advanced Robotics*, 7(6):525–546, 1993.

[30] Roberto Horowitz and Bo Li. Adaptive control for disk file actuators. In *Proceedings of the 34th Conference on Decision and Control*, pages 655–660, 1995.

[31] Roberto Horowitz and Bo Li. Design and implementation of adaptive non-repetitive

track-following disk file servos. In *Proceedings of the 1995 American Control Conference*, pages 4161–4166, 1995.

[32] Roberto Horowitz and Bo Li. Adaptive track-following servos for disk file actuators. *IEEE Transactions on Magnetics*, 7(6):525–546, 1996.

[33] Roberto Horowitz, S. Pannu, and Bo Li. Adaptive track following servos for disk files. In *Proceedings of the 13th World Congress, International Federation of Automatic Control*, pages 495–500, San Francisco, CA, 1996.

[34] Bill Hurst. Keeping track: how to test a 20 gb/sqin drive. *Data Storage*, 6(10), 1999.

[35] C. D'Angelo III and C. D. Mote Jr. Natural frequencies of a thin disk, clamped by thick collars with friction at the contacting surfaces, spinning at high rotation speed. *Journal of Sound and Vibration*, 168(1):1–14, 1993.

[36] Jun Ishikawa and Masayoshi Tomizuka. Pivot friction comepnsation using an accelerometer and a disturbance observer for hard diak drives. In *ASME International Mechanical Engineerng Congreess and Exposition*, 1997.

[37] C. Kempf and S. Kobayashi. Discrete-time disturbance observer design for systems with time delay. In *IEEE 4th Advanced Motion Control*, pages 332–337, Mie, Japan, 1996.

[38] C. Kempf, W.C. Messner, M. Tomizuka, and R. Horowitz. Comparison of four discrete-time repetitive control algorithms. *IEEE Control Systems Magazine*, 13(6):48–54, 1993.

[39] Carl J. Kempf and Seiichi Kobayashi. Design of a discrete time tracking controller for

a high speed, high accuracy positioning system. In *3rd International Conference on Motion and Vibration Control (MOVIC)*.

[40] H. Lee and Masayoshi Tomizuka. Design of friction-compensated and robust digital tracking controllers for high-accuracy positioning systems. In *Japan-USA Symposium on Flexible Automation*, pages 155–162, Kobe, 1994.

[41] Ho Seong Lee and Lin Guo and. Servo performance prediction for high capacity disk drives. In *Proceedings of the American Control Conference*, pages ??–??, ??, USA, 1998.

[42] Ho Seong Lee and Masayoshi Tomizuka. Robust motion controller design for high-accuracy positioning systems. *IEEE Transactions on Industrial Electronics*, 43(1):48–55, 1996.

[43] Jianwu Li and Tsu-Chin Tsao. Rejection of repeatable and non-repeatable disturbances for disk drive actuators. In *Proceedings of the American Control Conference*, pages 3615–3619, San Diego, USA, 1999.

[44] Jeffrey S. McAllister. The effect of disk patter resonances on track misregistration in 3.5 inch disk drives. *IEEE Transactions on Magnetics*, 32, 1996.

[45] C. Denis Mee and Eric D. Daniel. *Magnetic Recording Volume I: Technology*. McGraw-Hill, 1987.

[46] C. Denis Mee and Eric D. Daniel. *Magnetic Recording Volume II: Computer Data Storage*. McGraw-Hill, 1987.

[47] Y. Mizoshita, S. Hasegawa, and K. Takaishi. Vibration minimized access control for hard disk drives. *IEEE Transactions on Magnetics*, 32:1793–1798, 1996.

[48] Lucy Y. Pao and G. F. Franklin. Time optimal control of flexible structures. In *Proc. of the 29th IEEE Conference of Decision and Control*, pages 2580–2581, Honolulu, Hawaii, 1990.

[49] Lucy Y. Pao and G. F. Franklin. Robustness studies of a time optimal controller. In *Proc. of the 31st IEEE Conference of Decision and Control*, pages 3559–3564, Tucson, Arizona, 1992.

[50] Lucy Y. Pao and G. F. Franklin. Proximate time-optimal control of third-order servomechanisms. *IEEE Transactions on Automatic Control*, 38(4):560–580, 1993.

[51] Lucy Y. Pao and Gene F. Franklin. The robustness of a proximate time-optimal controller. *IEEE Transactions on Automatic Control*, 39(9):1963–1966, 1994.

[52] M. D. Sidman. Time optimal voltage-constrained deceleration velocity profile design for disk drive. In *ACC*, pages 4146–4151, Seattle, 1995.

[53] Craig Smith and Masayoshi Tomizuka. Shock rejection for repetitive control using a disturbance observer. In *Proceedings of the 35th IEEE Conference on Decision and Control*, pages 2503–2504, Kobe, Japan, 1996.

[54] Masayoshi Tomizuka. Zero-phase error tracking controller for digital control. *ASME Journal of Dynamics, Measurement and Control*, 109(1):65–68, 1987.

[55] Masayoshi Tomizuka. On the design of digital tracking controllers. *Transactions of ASME, Journal of Dynamic Systems, Measurement, and Control*, 115:412–418, 1993.

[56] Masayoshi Tomizuka. Model based prediction, preview and robust controls in motion control systems. In *IEEE 4th Advanced Motion Control*, pages 197–202, Mie, Japan, 1996.

[57] Jun Ueda, Akihiko Imagi, and Hitoshi Tamayama. Track following control of large capacity flexible disk drive with disturbance observer using two position sensors. In *Proceedings of the 1999 IEEE/ASME International Conference on Advanced Intelligent Mechatronics*, pages 144–149, Atlanta, USA, 1999.

[58] T. Umeno and Y. Hori. Robust speed control of dc servomotors using modern two degrees-of-freedom controller design. *IEEE Transactions on Industry Applications*, 38(5):363–368, 1991.

[59] P.D Welch. The use of fast fourier transform for the estimation of power spectra: a method based on time averaging over short, modified periodograms. *IEEE Transactions on Audio Electroacoust*, AU(15):70–73, 1967.

[60] Mattew T. White and Masayoshi Tomizuka. Increased disturbance rejection in magnetic disk drives by acceleration feedforward control. In *Proceedings of the 13th World Congress, International Federation of Automatic Control*, pages 489–494, San Francisco, CA, 1996.

[61] Mattew T. White and Masayoshi Tomizuka. Increased disturbance rejection in mag-

netic disk drives by acceleration feedforward control and parameter adaptation. *Control Engineering Practice*, 5(6):741–751, 1997.

[62] Mattew T. White, Masayoshi Tomizuka, and Craig Smith. Rejection of disk drive vibration and shock disturbances with a disturbance observer. In *Proceedings of the 1999 American Control Conference*, pages 4127–31, Piscataway, NJ, 1999.

[63] Mattew T. White, Masayoshi Tomizuka, and Craig Smith. Improved track following in magnetic disk drives using a disturbance observer. *IEEE/ASME Transactions on Mechatronics*, 5(1):3–11, 2000.

[64] Matthew White and Wei-Min Lu. Hard disk drive bandwidth limitations due to sampling frequency and computational delay. In *Proceedings of the 1999 IEEE/ASME International Conference on Advanced Intelligent Mechatronics*, pages 120–125, Atlanta, USA, 1999.

[65] T. Yamaguchi, H. Numasato, and H. Hirai. A mode-switching control for motion control and its application to disk drives: design of optimal model-switching condistions. *IEEE/ASME Transactions on Mechatronics*, 3:202–209, 1998.

[66] Bin Yao, M. Al-Majed, and Masayoshi Tomizuka. General high performance adaptive robust control of machine tools. In *Proceedings of Advanced Intelligent Mechatronics*, Tokyo, Japan, 1997.

[67] Bin Yao, M. Al-Majed, and Masayoshi Tomizuka. High-performance robust motion control of machine tools: an adaptive robust control approach and comparative experiments. *IEEE/ASME Transactions on Mechatronics*, 2(2):63–76, 1997.

[68] Bin Yao, M. Al-Majed, and Masayoshi Tomizuka. High performance robust motion control of machine tools: an adaptive robust control approach and comparative experiments. In *Proceedings of ACC*, 1997.

[69] Bin Yao and Masayoshi Tomizuka. Smooth robust adaptive sliding mode control of robot manipulators with guaranteed tranisent performence. In *Proceedings of Advanced Intelligent Mechatronics*, pages 1176–1180, 1994.

[70] Li Yi and Masayoshi Tomizuka. Robust motion control of mechanical systems with compliance. In *Proceedings of the 35th IEEE Conference on Decision and Control*, pages 2462–2467, Kobe, Japan, 1996.

[71] Li Yi and Masayoshi Tomizuka. Regulation of mechanical systems with compliance. In *Proceedings of the second Chinese world congress on intelligent control and intelligent automation*, pages 1571–1576, Xian, China, 1997.

[72] Li Yi and Masayoshi Tomizuka. Two degree-of-freedom control with adaptive robust control for hard disk servo systems. In *Proceedings of the 5th International Workshop on Advanced Motion Control*, pages 604–610, Coimbra, Portugal, 1998.

[73] Li Yi and Masayoshi Tomizuka. Two-degree-of-freedom control with roburst feedback control for hard disk servo systems. *IEEE/ASME Transactions on Mechatronics*, 4:17–24, 1999.